Høgskulen på Vestlandet

Master Thesis

ING5002

Predefinert informasjon

Startdato:	25-05-2019 09:00	**Termin:**	2019 VÅR
Sluttdato:	03-06-2019 14:00	**Vurderingsform:**	Norsk 6-trinns skala (A-F)
Eksamensform:	Masteroppgave		
SIS-kode:	203 ING5002 1 MOPPG 2019 VÅR Haugesund		
Intern sensor:	(Anonymisert)		

Deltaker

Kandidatnr.: 101

Informasjon fra deltaker

Engelsk tittel *: Feasibility study of correlating mass quantity output and fuel parameter input of different simulations using Fire Dynamics Simulator

Egenerklæring *: Ja

Inneholder besvarelsen konfidensiell materiale?: Nei

Jeg bekrefter at jeg har registrert oppgavetittelen på norsk og engelsk i StudentWeb og vet at denne vil stå på vitnemålet mitt *: Ja

Jeg godkjenner avtalen om publisering av masteroppgaven min *

Ja

Er masteroppgaven skrevet som del av et større forskningsprosjekt ved HVL? *

Nei

Er masteroppgaven skrevet ved bedrift/virksomhet i næringsliv eller offentlig sektor? *

Nei

Feasibility study of correlating mass quantity output and fuel parameter input of different simulations using Fire Dynamics Simulator

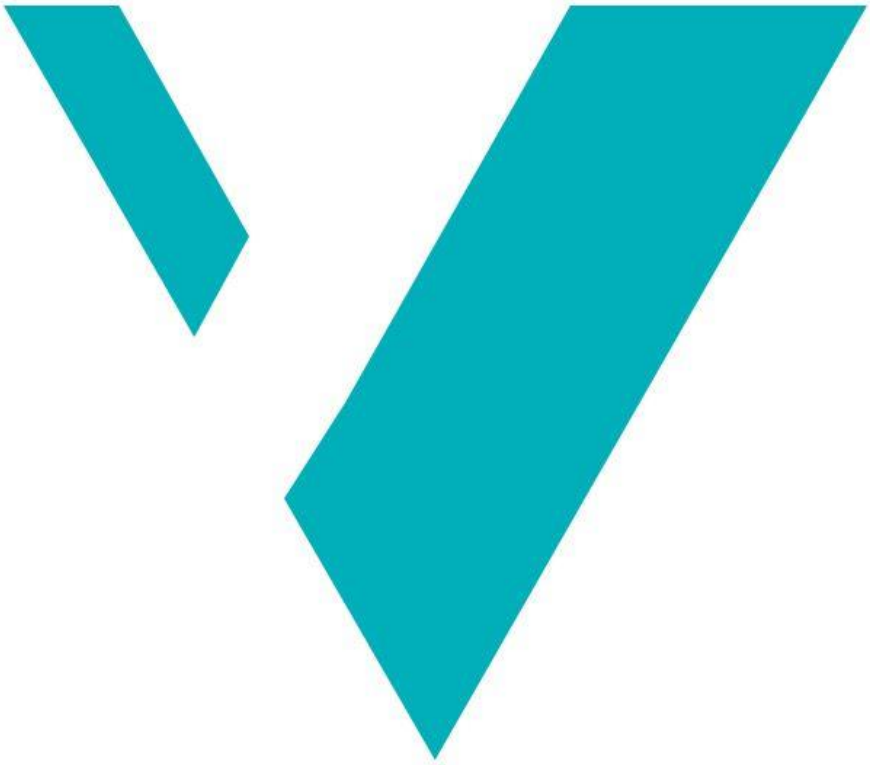

Steffen Oliver Sæle

WESTERN NORWAY UNIVERSITY OF APPLIED SCIENCES

Master Thesis in Fire Safety Engineering

Haugesund
[06.2019]

Western Norway University of Applied Sciences

Feasibility study of correlating mass quantity output and fuel parameter input of different simulations using Fire Dynamics Simulator

Master thesis in Fire Safety Engineering

Author: Steffen Oliver Sæle	Author sign. 
Thesis submitted: Spring 2019	Open thesis
Tutor: Xiaoqin Hu External tutor: Yvonne Bjarkø Skaare at Rambøll Norge AS	
Keywords: correlate input and output, correlation factor, correlate simulations, output estimation, mass quantity estimation, parameter sensitivity, Fire Dynamics Simulator	Number of pages: 76 + Appendix: 41 Haugesund/03.06/2019 Place/Date/Year

This thesis is a part of the master's program in Fire Safety engineering at Western Norway University of Applied Sciences. The author(s) is responsible for the methods used, the results that are presented, the conclusion and the assessments done in the thesis.

Preface

This thesis constitutes the final study required to complete the Fire Safety Engineering, Master of Science, program at the Western Norway University of Applied Sciences in Haugesund. Though the study has been both time consuming and challenging, it certainly has been intriguing. The basic idea of this thesis originated through conversation with fellow students and engineers, discussing issues often encountered while developing performance-based Fire Safety Design. One of these issues were the uncertainties arising when deciding upon the simulation input parameters, likely to strongly affect the results of the simulation and thereby, possibly, Fire Safety Design. I found the subject compelling and chose to study this issue in my master's thesis. Preliminary studies ensued, making inquiries as to relations between several output quantities often evaluated regarding Fire Safety Design, and input parameters likely to affect these. From the preliminary studies, promising patterns of correlation between fuel parameter input and mass quantity output were observed. As such, this path was pursued and eventually led to this thesis.

Acknowledgements

I would like to extend my sincere gratitude to my tutor, Associate Professor Xiaoqin Hu, at the Western University of Applied Sciences, who aided me regarding most aspects of this thesis. Without her input as to the format of the thesis, methodology, and physical interpretation of simulation results, this thesis may have been challenging to read and possibly somewhat meager. Especially considering the complex physics and mathematics encompassed in CFD simulation tools, such an accomplished sparring partner has been of value.

Additionally, thanks to my external tutor and now colleague at Rambøll Norway Ltd, Master of Science grad. Yvonne Bjarkø Skaare, who, in the spring of 2018, presented me with several basic outlines for possible themes for my thesis. These were themes regarding issues often encountered using fire simulation tools in the context of performance-based design. In collaboration, we deemed the most promising, and of importance to the field, the feasibility study of correlating fuel input simulation parameters to mass quantity output, which eventually led to this thesis. Yvonne also provided me with valuable input as to simulation series set-up, relevant for the fire safety engineering community, as well as feedback on the thesis and simulation results.

Finally, thanks to my department at Rambøll, for letting me use the company Pyrosim license and "computer park". As I've conducted several hundred simulations (including preliminary studies), this has been essential to my thesis.

Abstract

Fire accidents often spur massive attention due to the associated potential for enormous consequences for lives and property. To facilitate prevention and mitigation of fire accidents, knowledge as to the dynamics associated with fire development and spread of smoke and hot gases needs to be ascertained. To this end, forensic investigators, engineers and scientists apply software for fire simulation. Such software embodies mathematical models of the intricate physical processes associated with fire. Using such simulations, engineers and others can compute, for instance, the duration of which conditions in an egress route are tenable. Tenable conditions may often be related to concentrations of soot (which obscure visibility) and carbon monoxide (CO, which can be asphyxiating), and can rarely be calculated more precise than by use of simulations.

A drawback of such simulation tools are the computational costs of conducting simulations of a fire scenario. This can be highly time consuming and costly in projects. Additionally, it is often necessary to conduct several simulations, where simulation input is revised between simulations, further increasing time consumption. This is necessary, due to the uncertainty often associated with input parameters applied for the simulation. For instance, there is seldomly pristine knowledge as to what commodities (or fuels) may be involved in a building fire, or what energy levels and species yields combustion may lead to.

The purpose of this study is to investigate the feasibility of correlating simulation fuel *input* data to mass quantity *output* data (such as concentrations of soot and CO). This between two simulations applying different fuel parameter input. As such, the correlations may be used to estimate the mass quantity output of one simulation based on the mass quantity results of a base simulation. Provided reasonable estimations can be produced from this procedure, the computational cost of an analysis involving simulations may be reduced.

The correlations are deduced from functions paramount to the mass transport equations of a much-used simulation software, Fire Dynamics Simulator (FDS). Two functions of correlation, or correlation factors, have been proposed and developed. Correlation factor 1 considers the species mass source term of the FDS mass transport equation. Correlation factor 2 is based on the method FDS applies to collect information as to the species mass fractions of the smoke.

To investigate the feasibility of correlation, 93 simulations have been conducted in 19 series. Each series was comprised of 4-5 simulations. Individual series applied simulations of different fire scenarios. Between every simulation in each series, only fuel input parameters were altered. One of the simulations in each series was used as a base simulation. The mass quantity output of the base simulation was multiplied with the correlation factors, to ascertain estimations of mass quantity results of all other simulations in the series. The estimations were further compared to the actual simulations, to assess the performance of the correlation factors. This, for instance, in relation to potential tendencies for over- and underestimations associated with the characteristics of the fire scenario. The mass quantities considered and estimated were soot densities and mass fractions of CO. These quantities were statistically measured (mean and maximum values) in stationary volumes in different locations within the simulated enclosures.

The findings of this study suggest that reasonable estimations of mass quantity output may be produced by applying the correlation factors and a base simulation. Out a total of 744 mass quantity estimations, 82,2% and 94,8% deviated from the simulated mass quantities within the percentile intervals of $\mp$5% and $\mp$10% respectively. Approximately 0,5% deviated above 20%, with a maximum deviation of approximately 22%.

One of the findings regarding tendencies of over- and underestimations, is that high values of heat release rate (HRR) and/or measurements made in the vicinity of the fire origin, rendered simulation output of different simulations in a series more similar than estimated by the correlation factors. This led to under- and overestimations for low and high values of the correlation factors respectively. Adversely, for low values of HRR and/or for measurements made somewhat far away from the fire origin, low and high values of the correlation factors led to over- and underestimations respectively. Further, it was found that correlation factor 1, which considers the species mass production rates, provided more precise estimations than correlation factor 2, for the conducted simulations. The differences were, however, rather small.

These, and other findings, mainly apply to the simulations conducted in this study. However, it is likely that many of the identified tendencies are applicable to similar scenarios. As this is challenging to precisely determine, the correlation factors should be used cautiously. The most important limitation of the correlation factors has generally been the difference of fuel parameter input between the base simulation and the simulation of which estimations were made. Large differences, indicated by the difference between the value of the correlation factor and unity, generally coincided with increased potential for estimation discrepancies. In this study, many of the correlation factor-values varied between 0,14 and 1,7. Nonetheless, limitations considered, the correlation factors can likely be used to ascertain increased knowledge as to the possible consequences of altering simulation fuel parameter input of a base simulation, and this in a relatively short amount of time.

Samandrag

Brannulukker får ofte stor merksemd grunna deira potensiale for enorme konsekvensar i samband med liv og eigedom. For å leggje til rette for førebygging og konsekvensavgrensing av brann trengs forståing for dynamikken knytt til brannutvikling og spreiing av røyk og varme gassar. For å tileigne seg slik kunnskap, nyttar etterforskarar, ingeniørar og forskarar ulike mjukvarar for simulering av brann. Desse mjukvarene inneheld matematiske tolkingar av dei komplekse fysiske prosessane knytt til brann. Slik kan ingeniørar og andre berekne, til dømes, kor lenge ein rømingsveg kan nyttast i høve brann, før forholda vert kritiske. Kritiske forhold kan ofte knytast opp mot konsentrasjonar av sot (som hindrar sikt) og karbonmonoksid (CO, som kan verke kvelande), og kan sjeldan bereknast meir nøyaktig enn ved hjelp av simuleringar.

Ulempa med slike simuleringsprogram er dei store behova for datakraft som trengs for å gjennomføre berekningar for eit brannscenario. Dette kan være svært tidkrevjande og kostnadsdrivande i prosjekt. Samstundes er det ofte behov for å utføre fleire simuleringar av ulike brannscenario, der ulike parameterar for simuleringsinndata endrast, som igjen aukar naudsynt tidsbruk. Dette må gjerast sidan det ofte er knytt usikkerheiter til parameterar som nyttast for simuleringa. Ein har for eksempel sjeldan god nok kjennskap til kva materiale (eller brensel) som kan inngå i ein bygningsbrann eller kva nivå av energi og gassar som kan bli produsert ved forbrenning.

Føremålet med denne studien er å undersøkje høve for å korrelere simulerings*inndata* for brenselsparameterar til simulerings*utdata* for massekvantitetar (slik som konsentrasjonar av sot og CO). Dette mellom to simuleringar med ulike simuleringsinndata for brenselsparameterar. Slik kan korrelasjonane nyttast til å estimere ei simulering si massekvantitetsutdata basert på massekvantitetsutdata av ei anna simulering. Dersom rimelege estimat kan gjerast gjennom denne prosedyren, kan tidsbruken og kostnadar av simuleringsanalysar bli redusert.

Korrelasjonane er dedusert frå funksjonar som er sentrale for massetransportlikningane nytta i ei mykje brukt simuleringsmjukvare, Fire Dynamics Simulator (FDS). To funksjonar for korrelasjon (eller korrelasjonsfaktorar) er utvikla. Korrelasjonsfaktor 1 tek omsyn til ei kjeldeterm i FDS si massetransportlikning, masseproduksjonsraten. Korrelasjonsfaktor 2 tek utgangspunkt i metoden FDS nyttar for å hente ut informasjon om ulike gassar sine massefraksjonar i røykstraumen.

For å undersøkje korrelasjonsfaktorane har 93 simuleringar blitt gjennomførde i 19 seriar. Kvar serie inneheldt mellom 4 og 5 simuleringar. Individuelle seriar nytta simuleringar av ulike brannscenario. Skilnaden mellom kvar simulering i ei serie, var kunn eigenskapar knytt til brenselet. Vidare blei ei av simuleringane i kvar serie nytta som ei utgangspunktsimulering. Denne simuleringa sine massekvantitetsutdata, multiplisert med korrelasjonsfaktorane, blei nytta til å estimere massekvantitetsutdata til alle andre simuleringar i serien. Ved å samanlikne estimata med faktiske simulerte verdiar, har prestasjonsnivået til korrelasjonsfaktorane blitt vurdert. Dette blant anna i samband med potensielle tendensar for over- og underestimat knytt til karakteristikkar ved dei ulike scenarioa. Dei vurderte og estimerte massekvantitetsutdata var i form av tettleikar av sot og massefraksjonar av CO. Desse har blitt statistisk målt (gjennomsnittlege og maksimale verdiar) i stasjonære volum plassert ulike stader i dei simulerte romma.

Funna i studien indikerer at rimelege estimat av massekvantitetsutdata kan gjerast ved å nytte korrelasjonsfaktorane og ei utgangspunktsimulering. Av totalt 744 estimat av massekvantitetsutdata, avveik 82,2% og 94,8% av desse innafor prosentintervalla på høvesvis $\mp$5% og $\mp$10% frå dei simulerte resultata. Om lag 0,5% av estimata hadde avvik på over 20%, med eit maksimalt avvik på om lag 22%. Av tendensar for over- og underestimat, blei det blant anna funne at høge verdiar av varmegjeving (HRR) og/eller

målingar utførde nære arnestaden gjorde at verdiar av massekvantitetsutdata, for dei ulike simuleringane i serien, låg nærare kvarande enn kva korrelasjonsfaktorane tydde på. Dette leia til under- og overestimat for høvesvis låge og høge verdiar av korrelasjonsfaktorane. Motsett, for låge verdiar av HRR og/eller målingar utførde langt frå arnestaden, leia låge og høge verdiar av korrelasjonsfaktorane til høvesvis over- og underestimat. Vidare blei det funne at korrelasjonsfaktor 1, som tek omsyn til masseproduksjonsraten som følgjer av simuleringsinndata, i gjennomsnitt gav betre estimat enn korrelasjonsfaktor 2, for dei utførde simuleringane. Forskjellane var derimot små.

Desse, og andre funn, gjeld hovudsakleg dei simuleringane som er gjennomførde i denne studien. Samstundes er det truleg at mange av dei identifiserte tendensane for estimatavvikspotensiale også er gjeldande for andre liknande scenario. Dette er derimot utfordrande å fastslå presist, og korrelasjonsfaktorane må difor brukast med omhug. Den viktigaste avgrensinga til korrelasjonsfaktorane, uavhengig av sjølve brannscenarioet, var generelt ulikskapen i brenselsinndata mellom utgangspunktsimuleringa og simuleringa som estimat er utførde for. Store skilnader, som indikerast ved store differansar mellom korrelasjonsfaktorverdien og 1, samsvarte generelt med auke i potensial for estimatavvik. I denne studien varierte dei fleste korrelasjonsfaktorverdiar mellom omtrent 0,14 og 1,7. Samstundes, med avgrensingar teke i omsyn, kan korrelasjonsfaktorane truleg nyttast til å få auka kjennskap til moglege konsekvensar dersom ein endrar brenselseigenskapar av ei simulering, og dette på relativt kort tid.

Table of contents

List of figures

Appendix A:

Appendix B:

List of tables

Appendix:

Nomenclature

A_o	opening area	$[m^2]$
a	number of nitrogen atoms	$[-]$
C	visibility factor	$[-]$
C_v	Deardorff model constant	$[-]$
c_p	specific heat	$[J/gK]$
D	diameter	$[m]$
D	mass diffusivity	$[m^2/s]$
D^*	characteristic flame diameter	$[m]$
E	internal energy	$[J]$
e	mass specific internal energy	$[J/g]$
F	volumetric percentile-distribution	[%]
f	external body forces	$[N]$
$\boldsymbol{f}_b$	drag force vector originating from sub grid-scale particles	$[N]$
g	gravitational acceleration	$[m/s^2]$
H	mass specific stagnation energy (Bernoulli integral)	$[J/g]$
H	enthalpy	$[J]$
ΔH	heat of combustion (enthalpy change)	$[J]$
ΔH_C	heat of combustion per unit mass of fuel consumed	$[J/g]$
$\Delta H_{C,ox}$	heat of combustion per unit mass of oxygen consumed	$[J/g]$
ΔH_f	heat of formation	$[J]$
H_o	opening height	$[m]$
h	mass specific enthalpy	$[J/g]$
h_s	sensible enthalpy	$[J/g]$
K_m	mass extinction coefficient	$[m^2/g]$

k_{sgs}	sub-grid kinetic energy per unit mass	$[J/g]$
k	thermal conductivity coefficient	$[W/mK]$
L_f	flame height	$[m]$
m	mass	$[g]$
$\dot{m}$	mass loss/production rate	$[g/s]$
$\dot{m}_f''$	fuel mass loss flux	$[g/m^2 s]$
$\dot{m}_\alpha'''$	volumetric mass production rate of species α by chemical reactions	$[g/m^3 s]$
$\dot{m}_{b,\alpha}'''$	volumetric mass production rate of species α by evaporation	$[g/m^3 s]$
P	pressure	$[N/m^2]$
Pr_t	turbulent Prandtl number	$[-]$
p	pressure	$[N/m^2]$
$\bar{p}$	background pressure	$[N/m^2]$
$\dot{Q}$	heat release rate	$[W]$
$\dot{Q}^*$	fire Froude number	$[-]$
q_p	enthalpy change at constant pressure	$[J/g]$
$\dot{\boldsymbol{q}}''$	heat flux vector	$[W/m^2]$
$\dot{\boldsymbol{q}}_{\boldsymbol{r}}''$	thermal radiative heat flux vector	$[W/m^2]$
$\dot{q}'''$	volumetric heat release rate by combustion	$[W/m^3]$
$\dot{q}_b'''$	volumetric heat transfer rate to droplets and particles	$[W/m^3]$
$\Re$	universal gas constant	$[J/Kmol]$
r	radius	$[m]$
S	visibility distance	$[m]$
Sc_t	turbulent Schmidt number	$[-]$
T	temperature	$[K]$
t	time	$[s]$

$\boldsymbol{u}$	velocity vector	$[m/s]$
V	volume	$[m^3]$
v_f	radial fire spread velocity	$[m/s]$
W	molecular weight	$[g/mol]$
x	direction x	$[-]$
Y_α	mass fraction of species α	$[g/g]$
y	direction y	$[-]$
Z	mixture fraction	$[g/g]$
z	direction z	$[-]$

Greek symbols

α	thermal diffusivity	$[m^2/s]$
α	time evolving heat release rate	$[W/s^2]$
$\beta_{i,\theta}$	correlation factor i for quantity θ	$[-]$
γ_α	yield of species α by chemical reaction	$[g/g]$
Δ	LES filter width	$[-]$
ε	dissipation rate of turbulent kinetic energy	$[W/g]$
λ	mean free path of gas molecules	$[m]$
μ	dynamic molecular viscosity	$[g/ms]$
μ_t	turbulent viscosity	$[g/ms]$
ν_α	stoichiometric coefficient of species α	$[-]$
ρ	density	$[g/m^3]$
τ	viscous stress tensor	$[N/m^2]$
ψ_O	stoichiometric oxygen to fuel mass ratio	$[g/g]$
ω	vorticity	$[1/s]$

Subscripts

0	initial
∞	ambient
a	air
a	simulation
b	simulation
b	evaporation
C	per unit mass of fuel
C, ox	per unit mass of oxygen
dep	deposition
dt	diffusive-turbulent
f	flame
f	fuel
g	gas
g	gravitational
H	hydrogen
i	component in x-direction
i	species
i	number
j	component in y-direction
k	component in z-direction
m	mass
o	opening
p	constant pressure state
p	products

r	radiative
s	sensible
sgs	sub-grid scale
t	turbulent
th	thermophoretic
v	number of nitrogen atoms
x	number of carbon atoms
y	number of hydrogen atoms
z	number of oxygen atoms
α	species
β	species
θ	mass output quantity

1. Introduction

Fire safety attracts enormous attention due to the tragedies often associated with fire accidents. Recently, incidents such as the Grenfell Tower fire (June, 2017) in London and the Notre-Dame fire (April, 2019) in Paris have spurred massive media attention. In the former incident, 72 people tragically passed [1]. While no lives were lost in the Notre-Dame fire, the building sustained enormous damage, which was a UNESCO World heritage site, built in the 12th and 13th century [2]. The cost of restoring the building to near original state is estimated to lie between 1,13 and 2,3 billion USD (Stephane Bern, head of heritage renovation programs in France). However, these figures are highly uncertain [3].

To aid in preventing such catastrophes, knowledge as to the dynamics of a fire, herein fire development and transport of hot gases, needs to be facilitated. For this purpose, simulation tools have been developed in the last four decades. Such being Computational Fluid Dynamics (CFD) simulation software, developed particularly for investigating fire related problems, for instance, Fire Dynamics Simulator (FDS) [4]. These CFD techniques encompass the mathematical interpretations of the complex physics involved in a fire. Compared to conducting experiments to investigate the potential consequences of a fire, such simulation tools are often advantageous. Many different scenarios can be investigated, providing a high level of detail of the fire, and at lower costs. As such, fire simulation tools have a large user group, consisting of engineers, forensic investigators and scientists.

An issue often encountered, however, is the computational cost required to conduct fire simulations. Even for computers encompassing cutting-edge technology, merely one simulation of a building fire scenario may require weeks or even months to compute, depending on the spatial and temporal fidelity required for the scenario. For instance, the most computationally expensive simulation in this study (described in section 3.3.2) required almost three weeks of computational time, even when dividing the workload over several processors. The simulation time was 600 s and the computational domain was approximately 570 m^3, divided over almost 4 million grid cells (see 2.4.1). The computer used the processor Intel® Xenon® CPU E5-2630 @2,30GHz (2 processors) with 64 GB memory. Additionally, it is often necessary to conduct not just one, but several simulations in an analysis, where alterations are made to simulation input parameters likely to affect the simulation results. Among many others, such parameters may be the chemical composition of the combustible materials and yields of soot and carbon monoxide (CO) from the reaction. In terms of egress, these parameters may determine whether conditions in an egress route are tenable for humans. For instance, increasing yields of soot and CO may reduce visibility distance and increase risk of asphyxiation [5]. Naturally, a simulation series of several fire scenarios with revised input parameters, requires increased computational costs compared to merely a single simulation. However, provided only minor alterations in input parameters are made among individual simulations of a simulation series, it might be feasible to predict the results of one simulation based on the results of a similar simulation. If reasonable estimations of simulation output may be made based on only one simulation, the consequences of alterations in simulation parameters may be revealed, using far less recourses.

The objective of this thesis is to investigate the feasibility of applying the results of one FDS simulation to encompass estimations of other simulations species mass quantity-results (i.e. densities and mass fractions of soot, CO, etc.) if fuel simulation input parameters are revised. In this context, fuel parameters refer to chemical composition of the fuel, product species yields (such as CO and soot) and heat of combustion. In this study, several *base* simulations are conducted, by which estimations of *subsequent* simulation results are made. To attain such estimations, correlation factors are applied. These are functions correlating the solutions to the FDS mass transport equations of the base- and the estimated simulation. Two correlation

factors are developed in this study. One considering source terms to the FDS mass transport equation, and one deduced from the method of which FDS retrieves information about the mass quantities.

The remainder of this thesis begins with the theoretical basics for deducing and evaluating the correlation factors, provided in chapter 2. The deduction of the correlation factors, and description of the simulations conducted to evaluate their performance, are elaborated in chapter 3 (Methods). Estimations are made for several series of simulations, applying different building geometries, heat release rates (HRR), method of species treatment (enabling and disabling soot deposition) and miscellaneous fuel-type variations. In chapter 4 (Results), estimated mass quantities are compared to simulated quantities, for the different simulations conducted. This to investigate the performances of the two correlation factors. Tendencies of estimation discrepancies due to characteristics of fire scenarios and form of mass quantity output are discussed in chapter 5 (Discussion). The discussion chapter also makes inquiries as to which correlation factor may yield the most precise estimations, and under what circumstances, as well as general applicability of the correlation factors. Finally, chapter 6 (Conclusion) elaborate on whether reasonable estimations may be made by use of the correlation factors and summarizes findings as to potential limitations of their use and estimation discrepancies.

2. Theory basics

The theoretical framework needed to construct and evaluate correlations of different simulations, is presented in this chapter. The first two sections include basic fire dynamics, herein associating materials (or fuels) undergoing combustion with generation of heat, and further, how generation of heat may be approached in terms of fire safety engineering. Section 2.3 describe what may be considered the most paramount aspects of CFD in relation to simulating the flow of mass, energy and momentum due to fire. Finally, section 2.4 elaborate on the general approach FDS applies to evolve the solution to the transport equations for mass and constituent variables in time.

2.1. Thermochemistry

Thermochemistry is a discipline concerning the release of energy by chemical reaction. It is derived from the first law of thermodynamics which is a version of the energy conservation law. In the context of fire, it supplies knowledge of topics such as heat of combustion, heat of formation, and methods as to deriving such quantities [6].

Heat of combustion can be described as the heat released when a quantity of substance is oxidized completely to produce stable end products [6]:

$$Fuel + Oxidizer \rightarrow Products + Heat \tag{2.1}$$

This heat generation is associated with the change in enthalpy of the system, in which combustion is taking place. The enthalpy is defined as [6]:

$$H \equiv E + PV \tag{2.2}$$

where E is the internal energy of the system, P and V is the pressure and volume respectively. The heat of combustion, ΔH, is generally associated with the enthalpy change, q_p, due to changes in internal energy and expansion of the fire gases, at constant pressure [6]:

$$Heat = q_p = (E_2 + PV_2) - (E_1 + PV_1) = H_2 - H_1 = \Delta H \tag{2.3}$$

Heat of combustion is further dependent on the reaction of which combustion takes place. It may therefore be convenient to describe heat of combustion in terms of heat of formation, ΔH_f. This is the enthalpy change of the system as one mole of a substance is formed from its constituent elements in a reference state (usually one atm. pressure and 298 K). The relationship between the heat of combustion and the heat of formation can be described via Hess's law [6]:

$$\Delta H = \Delta H_{f,products} - \Delta H_{f,reactants} \tag{2.4}$$

Additionally, heat of combustion is often described relative to consumed constituents, such as unit mass of fuel, ΔH_C, or unit mass of oxygen, $\Delta H_{C,ox}$ [7]. The relation between the two can be expressed [8]:

$$\Delta H_C = \Delta H_{C,ox} \psi_O \tag{2.5}$$

where ψ_O is the stoichiometric oxygen to fuel mass ratio:

$$\psi_O = \frac{\nu_{O_2} W_{O_2}}{W_F} \tag{2.6}$$

where W_{O_2} and W_F is the weight of the oxygen and fuel respectively. ν_{O2} is the stoichiometric coefficient for oxygen. The relationship can be useful when estimating the maximum energy output of a fire, when oxygen supply limits combustion [8]. Additionally, applying $\Delta H_{C,ox}$ is beneficial in that its value lies within a relatively narrow range for a broad range of fuels. For instance, many polymers attain values of approximately 13,1 kJ/g_{ox} [7].

2.2. Heat release rate and the design fire

The HRR, $\dot{Q}$, is the amount of heat supplied to a system per unit time by combustion. Heat is released as oxygen and fuel react to form combustion products. The rate of heat release may be described in terms of the product of the rate of fuel mass loss rate, $\dot{m}_f$, and heat of combustion per unit mass of fuel consumed, ΔH_C [9]:

$$\dot{Q} = \dot{m}_f \Delta H_C \tag{2.7}$$

The HRR is often viewed as the primary indicator of the "size" of the fire. As such, specifying representable values for the HRR in terms of fire modelling, requires careful consideration. The HRR is also subject to time evolution. In an enclosure, this evolution can roughly be described in terms of four stages/phases: fire growth (1), flashover (2), fully developed fire or steady phase (3) and decay (4). These phases are often subject to qualitative evaluation. Also, the phases may overlap, the order rearranged, and some may never occur [9]. In terms of the design fire, in context of engineering, it is often sufficient to describe the HRR as time evolving until some steady state HRR is attained. In the literature and standards such as NFPA-Standards for Smoke and Heat Venting [10], the so-called alpha t-squared fire is proposed for representation of the time evolution of HRR:

$$\dot{Q} = \alpha t^2 \tag{2.8}$$

where α varies according to building type and/or commodities in the enclosure. In Table 2.1 a variety of growth rates are presented. Data is collected from SN-INSTA/TS 950:2014 [11].

Table 2.1 A variety of growth rates often used in Fire Safety Design. Adapted from [11]

Qualitative description of growth rate	α $[kW/s^2]$	Time [s] to reach 1055 kW
ultra-fast	0,19	75
fast	0,047	150
medium	0,012	300
slow	0,003	600

The HRR-growth continues until maximum attainable HRR is reached. The limiting factors are generally associated with oxygen supply and/or fuel supply. SN-INSTA/TS 950:2014 [11] suggests the former. A simple expression for air mass flow rate, $\dot{m}_a$, (in [kg]), through an opening is [9]:

$$\dot{m}_a = 0{,}5 A_o \sqrt{H_o} \tag{2.9}$$

where A_o is the area of the opening and H_o is its height. Expressing eq. 2.7 in terms of $H_{C,ox}$ and mass entrainment rate of oxygen, $\dot{m}_{ox}$, and combining it with 2.9, the maximum attainable HRR due to oxygen entrainment may be estimated (adapted from [9]):

$$\dot{Q}_{max} = 1{,}506 A_o \sqrt{H_o} \tag{2.10}$$

using $H_{C,ox}$ =13,1 MJ/kg, and a mass fraction of oxygen in air of 0,23 kg/kg. Combining eq. 2.8 and 2.10 may subsequently facilitate a simple design fire. In Figure 2.1, a door opening of 2,0 m^2 and 1,2 m in width is used as an example. Two HRR curves for medium- and fast-growing fires (Table 2.1) are plotted against time.

Figure 2.1 Exemplified HRR design fire.

Naturally, the smooth HRR evolution in the above plot is vastly simplified compared to real accidental fires. In Figure 2.2, an example of measured HRR evolutions are shown [12]. In the associated experiment, a collection of different chairs is burnt. The HRR evolution in time is far more fluctuating and the peak HRR is followed by a rapid decline. However, the experiment is likely conducted in a facility ensuring that oxygen supply is not limiting the HRR evolution (as is the case in Figure 2.1). Note that the horizontal time- axis is also spanning an interval approximately 2,5 times that of Figure 2.1, making for a more compressed appearance of the HRR increment and decline.

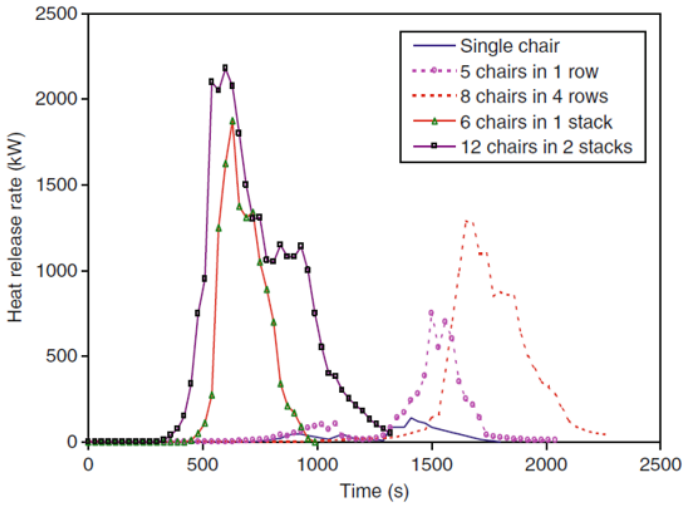

Figure 2.2 Heat release rate curves of stacked chairs. The chairs have steel frames, made of polypropylene, with no padding. From [12].

2.3.Computational Fluid Dynamics

CFD is a term used for the science of predicting the behavior of fluid flow and associated phenomena. It has been applied in a variety of software packages, in several different sciences and engineering fields. These being, for instance, meteorology, climate science, aircraft design and Fire Safety Design [13].

2.3.1. The governing equations

CFD represent the fundamental laws of fluid behavior through a set of conservation equations for mass, momentum and energy. The equation for mass conservation can be expressed as [14]:

$$\frac{\partial \rho}{\partial t} + \nabla \cdot \rho \boldsymbol{u} = 0 \tag{2.11}$$

where ρ and $\boldsymbol{u}$ is the density and velocity vector respectively. It merely states that the change of density over time, $\frac{\delta \rho}{\delta t}$, at a given point in space, equals the net mass flux, $\rho \boldsymbol{u}$, across the boundary of a volume surrounding the point. The expressions on the left-hand side of eq. 2.11 may also be referred to as accumulation rate and convective transport respectively [14].

A notation for the conservation of momentum can be described compactly as:

$$\frac{\partial (\rho \boldsymbol{u})}{\partial t} + \nabla \cdot (\rho \boldsymbol{u}\boldsymbol{u}) = -\nabla \mathrm{p} + \boldsymbol{f} + \nabla \cdot \tau \tag{2.12}$$

Newton's Second Law of Motion states that the rate of change of momentum equals the sum of the forces of the fluid. The driving forces of the fluid is the pressure gradient, $\nabla \mathrm{p}$, external forces, $\boldsymbol{f}$, for instance buoyancy, and friction. The latter is expressed as the viscous stress tensor, τ [14]. Viscosity, μ, is indicative of how strenuous the motion of different flows of molecules are to each other. Thus, it can be considered friction between fluids. A larger value indicates a larger exertion of shear stress between flows. For Newtonian fluids, shear stress increases linearly by strain rate, or velocity gradient [15]:

$$\tau = \mu \frac{dv}{dy} \tag{2.13}$$

The conservation of energy states that the change in sensible enthalpy, h_s, at a given point in space, equals the net energy flux, $\rho h_s \boldsymbol{u}$, across the boundary of a volume surrounding the point. For fire applications, a few additional source terms (terms added to the conservation equations, often in reference to the origin of a variable) need to be included on the right-hand side of the expression [14]:

$$\frac{\partial (\rho h_s)}{\partial t} = \nabla \cdot (\rho h_s \boldsymbol{u}) = \frac{Dp}{Dt} + \dot{q}''' - \nabla \cdot \dot{\boldsymbol{q}}'' + \varepsilon \tag{2.14}$$

These source terms are related to change in pressure, p, HRR by combustion, $\dot{q}'''$, thermal conduction and radiation vector, $\dot{\boldsymbol{q}}''$, and dissipation of kinetic energy, ε, respectively [14].

As the momentum equation really consists of three equations, one for each velocity component (u, v and w), the equations 2.11, 2.12 and 2.14 constitutes five partial differential equations (PDE's). These PDE's, however, contain six unknowns. These being the three velocity components, pressure, density and

temperature. A set of equations is therefore needed to close the system, here by relating sensible enthalpy to pressure. For the latter, an equation of state, assuming a perfect gas, will suffice for fire applications [14]:

$$p = \frac{\rho \Re T}{\bar{W}}; \bar{W} = \frac{1}{\sum\left(\frac{Y_\alpha}{W_\alpha}\right)} \tag{2.15}$$

where $\bar{W}$ is the mean molecular weight of a gaseous mixture consisting of a set of species α, with mass fractions Y_α, and $\Re$ being the universal gas constant [14].

Further, the *sensible* enthalpy is a function of specific heat, c_p, and temperature [14]:

$$h_s = \int_{T_0}^{T} c_p \, dT \tag{2.16}$$

The above equations constitute the framework for any CFD code. Applying the governing equations, however, require further assumptions and simplifications. The source terms also need sub models for closure, turbulent structures need to be accounted for and a variety of numerical schemes needs implementation. The methods of incorporating these aspects also vary according to the intent of the CFD code [14].

2.3.2. Turbulence modelling

One of the most crucial aspects for consideration in CFD, is the treatment of turbulence. In large-scale fire scenarios, heat and combustion products are primarily transported via convection. However, diffusive mechanisms are increasingly dominant in smaller scales, i.e. near boundaries and flames. Due to the difference in spatial scaling for the different processes of importance, capturing these correctly vastly increases computational time. To account for this, different turbulence models have been developed as surrogates for the effects occurring at the smallest spatial and temporal scales. These turbulence models are generally categorized by their spatial and temporal fidelity. The most common models are Direct Numerical Simulation (DNS), Reynolds-Averaged Navier-Stokes (RANS) and Large Eddy Simulation (LES) [14]. These are briefly described below.

DNS

As the name implies, DNS applies a direct numerical approach to the governing equations. No adjustments are made as to the resolution of the temporal and spatial scales. Thus, there is no need for sub models to incorporate diffusive terms, such as viscosity, thermal conductivity and material diffusivity. This requires temporal and spatial scales in the Kolmogorov-regime, where turbulent energy dissipates into heat by viscosity. For practical engineering applications, these scales require too much computing recourses, as the spatial and temporal resolution normally is less than 1 mm and 1 ms, respectively [14].

RANS

RANS approach the conservation equations by way of statistically time averaging. It decomposes the mass fractions, velocity components and enthalpy into time averaged, $\bar{\phi}(\boldsymbol{x}, t)$, and fluctuating, $\phi'(\boldsymbol{x}, t)$, components. Summing these components yields the variable, $\phi(\boldsymbol{x}, t)$, of consideration [14]:

$$\phi(\boldsymbol{x}, t) = \bar{\phi}(\boldsymbol{x}, t) + \phi'(\boldsymbol{x}, t) \tag{2.17}$$

Subsequently, the decomposed primitive variables are substituted into the governing equations. The same time averaging process is then applied to the system of equations, in its entirety, generating a new set of equations that resembles the originals. The mass conservation equation remains the same, but the equations for energy- and momentum conservation now have additional terms. As an example, consider the equation for momentum conservation, eq. 2.12. When applying the procedure described above, the equation is somewhat altered, and the fluctuating term, $\nabla \cdot \rho \overline{\boldsymbol{u}'\boldsymbol{u}'}$, is added [14]:

$$\frac{\partial(\rho \overline{\boldsymbol{u}})}{\partial t} + \nabla \cdot (\rho \overline{\boldsymbol{u}} \overline{\boldsymbol{u}}) = -\nabla \rho + \boldsymbol{f} + \nabla \cdot \bar{\tau} - \nabla \cdot \rho \overline{\boldsymbol{u}'\boldsymbol{u}'} \tag{2.18}$$

This term is referred to as the Reynold's stresses. Similarly, in the equation for energy conservation, the turbulent scalar flux, $\nabla \cdot \rho \overline{\boldsymbol{u}' h_s'}$, is added. As these additional terms represent additional unknowns for the conservation equations, further closure models are required [14].

LES

The derivation of the RANS and LES models are rather similar but differ in the treatment of the decomposition of the primitive variables, $\phi(\boldsymbol{x}, t)$. Whereas RANS emphasize temporal averaging, LES is developed for spatial averaging, or filtering. The effect of the small, filtered flows are then modelled, as opposed to numerically solving the conservation equations for the flow (in DNS). The general idea is to represent the smallest fluctuations and the dissipation of energy through turbulence via diffusive terms. The smallest fluctuations can also be referred to as the smallest resolvable eddies. What is meant by this, is illustrated in Figure 2.3 [14].

As to filtering, in FDS for instance, this is parametrized by the spatial interval $\Delta = (\delta x \delta y \delta z)^{1/3}$. δx is the spatial interval of a grid cell (see section 2.4.1.) in the x-direction. Roughly, the LES filters can be considered cell means. As an example, the filtered density in the x-direction can be expressed as [16]:

$$\bar{\rho}(x, t) = \frac{1}{\Delta} \int_{x-\frac{\Delta}{2}}^{x+\frac{\Delta}{2}} \rho(r, t) dr \tag{2.19}$$

where r represent the spatial dimensions x, y, z. Further inquiries as to the estimation of the unresolved viscous and diffusive terms through LES are made in section 2.4.2.

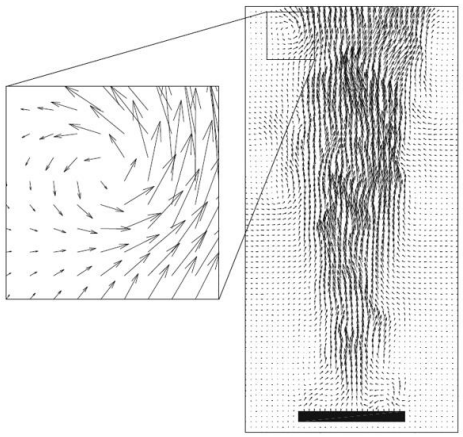

Figure 2.3 This figure exemplifies the smallest resolvable eddies, through a velocity vector field in a fire plume. The distance between the arrows indicates the grid cell size. From [14].

2.4. Fire Dynamics Simulator

FDS is a CFD code specially designed for fire applications. It numerically solves the governing equations for thermally-driven, low velocity flows. It's an open source code, which entails a vast number of users, consisting of scientists, engineers and forensic investigators. Turbulence is often modelled through LES, but options exist to employ both RANS and DNS [17].

In February 2000, the first version of the code was released to the public. Since then, it has been subject to major updates, and to date (fall of 2018) the latest version is FDS 6.7.0. FDS is developed and maintained mostly by the National Institute of Standards and Technology (NIST) and VTT Technical Research Centre of Finland. These institutes have also created a program for visualization of the solution to a FDS simulation, Smokeview (SMV) [17].

In this section, inquiries are made as to basics of FDS meshing, validation and incorporation of sub-grid scale flux terms in LES (2.4.1 and 2.4.2). Further, from section 2.4.3 to 2.4.8, key aspects of the FDS transport equations for mass, energy and momentum are described. Finally, section 2.4.9 show how these are combined to temporally evolve solutions to the mass transport equations and constituent variables.

2.4.1. Meshing and validation

FDS applies the Finite Volume Method (FVM), i.e. dividing the simulated volume into several sub-volumes, to solve the governing equations. This requires the specification of a numerical grid, referred to as a mesh. The mesh consists of a collection of rectilinear volumes, referred to as grid cells, as shown in Figure 2.4. The size and number of these cells dictate the computational cost of the simulation and the quality of the numerical solution [17].

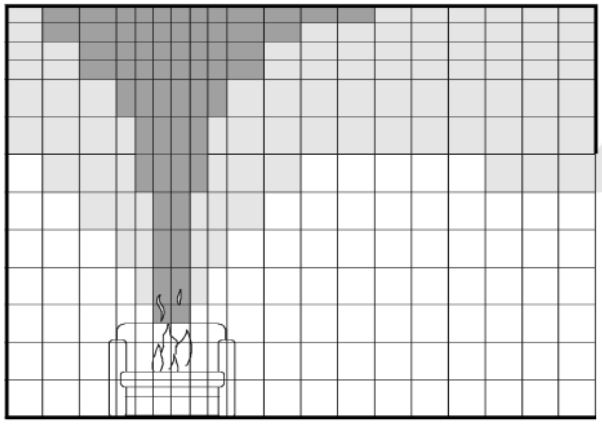

Figure 2.4 Illustration of the meshing concept. An enclosure is divided into several rectilinear volumes. From [9].

The appropriate size of the grid cells can be estimated through a grid sensitivity study (GSS). The procedure of a GSS is generally to preform several simulations of the same scenario, gradually increasing the grid resolution between simulations. If the results between simulations are appreciatory similar, further decrease of cell sizes is generally not necessary. The relationship between the characteristic flame diameter, D^*, and cell size, δx, is often applied when considering what grid cell size is appropriate for initiation of the GSS. The characteristic flame diameter can be expressed by [17]:

$$D^* = \left(\frac{\dot{Q}}{\rho_\infty c_p T_\infty \sqrt{g}}\right)^{\frac{2}{5}} \tag{2.20}$$

Where ρ_∞, T_∞ and c_p is the ambient density and temperature, and the heat capacity of air respectively, and g is the gravitational acceleration. A large value of $\frac{D^*}{\delta x}$ indicates high resolution. In the literature, values of 4, 10 and 16 may often be considered as coarse, medium and fine grid resolutions, respectively [18]. However, such values are merely suggestive, and does not preclude a GSS. The meticulousness of the GSS depend on the quantity of interest and what level of uncertainty may be deemed acceptable for the particular scenario

In addition to the GSS, there are methods of reducing the uncertainty regarding simulation results. This for instance, by comparing the scenario to validated scenarios. Scenarios are generally validated by the model developer. A validity study often encompasses (1) comparing simulation results with measurements from experiments, (2) quantifying the differences, also regarding uncertainties, and (3) determining applicability of the experiment. As to the latter, this can be done by use of dimensionless groups and other key parameters of the fire scenario. If the simulated scenario resembles validated scenarios in terms of these parameters, the uncertainty of the simulation results may be reduced. In addition to comparing validated cases to the simulation at hand, these parameters may also be employed in assessing the reasonability of simulation input. One such parameter is the fire Froude number, $\dot{Q}^*$ [19]:

$$\dot{Q}^* = \frac{\dot{Q}}{\rho_\infty c_p T_\infty \sqrt{gD} D^2} \tag{2.21}$$

where D is the flame diameter. The fire Froude number can be interpreted as the relationship between the fuel gas "exit" velocity and plume velocity induced by buoyancy. A value of unity is characteristic for accidental fires [19].

Another such parameter is the flame height. The flame height relative to the ceiling height is a parameter indicative of whether the flame impinges on the ceiling. Flame impingement might influence oxygen entrainment to the fire, as well as affecting activation of fire protection systems. The flame height can be estimated via Heskestad's correlation [19]:

$$L_f = D(3{,}7(\dot{Q}^*)^{\frac{2}{5}} - 1{,}02) \tag{2.22}$$

which is approximate to the flame height 50% of the time, due to pulsation. In addition to the fire Froude number and flame height, the possibilities for air entrainment in relation to HRR may be considered. This, for instance, through eq. 2.9 or 2.10, for natural ventilation [19].

2.4.2. Turbulent viscosity and diffusivity

The turbulence model in LES concerns closing the sub-grid scale flux terms. To close these terms, FDS requires a coefficient for turbulent transport, which can either be the turbulent viscosity or the turbulent diffusivity. FDS applies a procedure for modelling the turbulent viscosity, μ_t, and then using constant Schmidt and Prandtl numbers (dimensionless numbers for fluid properties [15]) to calculate the mass- and thermal diffusivities respectively [16].

In FDS, several models for obtaining the turbulent viscosity, μ_t, is available. By default, FDS uses a variation the Deardorff model:

$$\mu_t = \rho C_v \Delta \sqrt{k_{sgs}} \tag{2.23}$$

where k_{sgs} is the sub-grid kinetic energy per unit mass:

$$k_{sgs} = \frac{1}{2}((\bar{u} - \hat{\bar{u}})^2 + (\bar{v} - \hat{\bar{v}})^2 + (\bar{w} - \hat{\bar{w}})^2) \tag{2.24}$$

where

$$\bar{u}_{ijk} = \frac{u_{ijk} + u_{i-1,jk}}{2} \tag{2.25}$$

which is the average velocity at the center of the grid cell, ijk. The letters ijk are notations for spatial orientation (x, y, z-directions respectively) of a variable-component. The variable $\hat{\bar{u}}_{ijk}$, may be considered an average velocity, weighted about the adjacent grid cells, $i-1, jk$ and $i+1, jk$. It is solved by:

$$\hat{\bar{u}}_{ijk} = \frac{\bar{u}_{ijk}}{2} + \frac{\bar{u}_{i-1,jk} + \bar{u}_{i+1,jk}}{4} \tag{2.26}$$

The terms for the remaining velocity components, v and w, are defined in a similar fashion. FDS uses a constant value of $C_v = 0{,}1$, in eq. 2.23 [16].

The turbulent viscosity is further employed to compute the mass diffusivity, D. Diffusion is the migration of species due to mass concentration gradients [15]. Its related to turbulent viscosity by [16]:

$$(\rho D)_t = \frac{\mu_t}{Sc_t} \tag{2.27}$$

where Sc_t is the turbulent Schmidt number. Based on smoke plume simulations, FDS applies a constant value of $Sc_t = 0{,}5$.

Additionally, the turbulent viscosity is applied to calculate the thermal diffusivity, α. Thermal diffusivity can be interpreted as the thermal inertia of a substance [15]. Its relation to turbulent viscosity is [16]:

$$(\rho \alpha)_t = \frac{\mu_t}{Pr_t} \tag{2.28}$$

where Pr_t is the turbulent Prandtl number. Similar to the Schmidt number, the Prandtl number attains a constant value of 0,5.

2.4.3. The lumped species approach

The method of which FDS retrieves mass quantity information from the simulated mass flow in the computational domain is presented in this section.

As a fire is a relatively inefficient combustion process, there is a vast number of species generated from a combustion reaction. Every such species transports differently, and therefore, ideally, require a separate transport equation. Further, in a typical building fire, there are a variety of different fuels involved in the fire. As each of these fuels undergo combustion, there are hundreds of sub reaction steps involved. To avoid spending enormous computing power to track all these reactions and transport of individual species, simplifications needs to be made [16].

As to the reactions, most of the energy release can be accounted for using just one, or a few, reactions. In engineering applications, the associated properties of the flow are often of interest, in more of a macro-scale. Therefore, the energy contributions, and effect on the general flow are simplified without considering hundreds of sub-reactions [16].

When assuming only a single-step reaction on the form:

$$Fuel + Air \rightarrow Products \tag{2.29}$$

the necessity to explicitly solve the transport equations for every individual gas species (O_2, CO_2, N_2, for instance) is reduced. Rather, the transport equations can be related to the flow of fuel, air and products. To be realizable (in this context: mass is conserved), the sum of the mass fractions of these constituents need to equal unity. This reduces the number of necessary transport equations to two; one for the fuel and one for the products. The remaining constituent, air, is neither fuel nor products, and can subsequently be found by requiring realizability [16].

Although the fuel can often be considered as a single gas species, the products and air are collections of several gases. As such, the air and products are referred to as "lumped species". Still, the lumped species is transported as one, and therefore have a single set of properties associated with transport. Naturally, this is not the case for real flows, but the simplification often holds reasonably well [16].

Through the lumped species approach, retrieving information about the distribution of the primitive gas species in the flow, is a simple matter of performing a matrix operation. The relationship between the mass fractions of primitive and lumped species (Z_{air}, Z_{fuel} and $Z_{products}$) can be expressed via a transformation matrix A as follows [16]:

$$\boldsymbol{Y} = A\boldsymbol{Z} \tag{2.30}$$

where $\boldsymbol{Y}$ represent the matrix containing the mass fractions of the primitive species. The matrix A consists of N_y rows and N_z columns, the elements of which corresponds to mass fractions, $a_{\alpha,i}$, of the primitive species, α, in the lumped species, i [16]:

$$a_{\alpha,i} = \frac{\nu_{\alpha,i} W_\alpha}{\sum_\beta \nu_{\beta,i} W_\beta} \tag{2.31}$$

where ν and W represents volume fractions and molecular weights respectively. In the denominator, β refers to the primitive species in lumped species, i. For instance, consider the combustion reaction of methane in air [16]:

$$CH_4 + 2O_2 + 7{,}52N_2 \rightarrow CO_2 + 2H_2O + 7{,}52N_2 \tag{2.32}$$

As an example, if in a given grid cell, the lumped species of air, a, fuel, f, and products, p, are assumed to be distributed as

$$\boldsymbol{Z} = [Z_a \quad Z_f \quad Z_p]^T = [0{,}8 \quad 0{,}05 \quad 0{,}15]^T \tag{2.33}$$

then the mass fractions of the primitive species may be retrieved as such:

$$\boldsymbol{Y} = \begin{bmatrix} Y_{O_2} \\ Y_{N_2} \\ Y_{CH_4} \\ Y_{CO_2} \\ Y_{H_2O} \end{bmatrix} = \begin{bmatrix} 0{,}2330 & 0 & 0 \\ 0{,}7670 & 0 & 0{,}7248 \\ 0 & 1 & 0 \\ 0 & 0 & 0{,}1514 \\ 0 & 0 & 0{,}1238 \end{bmatrix} \begin{bmatrix} 0{,}8 \\ 0{,}05 \\ 0{,}15 \end{bmatrix} = \begin{bmatrix} 0{,}18664 \\ 0{,}72232 \\ 0{,}05 \\ 0{,}02271 \\ 0{,}01857 \end{bmatrix} \tag{2.34}$$

The mass fractions on the right-hand side of eq. 2.34 may also be solved by:

$$Y_\alpha = Z_a \cdot a_{\alpha,a} + Z_f \cdot a_{\alpha,f} + Z_p \cdot a_{\alpha,p} \tag{2.35}$$

Note that, as default, FDS includes trace amounts of water vapor (H_2O) and carbon dioxide (CO_2) in air. In eq. 2.34, this is neglected for simplicity. Further, other primitive species such as soot (when treated as a gas) and CO is often prescribed as constituents of the products [16].

The expression for transport of a lumped species and a primitive species is formulated [12]:

$$\frac{\partial}{\partial t}(\rho Z_\alpha) + \nabla \cdot (\rho Z_\alpha \boldsymbol{u}) = \nabla \cdot (\rho D_\alpha \nabla Z_\alpha) + \dot{m}'''_\alpha + \dot{m}'''_{b,\alpha} \tag{2.36}$$

where the first and second term on the left-hand side of the equation is the accumulation rate and convective transport respectively. The first term on the right-hand side is the diffusive transport. The two second terms on the right-hand side, $\dot{m}'''_\alpha$ and $\dot{m}'''_{b,\alpha}$, are the mass source terms. They are distinguished by the method of which mass is formed. $\dot{m}'''_\alpha$ is the source term for mass produced by combustion, while $\dot{m}'''_{b,\alpha}$ represents mass formed by evaporation. In many applications, however, only mass production is considered [16].

Equation 2.36 is paramount in studying the flow of smoke and its constituents. In section 2.4.9, the procedure of computing this equation is presented.

2.4.4. Stoichiometry

FDS facilitate several ways to specify and compute stoichiometry and combustion chemistry. When the intent of the simulation is merely to study the transport of smoke and heat, stoichiometry can be simplified [16]. In this context, the approach referred to as simple chemistry is often used. In FDS, this is the default chemical reaction equation, defined [16]:

$$\nu_a(Air, Z_a) + \nu_f\big(Fuel, Z_f\big) \rightarrow \nu_p\big(Products, Z_p\big) =$$

$$\nu_a\big(\nu_{O_2,a}O_2 + \nu_{N_2,a}N_2 + \nu_{H_2O,a}H_2O + \nu_{CO_2,a}CO_2\big) + \nu_f\big(C_xH_yO_zN_v\big) \rightarrow \tag{2.37}$$

$$\nu_p\big(\nu_{H_2O,p}H_2O + \nu_{CO_2,p}CO_2 + \nu_{N_2,p}N_2 + \nu_{CO,p}CO + \nu_{S,p}Soot\big)$$

The lumped species, $i = a, f, p$, contains the volume fraction of the primitive species, α, denoted $\nu_{\alpha,i}$ (applied in eq. 2.31). The lumped species' stoichiometric coefficients are denoted by ν_i. The subscripts x, y, z and v refer to the number of atoms of carbon, hydrogen, oxygen and nitrogen in the fuel respectively [16].

The yields of CO, γ_{CO}, and soot, γ_S, also need to be specified, along with the hydrogen fraction of soot, X_H (default value is 0,1). The yield of a species α is defined by the following relationship [16]:

$$\gamma_\alpha = \frac{mass\ of\ the\ species\ \alpha\ in\ products}{mass\ of\ fuel\ reacted} \tag{2.38}$$

In FDS, the user may also specify several combustion reactions in one simulation. The method requires different fuels to be specified, along with their respective products. For two reactions, this require FDS to transport four lumped species; two fuels and two products (no transport equation needed for air, see section 2.4.3) [16]. To reduce the amount of transport equations, a simplified alternative method may be applied. This entails merging the fuels into one, referred to as a surrogate fuel. In general, when using the surrogate fuel-method, a volumetric percentile-distributed, F, surrogate fuel-variable, Φ, can be described as [20]:

$$\Phi = F(\Phi_1 - \Phi_2) + \Phi_2 \tag{2.39}$$

when the surrogate fuel properties are merged from two fuels. For instance, if two fuels, 1 and 2, contains two and four carbon atoms respectively, the surrogate contains:

$$\Phi_C = 50\%(2 - 4) + 4 = 3$$

assuming a volumetric percentile-distribution, $F = 50\%$. The same procedure is applied for the remaining fuel-specific variables [20].

2.4.5. Aerosol deposition and treatment of soot

By default, FDS transports soot as any other gaseous species. This entails treatment as a gas and no deposition. However, by enabling aerosol transport, FDS facilitates the means of treating soot as a particulate and the modelling of deposition of soot onto surfaces. Deposition mechanisms applied in FDS are gravitational settling, thermophoresis (movement towards or away from walls due to temperature gradients), diffusive deposition (migration due to concentrations gradients) and turbulent deposition (deposition due to impact). The deposition velocity of aerosols, u_{dep}, can be expressed [16]:

$$u_{dep} = u_g + u_{th} + u_{dt} \tag{2.40}$$

where the subscript g, th, and dt are the gravitational, thermophoretic and combined diffusive-turbulent deposition velocities respectively. The gravitational and thermophoretic deposition velocities are added to the convective velocity term in the species mass transport equation (eq. 2.36). As such, the transport velocities for any species transported as an aerosol, is altered compared to species transported as gases. The differences in overall velocity are, however, often small due to the comparably large convective velocity [16].

The deposition velocities results in the deposition mass flux [16]:

$$\dot{m}''_{dep,\alpha} = \rho Y_\alpha u_{dep} \tag{2.41}$$

where ρY_α is the mass density of species α. When mass is deposited onto surfaces, this mass is omitted from further transport. Applying deposition mechanisms also require specification of aerosol properties, unless default properties are sufficient. These being the aerosol density, thermal conductivity and mean diameter [16]. Default properties are 1800 kg/m^3, 0,26 W/mK and 1,0 µm [17].

As the mass deposition mechanisms remove mass from the simulation, deposition effectively acts like a mass sink (which entails adding a negative mass source term to eq. 2.36). For the case of soot, this may increase the visibility distance, S. This due to soot being the most important factor for light obscuration through smoke. In FDS, the visibility distance through smoke is estimated via [17]:

$$S = \frac{C}{K_m \rho Y_S} \tag{2.42}$$

where ρY_S is the soot density and K_m is a constant representing the mass extinction coefficient. Its value is 8700 m^2/kg by default, approximately representative for combustion of wood and plastics. The visibility factor, C, is a non-dimensional factor representative for the object viewed through the smoke. Its default value is 3, which can be representative for a light-reflecting sign. A value of 8 is also suggested in the FDS User Guide [17], as representative for a light-emitting sign.

2.4.6. Energy transport

The neglection of high-speed flows (i.e. flows with a high Mach number) enables the relation between internal energy, e, and *specific* enthalpy, h. The relation is made through the thermodynamic pressure, or rather the background pressure, $\bar{p}$, and can be expressed [16]:

$$h = e + \frac{\bar{p}}{\rho} \tag{2.43}$$

The thermodynamic pressure gets its name from its relation to temperature by the ideal gas law [16]:

$$\bar{p} = \rho \Re T \sum_{\alpha} \frac{Z_\alpha}{W_\alpha} \equiv \frac{\rho \Re T}{\bar{W}} \tag{2.44}$$

This relation enables the connection between the density of the flow and the energy conservation equation, written in terms of *sensible* enthalpy, h_s [16]:

$$\frac{\partial}{\partial t}(\rho h_s) + \nabla \cdot (\rho h_s \boldsymbol{u}) = \frac{D\bar{p}}{Dt} + \dot{q}''' + \dot{q}_b''' - \nabla \cdot \dot{\boldsymbol{q}}'' \tag{2.45}$$

where $\dot{q}'''$ is the HRR originating from combustion, and $\dot{q}_b'''$ represent the energy transfer rate to droplets and particles (sub-grid scale). $\dot{\boldsymbol{q}}''$ consists of the heat fluxes due to thermal conduction, diffusion, and radiation [16]:

$$\dot{\boldsymbol{q}}'' = -k\nabla T - \sum_{\alpha} h_{s,\alpha} \rho D_\alpha \nabla Z_\alpha + \dot{\boldsymbol{q}}_{\boldsymbol{r}}'' \tag{2.46}$$

where k is the thermal conductivity. For high temperature smoke flows, thermal radiation is generally the dominant form of heat transfer. Thermal radiation also generally increases when the soot content of the smoke increases, due to the emissivity of soot [9]. FDS does not explicitly solve the energy conservation equation, eq. 2.45. Rather it's solved by the divergence of velocity:

$$\nabla \cdot \boldsymbol{u} = \frac{1}{\rho h_s}\left[\frac{D}{Dt}(\bar{p} - \rho h_s) + \dot{q}''' + \dot{q}_b''' - \nabla \cdot \dot{\boldsymbol{q}}''\right] \tag{2.47}$$

This equation enables FDS to advance flow transport in time by use of thermodynamic variables ρ, Z_α and $\bar{p}$ only [16].

2.4.7. Heat release rates

Typically, the HRR is the most important contributor to the velocity divergence and thereby has a major influence on the transport equations [16].

In Fire Safety Design, the intent of the fire simulation may merely be to predict the consequences of the transport of smoke and heat, from a fire with a specified HRR. In such a case, the user predetermines the HRR per unit area, $\dot{q}''_{user}$, (HRRPUA) and the heat of combustion, ΔH_c. The HRR may also be specified by a function for time evolution, $f(t)$. The time evolution of the HRR can be in the form of either a time ramp or a flame spread velocity. From these quantities, the mass flux of the fuel, $\dot{m}''_f$, is computed. The release of fuel is allocated to a surface, which can be considered a burner releasing the user specified species:

$$\dot{m}''_f = \frac{f(t)\dot{q}''_{user}}{\Delta H_c} \tag{2.48}$$

When using simple chemistry, the heat of combustion can be specified in terms of either fuel or oxygen consumption [16].

2.4.8. Momentum transport

The equation for conservation of momentum is, in FDS, articulated as follows [16]:

$$\frac{\partial \boldsymbol{u}}{\partial t} - \mathbf{u} \times \omega + \nabla \mathrm{H} - \tilde{p}\nabla(1/\rho) = \frac{1}{\rho}[(\rho - \rho_0)g + \boldsymbol{f}_b + \nabla \cdot \tau] \tag{2.49}$$

This notation is made to derive a Poisson equation for pressure. Simply put, this expression is derived via the vector identity:

$$(\boldsymbol{u} \cdot \nabla)\boldsymbol{u} = \frac{\nabla|\boldsymbol{u}|^2}{2} - \boldsymbol{u} \cdot \omega \tag{2.50}$$

and the definition of the mass specific stagnation energy:

$$H \equiv \frac{\nabla|\boldsymbol{u}|^2}{2} + \frac{\tilde{p}}{\rho} \tag{2.51}$$

In eq. 2.49, ω is the vorticity (the "curl" of the flow). The drag force originating from sub grid-scale particles is included by $\boldsymbol{f}_b$. The viscous stress, τ, is solved via FDS's viscosity model [16].

By expressing eq. 2.49 as:

$$\frac{\partial \boldsymbol{u}}{\partial t} + \boldsymbol{F} + \nabla \mathrm{H} = 0 \tag{2.52}$$

and taking its divergence, the Poisson equation for pressure can be derived [16]:

$$\nabla^2 H = -\left[\frac{\partial}{\partial t}(\nabla \cdot \boldsymbol{u}) + \nabla \cdot \mathbf{F}\right] \tag{2.53}$$

2.4.9. Solution procedure

In the following, FDS's solution procedure for advancing the transport of mass, and constituent variables, in time is shown. This assumes that there are existing known initial values for these variables at the *n*th time step. These are either calculated from previous time steps or ascertained from starting values when t=0. The variables, grid cell-specific, are the density, ρ^n, lumped species mass fractions, Z_α^n, velocity, $\boldsymbol{u}^n$, and the Bernoulli integral, H^n. The latter can be regarded as the total pressure divided by the density. The background pressure, $\bar{p}^n$, is specific to the enclosure in question. These variables are explicitly advanced in time by use of a second-order prediction/correction scheme. In the following, the asterisk $(*)$ indicates estimates of a first order accurate solution for the variable at the next time step, thus the predicted value. The solution procedure is as follows [16]:

Predictor steps

1. Via an explicit Euler step, ρ, Z_α and $\bar{p}$ is estimated for the next time step. Eq. 2.36 is used to make an estimation for the species density:

$$\frac{(\rho Z)_\alpha^* - \rho^n Z_\alpha^n}{\delta t} + \nabla \cdot \rho^n Z_\alpha^n \boldsymbol{u}^n = \nabla \cdot (\rho^n D_\alpha^n Z_\alpha^n) + \left(\dot{m}_\alpha''' + \dot{m}_{b,\alpha}'''\right)^n \tag{2.54}$$

2. The bulk density, ρ^*, of the mixture, is calculated, in addition to the mass fractions, Z_α^*, by equating:

$$\rho^* = \Sigma_\alpha (\rho Z_\alpha)^* \tag{2.55}$$

and

$$Z_\alpha^* = \frac{(\rho Z)_\alpha^*}{\rho^*} \tag{2.56}$$

3. With the mass fractions and densities computed, the temperature, T^*, is found from the ideal gas law (eq. 2.44).

4. By use of the computed thermodynamic quantities, the divergence, $(\nabla \cdot \boldsymbol{u})^*$(in eq. 2.47), derived from the solution for energy conservation (eq. 2.45), is estimated.

5. The Poisson equation for pressure, derived from the momentum equation, is solved. This by using the divergence of the velocity field from the previous step:

$$\nabla^2 H^n = -\frac{(\nabla \cdot \boldsymbol{u})^* - \nabla \cdot \boldsymbol{u}^n}{\delta t} - \nabla \cdot \mathbf{F}^n \tag{2.57}$$

6. Now, the actual velocity (not merely its divergence from step 4) can be computed.

$$\frac{\boldsymbol{u}^* - \boldsymbol{u}^n}{\delta t} + \boldsymbol{F}^n + \nabla H^n = 0 \tag{2.58}$$

7. After steps 1 through 6, FDS checks if criterions for stability constrains are satisfied. This concerns the size of the time step, δt. Instabilities might arise if this step is too large. If so, the time step is reduced, and the steps 1 through 6 is repeated. If stability is ensured, the corrector step ensues [16].

Corrector steps

The corrector steps are similar to the predictor steps. Now, however, the predicted quantities are included as input to the transport equations [16].

1. First, the transport equation for the densities is computed for time step *n+1*:

$$\frac{(\rho Z)_\alpha^{n+1} - \frac{1}{2}(\rho^n Z_\alpha^n + \rho^* Z_\alpha^*)}{\delta t/2} + \nabla \cdot \rho^* Z_\alpha^* \boldsymbol{u}^* = \nabla \cdot (\rho^* D_\alpha^* Z_\alpha^*) + \left(\dot{m}_\alpha''' + \dot{m}_{b,\alpha}'''\right)^n \tag{2.59}$$

The background pressure is computed in a similar fashion.

2. The bulk density and species mass fractions for the time step *n+1* are computed by:

$$\rho^{n+1} = \Sigma_\alpha (\rho Z_\alpha)^{n+1} \tag{2.60}$$

and

$$Z_\alpha^{n+1} = \frac{(\rho Z)_\alpha^{n+1}}{\rho^{n+1}} \tag{2.61}$$

3. Using these quantities, the temperature, T^{n+1}, can be equated from the ideal gas law.

4. From the values obtained from step 1 through 3, source terms for the HRR per unit volume, $\dot{q}'''$, net absorption/emittance of thermal radiation, $\nabla \cdot \dot{\boldsymbol{q}}''$, and the species source terms, $\dot{m}_\alpha'''$, are computed. These source terms are applied in the predictor/corrector steps for the next time step. The next time step is denoted, in this respect, *n+2*.

5. Using the values from step 1 through 3, the velocity divergence, $(\nabla \cdot \boldsymbol{u})^{n+1}$, is equated.

6. The pressure can thus be computed:

$$\nabla^2 H^* = -\left[\frac{(\nabla \cdot \boldsymbol{u})^{n+1} - \frac{1}{2}(\nabla \cdot \boldsymbol{u}^* + \nabla \cdot \boldsymbol{u}^n)}{\delta t/2}\right] - \nabla \cdot \mathbf{F}^* \tag{2.62}$$

7. Finally, the velocity is obtained [16]:

$$\frac{\boldsymbol{u}^{n+1} - \frac{1}{2}(\boldsymbol{u}^* + \boldsymbol{u}^n)}{\delta t/2} + \boldsymbol{F}^* + \nabla H^* = 0 \tag{2.63}$$

3. Methods

The methods of which simulations are correlated by use of correlation factors, are proposed and described in this chapter. The correlation factors are defined as functions of input parameters, significant to the solution to the mass transport equation (eq. 2.36). By use of these correlation factors and output from base simulations, it may be feasible to make reasonable estimations of simulation output from other simulations, applying different fuel parameters than the base simulation. The estimations are further compared to actual simulations that apply these different fuel parameters, facilitating evaluation of the performance and applicability of the correlation factors. Simulation scenarios applied to assess the performance of the correlation factors are also described in this chapter. These are simulation scenarios applying input parameters relating to those often specified in standards and codes applied in Fire Safety Design.

3.1. Correlation factors and estimated output

For a series of fire simulations with revised input parameters, a correlation factor (in this context) is defined as the ratio of functions of fuel input parameter values for two of these simulations. It is expected that such correlation factors may be used to estimate the species concentrations of a fire scenario, from the simulation results of a base fire scenario. This provided the functions account for aspects paramount to transport and mixing of mass in the computational domain. In this study, two correlation factors are derived. Correlation factor number 1 considers the source terms in the mass transport equations. The second, considers the method of which FDS retrieves information about the species output quantities.

In mathematical terms, the correlation factor, β_θ, is the ratio of functions of input parameters, I, from two simulations, a and b:

$$\beta_\theta = \frac{f(I_a)}{f(I_b)} \tag{3.1}$$

where *only* values of fuel input parameters differ. In this context, fuel parameters refer to chemical composition of the fuel, product species yields (such as CO and soot) and heat of combustion. If the functions account for major aspects of the solution to the mass transport equation (eq. 2.36), correlation factors may be expected to approximate the ratio of mass output quantities, θ, from simulation a and b:

$$\frac{f(I_a)}{f(I_b)} \approx \frac{\theta_a}{\theta_b} \tag{3.2}$$

where the position and time of measurement for both θ_a and θ_b are the same. Provided mass quantity output of one simulation is known, for instance b, output quantity of simulation a may thereby be estimated by combining eq. 3.1 and 3.2:

$$\theta_a \approx \theta_b \cdot \beta_\theta \tag{3.3}$$

The mass quantity can be, for instance, the species mass fraction, Y_α, or the species density, ρY_α. In this study, estimated mass quantities are of primitive species distinctive to product species by combustion. In the following, two different correlation factors are presented. Expanded versions of the equations are provided in Appendix A.1.

3.1.1. Correlation factor 1

Correlation factor 1, $\beta_{\theta,1}$, is calculated by using species mass production rates by combustion, which are source terms to the mass transport equations ($\dot{m}_\alpha'''$ in eq. 2.36). Unless, for instance, evaporation and deposition is invoked in the simulation, species mass production rates accounts for all mass of the primitive species distinctive to products, introduced to the computational domain. As such, the values of species mass production rates should highly affect product species mass quantity measurements of simulations. Provided the produced mass is transported similarly in both simulation a and b, increased/reduced mass production may lead to a similar increase/reduction in the measured species mass output quantity. By applying eq. 2.38, the species mass production rates, $\dot{m}_\alpha$ (for soot, CO, etc.), can be solved by:

$$\dot{m}_\alpha = \gamma_\alpha \dot{m}_f$$

where γ_α is the yield parameter for species α. Further, mass production rates may be expressed in terms of FDS fuel parameter input, by combining the above expression and eq. 2.5 through 2.7:

$$\dot{m}_\alpha = \frac{\gamma_\alpha \dot{Q}}{\left(\Delta H_{C,ox} \frac{\nu_{O_2,a} W_{O_2}}{W_F}\right)} \tag{3.4}$$

Alternatively, the denominator may also be expressed in terms of heats of formation. This approach is not taken, however, as values of $\Delta H_{C,ox}$ are often more easily attained and often rather constant (for many polymers $\Delta H_{C,ox} \approx 13{,}1\ kJ/g_{ox}$ [7]). The species mole weights, W, and oxygen stoichiometric coefficient, $\nu_{O_2,a}$, are also somewhat simple to calculate. The latter is calculated by balancing the chemical reaction of eq. 2.37 (adapted from [17]):

$$\nu_{O_2,a} = x + \frac{y}{4} - \frac{z}{2} + W_F \left(\frac{\gamma_S}{W_S}\left(\frac{3X_H}{4} - 1\right) - \frac{\gamma_{CO}}{2W_{CO}}\right) \tag{3.5}$$

where x, y and z are the numbers of atoms of carbon, hydrogen and oxygen in the fuel respectively. Calculations of species mole weights are provided in Appendix A.1.

Replacing the general mass parameter function, $f(I)$, with the species mass production rates, $\dot{m}_\alpha$, allows equation 3.1 to be expressed in terms of $\beta_{\theta,1}$:

$$\beta_{\theta,1} = \frac{\dot{m}_{\alpha,a}}{\dot{m}_{\alpha,b}} \tag{3.6}$$

Output quantity θ_a may thereby be estimated from the base simulation output, θ_b, and correlation factor $\beta_{\theta,1}$, by substituting these expressions into equation 3.3:

$$\theta_a \approx \theta_b \cdot \beta_{\theta,1} \tag{3.7}$$

The correlation factor only accounts for species mass production rates, and not the manner of which it is transported. Alterations in transport mechanisms between simulation a and b may, for instance, be due to different solutions to the transport equations for energy and momentum. Causations between such mechanisms and estimation discrepancies are, however, best evaluated through simulations.

Also notice that even if correlation factor 1 involves the term for HRR, $\dot{Q}$, this value is held constant between simulation a and b (in this study). This due to the relation between HRR and the velocity divergence (eq. 2.47), possibly affecting the solution to the FDS mass transport equations significantly.

3.1.2. Correlation factor 2

Correlation factor 2, $\beta_{\theta,2}$, is calculated by use of the primitive species mass fractions of products, $a_{\alpha,p}$. The correlation factor utilizes the method of which FDS retrieves information about mass quantity output. FDS solves the primitive species mass fractions, Y_α, by use of the mass fractions of the ith transported lumped species, Z_i, and the mass fractions of the primitive species in every lumped species, $a_{\alpha,i}$. The procedure is illustrated in section 2.4.3. For a species only produced by combustion, the mass fraction of the species can be solved through eq. 2.35:

$$Y_\alpha = Z_p a_{\alpha,p}$$

The mass fraction of the lumped product species, Z_p, is solved through the species transport equations in FDS. The mass fraction of the primitive species, $a_{\alpha,p}$, however, is solved by the simple hand-calculation of eq. 2.31. For two similar scenarios, provided the relative change in Z_p is considerably less between simulation a and b, than $a_{\alpha,p}$, the ratios of $a_{\alpha,p,a}$ to $a_{\alpha,p,b}$ should approximate the ratios of $Y_{\alpha,a}$ to $Y_{\alpha,b}$. In mathematical terms, the *relative difference* between the solutions to the transport equations of $Z_{p,a}$ and $Z_{p,b}$ may be neglected, provided that:

$$\left|\frac{Z_{p,b} - Z_{p,a}}{Z_{p,b}}\right| \ll \left|\frac{a_{\alpha,p,b} - a_{\alpha,p,a}}{a_{\alpha,p,b}}\right| \tag{3.8}$$

which in turn signify:

$$\frac{Y_{\alpha,a}}{Y_{\alpha,b}} \approx \frac{a_{\alpha,p,a}}{a_{\alpha,p,b}} \tag{3.9}$$

This is the basis for correlation factor 2. Replacing $f(I)$ with eq. 2.31, in eq. 3.1, thereby yield correlation factor 2:

$$\beta_{\theta,2} = \frac{a_{\alpha,p,a}}{a_{\alpha,p,b}} \tag{3.10}$$

Output quantity θ_a may thereby be estimated from the base simulation output, θ_b, and the correlation factor $\beta_{\theta,2}$, by substituting these expressions into equation 3.3:

$$\theta_a \approx \theta_b \cdot \beta_{\theta,2} \tag{3.11}$$

In the above expression, the species mass fraction, Y_α, is exchanged with the general expression θ, meaning that the correlation factor is (in this study) also used to estimate other mass quantity outputs than Y_α. For instance, the expression may yield reasonable estimations for species densities, ρY_α, provided that the relative change in density between simulation a and b is considerably less than the relative change in the mass fraction of the primitive species, $a_{\alpha,p}$:

$$\left|\frac{\rho_b - \rho_a}{\rho_b}\right| \ll \left|\frac{a_{\alpha,p,b} - a_{\alpha,p,a}}{a_{\alpha,p,b}}\right| \tag{3.12}$$

which is the same criterion as for the lumped species mass fractions, Z_p. Thereby, for species density estimations, discrepancies may increase if densities change in the same direction and decrease if changed similarly in opposite directions, between simulation a and b.

Eq. 2.31, used to calculate $a_{\alpha,p}$, accounts for the mole weights of the species and the products. It does not, however, account for the rate of which mass is produced. The estimation discrepancies of correlation factor 2, and thereby the differences to the solutions of Z_p and/or ρ between simulation a and b, may therefore partly be attributed to alterations in mass production rates. Additionally, similar to correlation factor 1, correlation factor 2 does not account for transport of momentum and energy, potentially prone to alter mass transport mechanisms.

3.1.3. Estimated output quantities

This study will consider mass quantity output often of interest in Fire Safety Design. As FDS employs the lumped species approach, and the estimation accuracy may therefore generally be similar for any primitive species in the same "lump", the choice of estimated species is relatively arbitrary. However, there may be differences regarding the estimated quantity variable, for instance density or mass fraction. The former may be prone to change due to expansion of gases via the relation between temperature and density, asserted through the ideal gas law (eq. 2.44). However, as gases expand, the mass fractions may remain relatively constant, provided mixing due to expansion is limited. As such, both density quantities and mass fractions are assessed.

Regarding egress, soot content of the smoke is relevant for assessing the visibility distance. In the equation for the visibility distance, eq. 2.42, soot content is encompassed in terms of soot density, ρY_S. As such, the soot density output of simulations is subjected to estimation by use of the correlation factors. Additionally, successful egress may depend on the CO content of the smoke. High levels of CO may cause asphyxiation, possibly resulting fatalities [5]. In addition to the soot density, the CO mass fraction, Y_{CO}, is assessed.

As to the form of output, time history recordings of the quantities are required in stationary positions. FDS facilitate numerus manners of data recording, the DEVC (device) Name-list groups being most suitable for the purpose of this study. The DEVC Name-list group, enables measurements in stationary points, lines or volumes in the simulated scenario [17]. Stationary points and lines, however, only record data representable for values in a limited amount of grid cells. As such, estimation accuracy may be misrepresented. Therefore, the volume-devices are more suitable. In FDS, such devices allow for spatially integrated time histories, facilitating statistical mean and maximum values of the quantity measured for the grid cells in a specified volume [17]. Such measurements may also be of interest regarding Fire Safety Design. Mean values allow for representation of the quantity of interest for a larger volume rather than only a few stationary points. Maximum values allow for evaluation through a more conservative approach, in terms of the species effects on humans.

To summarize, the statistical *volumetric* mean and maximum values are assessed for both soot densities and CO mass fractions (four mass quantity outputs in total). Inquiries as to the locations of measurements are made in section 3.2.3 and 3.2.4. Estimation precision of all quantities will be made statistically. However, depiction of individual estimation results will depend on discrepancy tendencies. If tendencies of estimation discrepancies are generally similar for all measured quantities, only a representative selection of results will be conveyed in the results chapter (remaining results will be provided in Appendix B).

3.2. Simulations

In this section, the simulated scenarios applied to study the correlation factors are described.

A total of 93 simulations have been conducted. Simulations are performed in 19 series. Each series *mostly* consists of 5 simulations, whereas one of these is the *base* simulation. The base simulation is applied to estimate the output of the other simulations in the series, by use of the correlation factors (solving eq. 3.7 and 3.11 for the individual correlation factors). The estimations are further compared to the actual simulations, to assess estimation precision. For every *individual simulation* in each series, only fuel parameters are altered (see Table 3.1). Between every simulation *series*, parameters for Model geometry, HRR, fuel and soot transport are altered. These parameters are likely to affect the solutions to the transport equations of FDS and may therefore yield different estimation discrepancies.

To identify the parameters used for the individual simulations, simulations are referred to by indexes. For instance, the simulation applying Model geometry A (A), a fast-growing fire (F), 100% wood as fuel (10) and soot transported separately as an aerosol (S) with deposition mechanisms activated (Y), is indexed A.F.10.S.Y. The varying input parameters, and associated indexes, are described in Table 3.1.

Table 3.1 Description of varying input variables in FDS simulations.

Parameter	Indexes (separated by dots (.))	Description
Model geometry	A. B.	Two model geometries are used, denoted as A and B. Due to computational cost, most simulations are conducted using the smallest Model, Model A. See section 3.2.3 and 3.2.4 for Model geometry A and B respectively.
HRR	M. F. C1. C1,5. C2. C3. C5. C7.	Time evolving fires are indexed with letters only, herein Medium (M) and Fast (F). Simulations with Constant (C) HRRs are supplemented with numbers. The numbers represent HRR in [MW]. See section 3.2.2 for choice of HRR.
Fuel	0. 3. 5. 7. 10. 5-a. 5-b. 5-c. 5-d. GM23. GM27. GM29. GM31. GM37.	Numbers only, are used when the fuel is a mixture of wood (red oak) and polyurethane (GM25). The numbers indicate the percentage of wood (10 refers to 100%). For some simulations, only soot yield is altered. These are indexed by the number 5, supplemented with a lower-case letter. Otherwise, the polyurethane GM-type is used as index. See section 3.2.7 for fuel properties.
Soot transport	L. SY. SN.	Soot is either transported as part of the Lumped (L) product species or Separately (S) as an aerosol. For the latter, FDS facilitate soot deposition mechanisms. Most such simulations are performed with soot deposition enabled (Y), and a few disabled (N). See section 3.2.6 for soot transport.

Additional information:

- All simulations employ the LES turbulence model. This is the default turbulence model of FDS and is generally more suitable for engineering applications than, for instance, DNS [14].
- Simulation duration, or simulation time, is determined by HRR. The following durations are applied:
    - Growing HRRs: 200 s. The duration is chosen to investigate estimation precision in relatively early phases of the fire, and when flow patterns are continuously evolving.
    - Constant HRRs: 600 s. The duration is chosen to investigate estimation precision in somewhat late phases of the design fire, when flow conditions are rather stable and somewhat near steady state.
- Unless otherwise specified, default properties and settings of FDS v6.7.0 are applied.
- Representative input files used for the simulations are provided in Appendix C.

3.2.1. Choice of simulation code

As to the selection of the CFD code for fire simulations, there are a variety of alternative codes to FDS. One method of choosing the appropriate code, is by comparing validation data. The code best able to predict the outcome of the scenario, may be deemed best suited for the case. In a recent verification and validation study by US NUREG (United States Nuclear Regulatory Commission) [21], FDS was shown to predict far-field species concentrations within experimental uncertainty. According to [22] FDS can predict such quantities with relatively high precision, especially for well-ventilated fires. For this reason, FDS is assumed well suited for the purpose of this study.

FDS is also chosen due to applicability and availability. FDS is a free open source code, with its first official release in 2000. Elements of the code was, however, in use for two decades prior to its release, in other CFD codes and in research. Since its release in 2000 it has been subject to major updates to increase its functionality and flexibility. Today FDS is well established in the fire safety engineering community and have numerous users, including engineers, forensics and scientists [22]. As its user group may be relatively large, the relevance of this study may increase accordingly.

All simulations are performed applying FDS v6.7.0 (latest release at the beginning of this study, fall 2018). NIST's documentation for verification and validation for FDS is based on the framework set by *Standard Guide for Evaluating the Predictive Capability of Deterministic Fire Models*, ASTM E1355-12 (American Society for Testing and Materials) [16]. Most parts of the FDS input files are generated via the third-party application Pyrosim v2018.2.0730. This is a commercial software developed by Thunderhead Engineering for graphical pre-processing of FDS input files. It also allows for implementation of many simulation parameters applied in FDS [23].

3.2.2. Heat release rates

In this study, values of HRR are predetermined. In FDS, HRR is asserted through specification of heat release rate per unit area (HRRPUA), which subsequently is assigned to a VENT. The VENT releases fuel at a rate necessary to sustain the specified HRR, a method physically analogous to a burner [17].

As different values of HRR will transport mass, momentum and energy differently, several HRR values are applied for testing the validity of the correlation factors. HRR values are chosen based on typical values used in Fire Safety Design. Additionally, the interval value of HRR among simulation series are constant in each simulation Model. This due to facilitate better comparison of alterations in estimation discrepancies due to revised HRR among simulation series. Three different constant values of HRR are used for every Model geometry, described in the following.

In the Swedish fire safety code, *Boverkets ändring av verkets allmänna råd (2011:27) om analytisk dimensionering av byggnaders brandskydd* [24], a suggested minimum of 2000 kW may be applied for buildings where active fire suppression systems are installed (if suppression is activated, lower values may be permitted). This value is chosen as a maximum constant HRR for the smallest Model geometry (Model A). Intervals of 500 kW are used, rendering the following HRRs: 1000, 1500 and 2000 kW.

In [24], a value of 5000 kW is suggested for, among others, offices, schools, hotels and apartments. This value is chosen as a mid-value for the largest Model geometry (Model B). Intervals of 2000 kW are used, rendering the following HRRs: 3000, 5000, 7000 kW.

In Fire Safety Design, it is also common to include time evolving HRRs. In this study, this is represented by αt^2-fires (eq. 2.8). In [24] medium- and fast-growing fires for are suggested for, among others, offices, schools, hotels, public buildings and apartments. As such, these growth rates are applied. The medium- and fast-growing fires are defined as 0,012 kW/s^2 and 0,047 kW/s^2 respectively (see table 2.1).

As to the choice of HRRPUA, different values may transfer heat differently to surroundings. Larger HRRPUAs signify smaller surface area of the flame, possibly yielding slower heat distribution to surroundings (due to smaller surface area of the flame) [25]. As such, similar values for all simulations using constant HRRs is desirable. The values are also chosen based on compatibility with the fire Froude number (eq. 2.20) and flame height (eq. 2.21) relative to ceiling height. As to the former, accidental fires typically ascertain a value of unity [19]. Regarding the latter, reduced flame impingement on the ceiling is preferred, as this may affect the solution to the combustion model. Based on the calculations provided in Appendix A.2, a HRRPUA of approximately 1000 kW/m^2 is chosen for the simulations. The values of HRRPUA are slightly adjusted as the VENTs needs to conform with the underlying grid (see Table 3.2).

FDS facilitate HRR-growth by radially spreading fires and time RAMPs of HRRPUA (ramping up the HRRPUA as a function of time for a VENT with constant area). The values of the fire Froude number and flame height are also used for determining the method of emulating HRR-growth. Based on the calculations in Appendix A.2, the best suited approach is chosen to be the radially spreading fire. This due to the method leading to a fire Froude number closer to unity and limited flame impingement on the ceiling. The radial velocity is calculated as such [25]:

$$v_f = \sqrt{\frac{\alpha}{\pi \dot{Q}''}} \tag{3.13}$$

where $\dot{Q}''$ is the HRRPUA. Table 3.2 gives a summary of the HRRs applied, along with corresponding representative simulation indexes. In addition, the spread rates and applied areas of the fire VENTs are shown.

Table 3.2 HRR parameters applied

Description of HRR	Predetermined HRR	Spread rate or VENT area	HRRPUA	Representing index
Medium growing	0,012 kW/s^2	0,0019 m/s	1000 kW/m^2	M
Fast growing	0,047 kW/s^2	0,0039 m/s	1000 kW/m^2	F
Constant	1000 kW	1,0 m^2	1000 kW/m^2	C1
Constant	1500 kW	1,44 m^2	1041,7 kW/m^2	C1,5
Constant	2000 kW	1,96 m^2	1020,4 kW/m^2	C2
Constant	3000 kW	2,89 m^2	1038,1 kW/m^2	C3
Constant	5000 kW	4,84 m^2	1033,1 kW/m^2	C5
Constant	7000 kW	6,76 m^2	1035,5 kW/m^2	C7

The simulated values of HRR were also checked (from the FDS DUMP files) post simulation, to ensure that the predetermined value was attained.

3.2.3. Model A and location of measurement

Model A, with dimensions, is illustrated in Figure 3.1. The fire-room, where the VENT of which the fire originates (red surface), is located to the right. The VENT is located in the center of the room. The VENT is also elevated 0,5 m above the floor. The orientation may allow for more efficient air entrainment to the combustion zone, compared to a placement in, for instance, a corner and/or interfacing the floor.

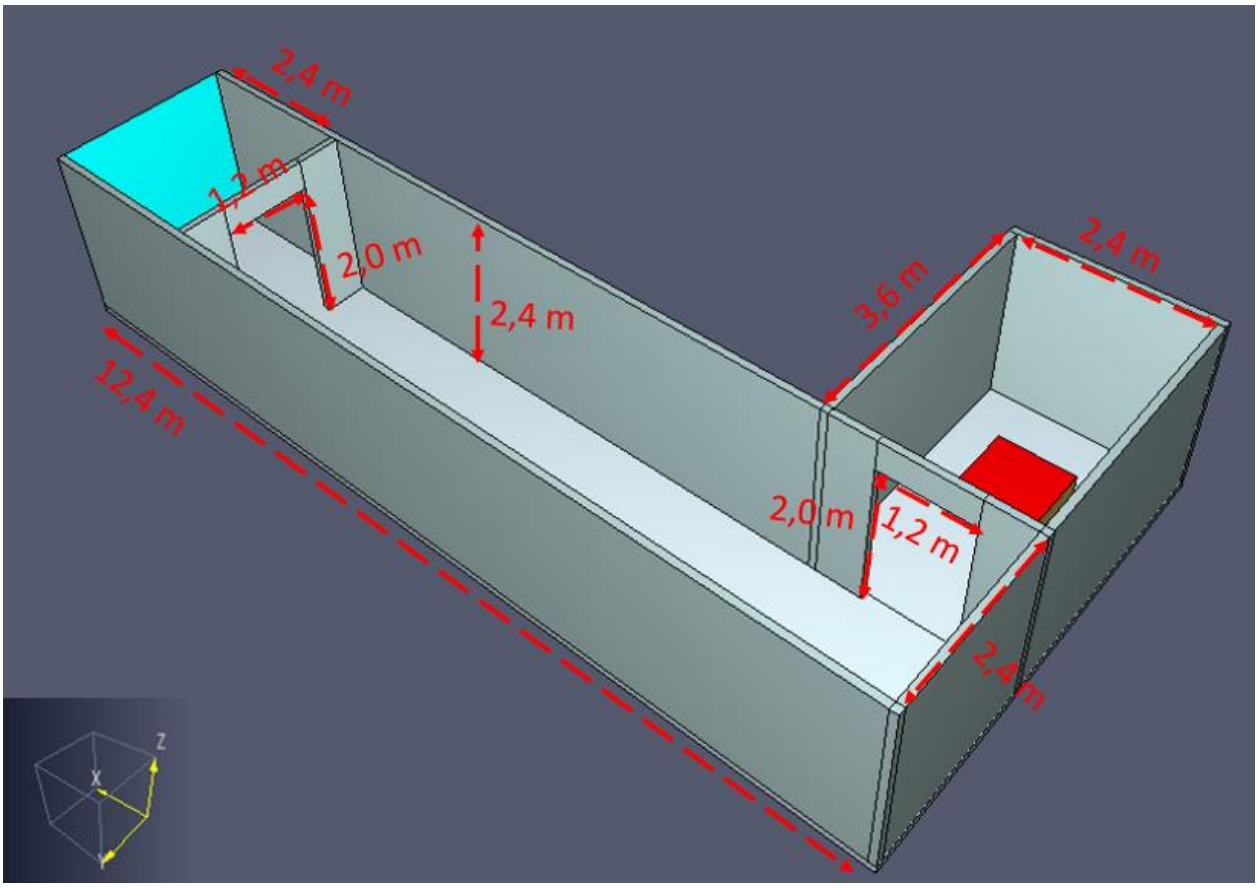

Figure 3.1 Illustration of Model A, with dimensions. Ceiling omitted from model for illustration purposes. Snapshot in Pyrosim.

The Model is based on a variation of the ISO 9705 Room Corner Test. This is a geometry used for classifying building materials. During the classification test, a burner is placed in the corner of the room, exposing the surface of the building materials to heat. Just outside the opening of the room, a hood of 3,0 m^2 is placed for collecting smoke. A variation of the Room *Corner* Test is the Room *Corridor* Test. This variation is scaled down 50%, compared to the Room Corner Test, and is connected to a corridor [26].

The configuration of Model A (Figure 3.1), resembles the Room Corridor Test but with scales closer to the Room Corner Test. The larger scale allows for a larger value of HRR, as well as represents a configuration more applicable to real enclosures.

In Table 3.3 the dimensions of the ISO Test configurations and Model A are shown for comparison. Opening dimensions of Model A are approximately the same as for the Room Corner Test, but with a slightly increased width (by 50%). The corridor dimensions are also somewhat more increased than 100%, compared to the Room Corridor Test. This to allow for more air supply, sustaining a greater HRR.

Table 3.3 Comparison of dimensions of ISO Test rooms and Model A

Geometrical configuration	Dimensions fire room (length-width-height) [m]	Corridor dimensions (length-width-height) [m]	Openings (width- height) [m]
ISO 9705 Room Corner Test	2,4 - 3,6 - 2,4	-	0,8 - 2,0
Variation of Room Corner test: Room Corridor Test	1,2 - 1,8 - 1,2	6 - 0,6 - 1,2	0,3 - 1,2
Model A	2,4 - 3,6 - 2,4	12,4 - 2,4 - 2,4	1,2 - 2,0

In Figure 3.2, the location of measurements, with dimensions, are illustrated. The statistical volumetric mean and maximum soot densities and CO mass fractions will be measured over this volume. The distance from the corridor floor to the bottom of the measurement-volume is 1,5 m. The orientation is chosen as it covers both typical detector locations (ceiling) and typical person heights (approximately 1,5 m when slightly crouching and 1,8 m when standing upright).

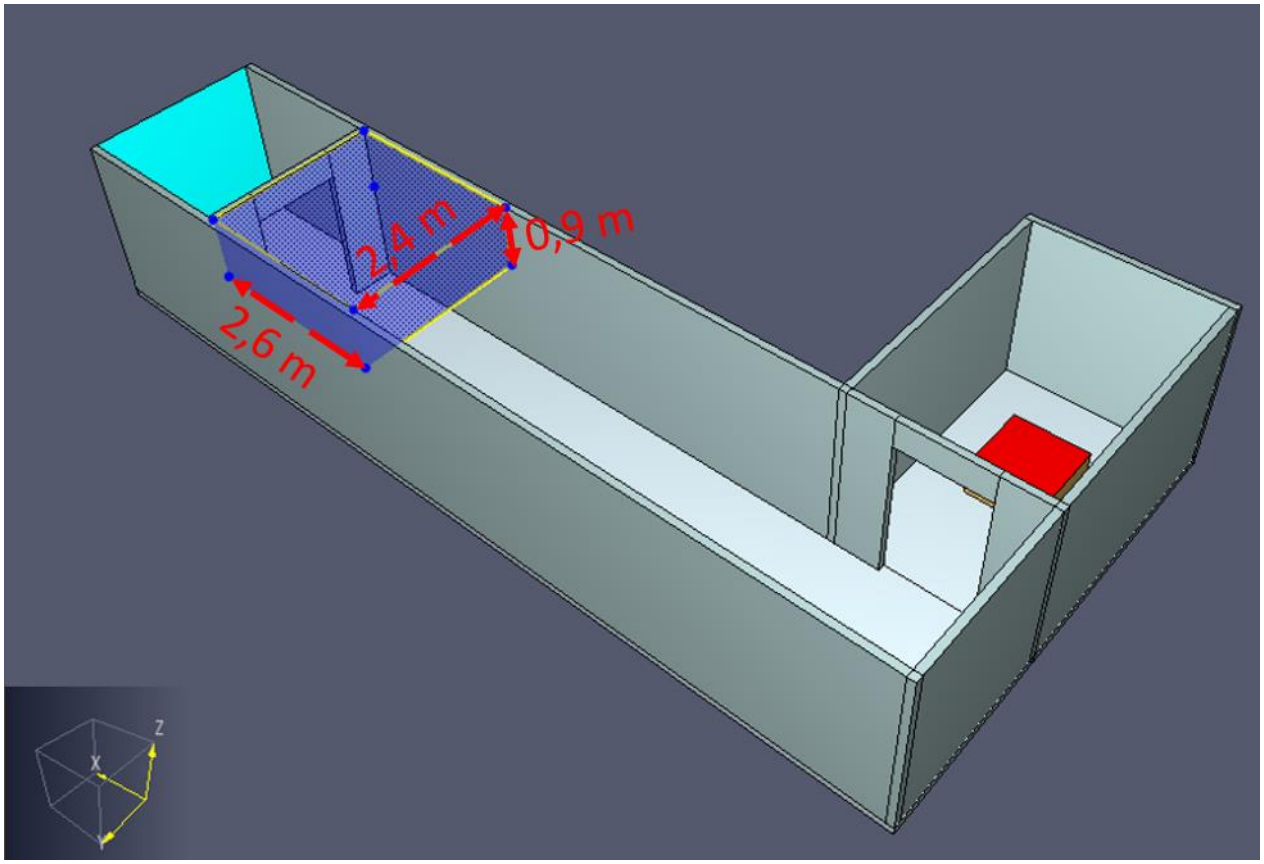

Figure 3.2 Illustration of location of measurements in Model A (blue cube with yellow outlines), with dimensions. Snapshot in Pyrosim.

3.2.4. Model B and locations of measurement

Model B, with dimensions, is illustrated in Figure 3.3. Model B has some of the same trades as Model A but scaled up in size (approximately 6 times in volume). This to investigate the precision of the correlation factors when HRR is scaled up, and when the distance from the fire-origin and position of measurement increases.

The placement of the fire VENT is located in the middle the fire-room, elevated 0,5 m above the floor (similar to Model A). The corridor is also identical to the one in Model A. The fire-room is, however, no longer connected to the corridor directly, but via an intermediate room. Additionally, oxygen is also supplied to the fire-room from an opening in its rear end. All other openings have dimensions similar to Model A, with height and width of 2,0 and 1,2 m respectively.

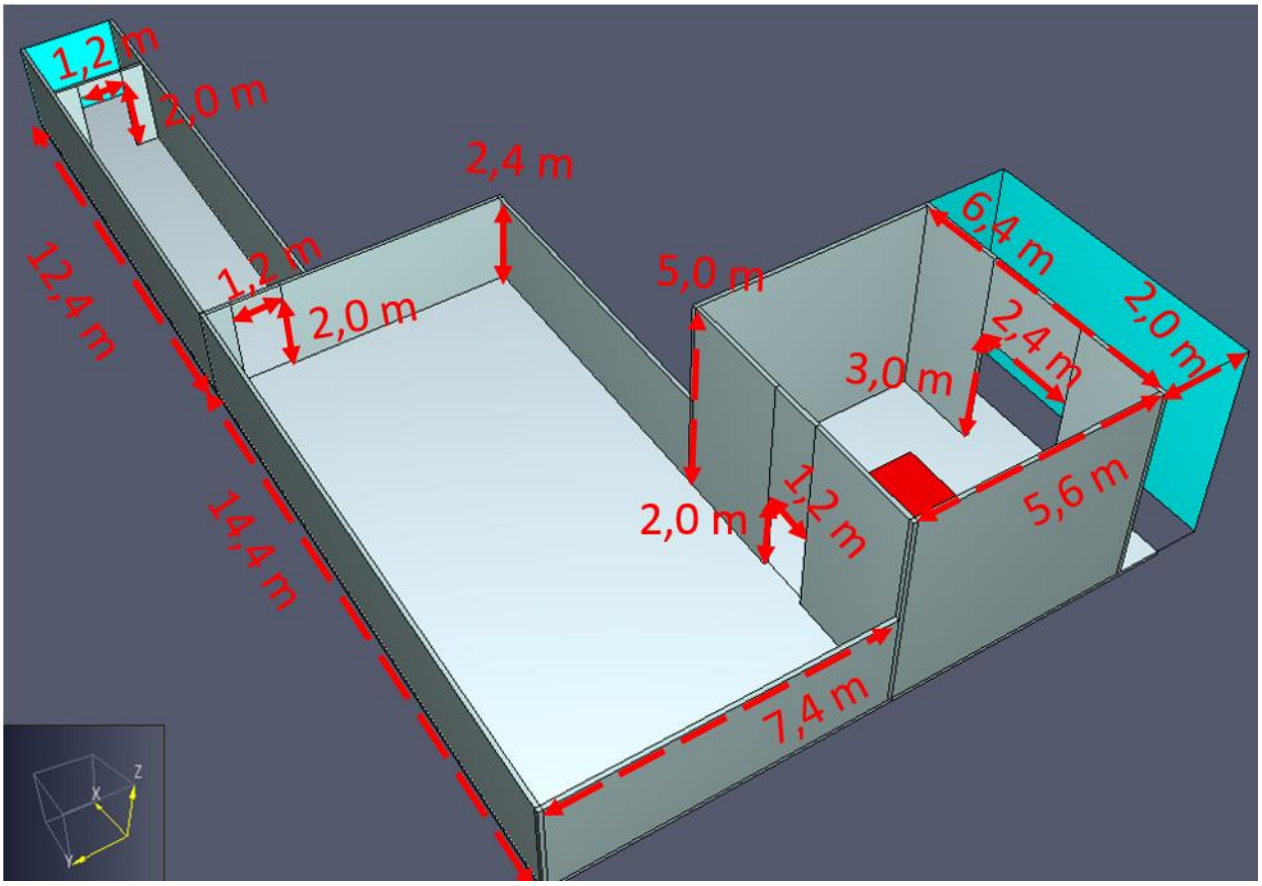

Figure 3.3 Illustration of Model B, with dimensions. Ceiling omitted from model for illustration purposes. Snapshot in Pyrosim.

For Model B, two positions of measurement are applied. This to test differences in estimation accuracy due to distance from fire-origin. The distance between measurement I and II is 19,2 m in the x-direction. The volumes of which measurements are made, are identical to the ones applied for Model A. Locations of measurements are shown in Figure 3.4. The statistical volumetric mean and maximum soot densities and CO mass fractions will be measured over these volumes.

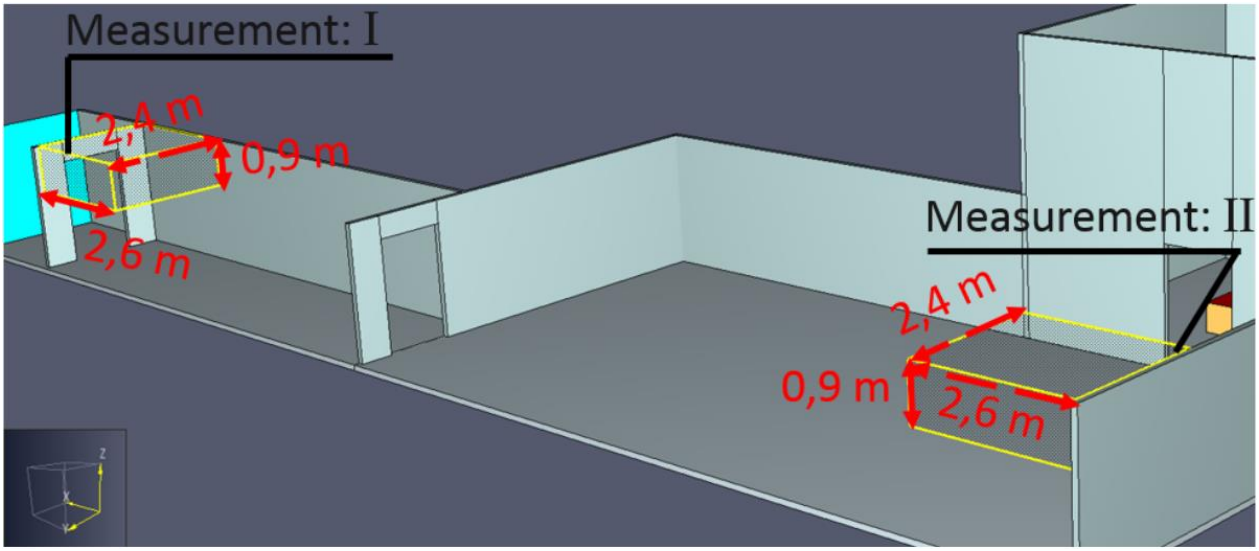

Figure 3.4 Illustration of locations of measurements in Model B (yellow outlines), with dimensions. Wall and ceiling omitted for illustration purposes. Snapshot in Pyrosim.

3.2.5. Boundaries

The term "boundaries" encompass the interfaces between the flow and surroundings, herein walls, ceilings, floors and "outside". The latter refers to outside of the computational domain, and simply entails an interfacing volume with ambient conditions (unless specified otherwise). In FDS, these openings are referred to as OPEN. In the figures describing the Models, for instance Figure 3.3, OPEN boundaries are shown as blue surfaces. As FDS uses a constant pressure assumption at OPEN boundaries, these boundaries should be placed well away from the fire plume. Otherwise, this assumption may cause unrealistic effects to the fire plume [27].

The roofs, floors and walls are assigned properties consistent with 60-minute fire resistance rating (EU-classification: EI 60). These boundaries exchange heat with the flow. The properties are chosen based on relevance to Fire Safety Design. The material properties are specified on the MATL line. The composition of the walls on the SURF line. Walls of the enclosure are constructed as illustrated in Figure 3.5.

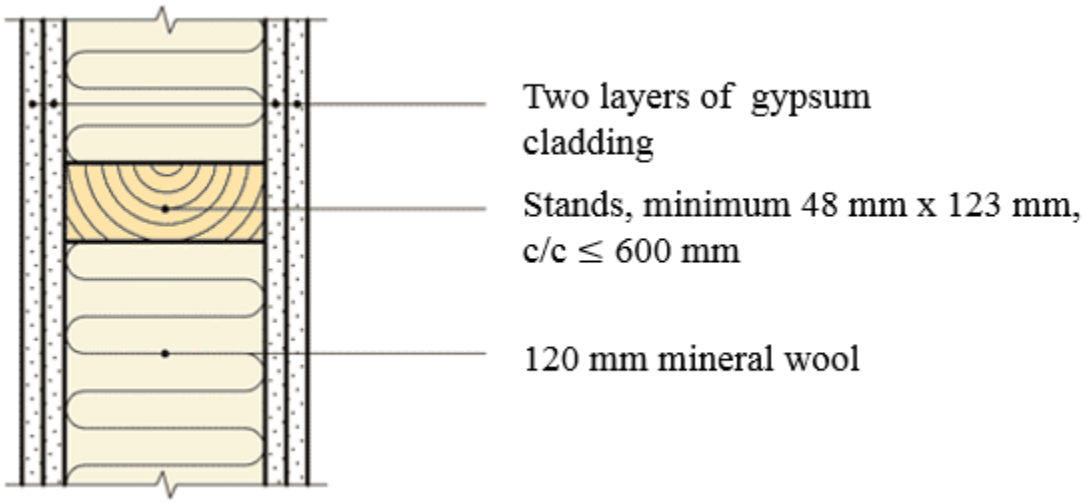

Figure 3.5 Conceptual construction of walls. From [28]

The ceilings of the enclosures are constructed as illustrated in Figure 3.6.

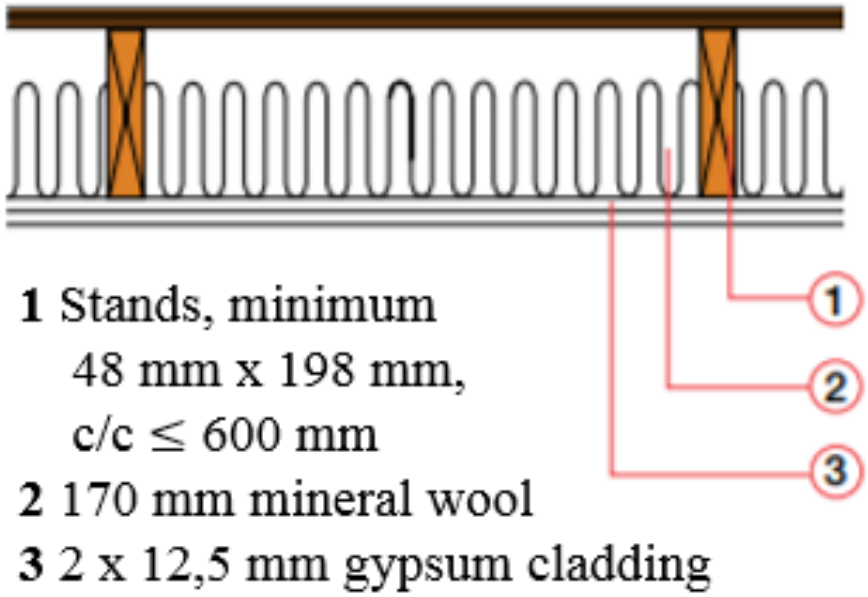

Figure 3.6 Conceptual construction of ceiling. From [29]

Floors of the enclosure are 0,2 m thick concrete slabs. Due to the distance between the floor and the smoke layer, heat transfer will likely be negligible. Thus, thermal properties of the floor will have rather small effects on the solutions to the transport equations.

In Table 3.4, the properties of the physical boundaries are addressed. The thermal properties are collected from [9]. As the stands may be 0,552 m apart (600 mm center to center), these are omitted from the simulation inputs. This simplification is made due to negligible contribution to the heat transfer between the flow and the boundaries.

Table 3.4 Properties of materials used in boundaries. Collected from [9].

Boundary	Material	Layer thickness [m]	k $[W/mK]$	c $[kJ/kgK]$	ρ $[kg/m^3]$
Floor	Concrete	0,2	1,8	1,04	2280
Part of wall	Gypsum cladding	0,0125	0,17	1,09	930
Part of wall	Mineral wool	0,12	0,041	0,8	100
Ceiling	Mineral wool	0,17	0,041	0,8	100

All material boundaries have a void as backing. This signifies that the back side is exposed to a volume with ambient conditions [17]. In FDS, this is specified on the SURF line as BACKING='VOID'.

3.2.6. Soot transport and deposition

Three different methods of treatment of soot are applied. In this study, the default combustion and transport model in FDS is used most frequently. This method implies that all primitive species are transported as part of the lumped species and are treated as gases [17]. Simulations indexed L, applies this transport method.

In some simulations, soot is transported separately as an aerosol with the possibilities of depositing onto surfaces. As the correlation factors do not account for the effects of deposition, it is expected that such mechanisms will influence the estimation precision. Simulations indexed S.Y, applies this transport method.

Additionally, a few simulations are performed where soot is transported separately as an aerosol with deposition mechanisms disabled. These simulations are conducted due to the possible influences of added thermophoretic and gravitational velocities to the convective term in the mass transport equation (2.36) [16]. Simulations indexed S.N, applies this transport method.

In Appendix C, a selection of representative input text files is provided. In Appendix C.1, the method of asserting aerosol transport and soot deposition is shown. In Appendix C.2, the method applied when all species are transported as part of the lumped species is shown.

3.2.7. Fuel properties

The fuel properties presented in this section are used as the input to the functions, $f(I)$, of the correlation factors (eq. 3.6 and 3.10). The calculated values of the correlation factors are provided in Table 4.1.

Fuel properties are chosen to reflect combustible materials often used in Fire Safety Design. Propositions of fuel and reaction data to be examined in Fire Safety Design may be found in several codes, standards and guides. Often, the propositions involve polymers, wood or mixtures of these. In this study, fuel properties are collected from the Appendix in the *SFPE Handbook of Fire Protection Engineering, Fifth Edition* [30]. Use of the Handbook is advantageous in that information as to the conditions of which the fuel data was collected, supplement the fuel properties described (this is often lacking in codes and standards). This offers the advantage of evaluating limits of applicability of the properties in question.

In this study, fuel properties of wood and polymers are used. To represent the former, red oak is applied, a widely used constituent in furniture, flooring and interior finishing [31]. To represent polymers, both rigid

and flexible polyurethane in the GM-series, are applied. These polymers are used in furniture, mattresses, beds, couches and chairs. Fuel properties directly collected from [30] are representing GM23, GM25, GM27, GM29, GM31, GM 39 and red oak. The yields for CO and soot are for well-ventilated fires. The chemical formulas are deduced from measurements in the FM Global Research Flammability Laboratory [30].

Between individual simulations in every simulation series, only fuel properties are altered. For most simulation series, fuel properties are altered in accordance with the surrogate fuel method, eq. 2.40. The surrogate fuels consist of mixtures of GM25 and red oak. The percentile distributions, F, of red oak are 0, 30, 50, 70 and 100 %. The use of surrogate-fuels is advantageous in that all fuel parameters change linearly.

For two simulation series, the fuel consist of a 50/50 mixture of red oak and GM25. This variation only alters the soot yield between individual simulations. The alterations are $\pm 10\%$ and $\pm 20\%$ of the soot yield of the original 0,105 g/g of the 50% surrogate-fuel mixture (see Table 3.5). This fuel parameter variation is included as the soot yield may be especially important in terms of thermal radiative heat transport.

In one simulation series, individual simulations apply fuel parameters representing polyurethane in the GM-series. This fuel parameter variation is included as the fuel properties alter non-linearly, as opposed to the surrogate-fuel variation.

In Table 3.5, fuel properties applied in this study are presented, with representing simulation indexes. Fuel parameters indexed 5 (**bold font**) is used as input to the base simulations in every simulation series, by which all other simulation outputs are estimated.

Table 3.5 Fuel properties and representing indexes. Fuel properties are collected and adapted from [30].

F [%] and/or fuel type	Formula	γ_{CO} $[g/g]$	γ_S $[g/g]$	$\Delta H_{C,ox}$ $[kJ/g_{ox}]$	ΔH_C $[kJ/g_f]$	Representing index
0	$CH_{1,7}O_{0,32}N_{0,07}$	0,028	0,194	12,0	18,0	0
30	$CH_{1,7}O_{0,44}N_{0,05}$	0,021	0,140	12,4	17,4	3
50	$\boldsymbol{CH_{1,7}O_{0,52}N_{0,04}}$	**0,016**	**0,105**	**12,6**	**17,1**	**5**
70	$CH_{1,7}O_{0,60}N_{0,02}$	0,011	0,069	12,8	17,1	7
100	$CH_{1,7}O_{0,72}N_{0,001}$	0,004	0,015	13,2	17,2	10
50	$CH_{1,7}O_{0,52}N_{0,04}$	0,016	0,0840	12,6	-	5-a
50	$CH_{1,7}O_{0,52}N_{0,04}$	0,016	0,0945	12,6	-	5-b
50	$CH_{1,7}O_{0,52}N_{0,04}$	0,016	0,1155	12,6	-	5-c
50	$CH_{1,7}O_{0,52}N_{0,04}$	0,016	0,1260	12,6	-	5-d
GM's						
Polyurethane (flexible) foams						
GM 23	$CH_{1,8}O_{0,35}N_{0,06}$	0,031	0,227	13,7	-	GM23
GM 27	$CH_{1,7}O_{0,3}N_{0,08}$	0,042	0,198	11,2	-	GM27
Polyurethane (rigid) foams						
GM 29	$CH_{1,1}O_{0,23}N_{0,10}$	0,310	0,130	12,6	-	GM29
GM 31	$CH_{1,2}O_{0,22}N_{0,10}$	0,038	0,125	11,9	-	GM31
GM 37	$CH_{1,2}O_{0,20}N_{0,08}$	0,024	0,104	12,7	-	GM37

In Table 3.5, for the surrogate-fuel variation (indexed 0 to 10), ΔH_C is presented in addition to $\Delta H_{C,ox}$. The reason being that the surrogate-fuel variation is also used when soot is transported as an aerosol. When this approach is taken, FDS requires that the heat of combustion is expressed in terms of heat of combustion per unit mass of fuel consumed [17]. ΔH_C is calculated by combining eq. 2.5 and 2.6.

3.2.8. Simulation series

In Table 3.6 through Table 3.9, all simulations are listed with series numbers and simulation indexes. Tables are divided according to simulation parameters. In each table, simulation series numbers are arranged according to HRR. The base simulation in each series, with fuel parameters indexed 5, is indicated by a **bold font**. The total number of simulation series and simulations are 19 and 93 respectively.

In Table 3.6, the simulations applying Model A and species transport via lumped species are listed.

Table 3.6 Model A, species are transported via lumped species. Simulation series categorized by number, and individual simulations by indexes.

Series no.	Series index	Model	HRR	F [%] or GM's	Soot Transport	Soot deposition active (Yes/No)
1	A.M.0.L	A	Medium growth	0	Lumped	N
	A.M.3.L	A	Medium growth	30	Lumped	N
	A.M.5.L	**A**	**Medium growth**	**50**	**Lumped**	**N**
	A.M.7.L	A	Medium growth	70	Lumped	N
	A.M.10.L	A	Medium growth	100	Lumped	N
2	A.F.0.L	A	Fast growth	0	Lumped	N
	A.F.3.L	A	Fast growth	30	Lumped	N
	A.F.5.L	**A**	**Fast growth**	**50**	**Lumped**	**N**
	A.F.7.L	A	Fast growth	70	Lumped	N
	A.F.10.L	A	Fast growth	100	Lumped	N
3	A.C1.0.L	A	1000 kW	0	Lumped	N
	A.C1.3.L	A	1000 kW	30	Lumped	N
	A.C1.5.L	**A**	**1000 kW**	**50**	**Lumped**	**N**
	A.C1.7.L	A	1000 kW	70	Lumped	N
	A.C1.10.L	A	1000 kW	100	Lumped	N
4	A.C1,5.0.L	A	1500 kW	0	Lumped	N
	A.C1,5.3.L	A	1500 kW	30	Lumped	N
	A.C1,5.5.L	**A**	**1500 kW**	**50**	**Lumped**	**N**
	A.C1,5.7.L	A	1500 kW	70	Lumped	N
	A.C1,5.10.L	A	1500 kW	100	Lumped	N
5	A.C2.0.L	A	2000 kW	0	Lumped	N
	A.C2.3.L	A	2000 kW	30	Lumped	N
	A.C2.5.L	**A**	**2000 kW**	**50**	**Lumped**	**N**
	A.C2.7.L	A	2000 kW	70	Lumped	N
	A.C2.10.L	A	2000 kW	100	Lumped	N

In Table 3.7, the simulations applying Model A and soot transported separately as an aerosol are listed. All remaining species are transported as constituents of lumped species.

Table 3.7 Model A, soot transported as aerosol. Simulation series categorized by number, and individual simulations by indexes.

Series no.	Series index	Model	HRR	*F* [%] or GM's	Soot Transport	Soot deposition active (Yes/No)
6	A.M.0.S.N	A	Medium growth	0	Aerosol	N
	A.M.3.S.N	A	Medium growth	30	Aerosol	N
	A.M.5.S.N	**A**	**Medium growth**	**50**	**Aerosol**	**N**
	A.M.7.S.N	A	Medium growth	70	Aerosol	N
	A.M.10.S.N	A	Medium growth	100	Aerosol	N
7	A.M.0.S.Y	A	Medium growth	0	Aerosol	Y
	A.M.3.S.Y	A	Medium growth	30	Aerosol	Y
	A.M.5.S.Y	**A**	**Medium growth**	**50**	**Aerosol**	**Y**
	A.M.7.S.Y	A	Medium growth	70	Aerosol	Y
	A.M.10.S.Y	A	Medium growth	100	Aerosol	Y
8	A.F.0.S.N	A	Fast growth	0	Aerosol	N
	A.F.3.S.N	A	Fast growth	30	Aerosol	N
	A.F.5.S.N	**A**	**Fast growth**	**50**	**Aerosol**	**N**
	A.F.7.S.N	A	Fast growth	70	Aerosol	N
	A.F.10.S.N	A	Fast growth	100	Aerosol	N
9	A.F.0.S.Y	A	Fast growth	0	Aerosol	Y
	A.F.3.S.Y	A	Fast growth	30	Aerosol	Y
	A.F.5.S.Y	**A**	**Fast growth**	**50**	**Aerosol**	**Y**
	A.F.7.S.Y	A	Fast growth	70	Aerosol	Y
	A.F.10.S.Y	A	Fast growth	100	Aerosol	Y
10	A.C1.0.S.Y	A	1000 kW	0	Aerosol	Y
	A.C1.3.S.Y	A	1000 kW	30	Aerosol	Y
	A.C1.5.S.Y	**A**	**1000 kW**	**50**	**Aerosol**	**Y**
	A.C1.7.S.Y	A	1000 kW	70	Aerosol	Y
	A.C1.10.S.Y	A	1000 kW	100	Aerosol	Y
11	A.C1,5.0.S.Y	A	1500 kW	0	Aerosol	Y
	A.C1,5.3.S.Y	A	1500 kW	30	Aerosol	Y
	A.C1,5.5.S.Y	**A**	**1500 kW**	**50**	**Aerosol**	**Y**
	A.C1,5.7.S.Y	A	1500 kW	70	Aerosol	Y
	A.C1,5.10.S.Y	A	1500 kW	100	Aerosol	Y
12	A.C2.0.S.Y	A	2000 kW	0	Aerosol	Y
	A.C2.3.S.Y	A	2000 kW	30	Aerosol	Y
	A.C2.5.S.Y	**A**	**2000 kW**	**50**	**Aerosol**	**Y**
	A.C2.7.S.Y	A	2000 kW	70	Aerosol	Y
	A.C2.10.S.Y	A	2000 kW	100	Aerosol	Y

In Table 3.8, the simulations applying Model A and miscellaneous fuel types are listed (i.e. not using the surrogate-fuel method). All species are transported as constituents of lumped species. As only soot yield is altered between individual simulations in series 13 and 14, the values of soot yield are provided in Table 3.8 (to the right) for clarity. The simulations applied as bases are the same as for series 1 and 2, for medium- and fast-growing fries respectively (which is why the total number of conducted simulations is 93, not 96).

Table 3.8 Model A, miscellaneous fuel types. Simulation series categorized by number, and individual simulations by indexes.

Series no.	**Series index**	**Model**	**HRR**	***F*** [%] **or GM's**	**Soot Transport**	**Soot deposition active (Yes/No)**	$\boldsymbol{\gamma_S}$ $[\boldsymbol{g/g}]$
	A.M.5-a.L	A	Medium growth	50	Lumped	N	0,0840
	A.M.5-b.L	A	Medium growth	50	Lumped	N	0,0945
13	**A.M.5.L**	**A**	**Medium growth**	**50**	**Lumped**	**N**	**0,105**
	A.M.5-c.L	A	Medium growth	50	Lumped	N	0,1155
	A.M.5-d.L	A	Medium growth	50	Lumped	N	0,1260
	A.F.5-a.L	A	Fast growth	50	Lumped	N	0,0840
	A.F.5-b.L	A	Fast growth	50	Lumped	N	0,0945
14	**A.F.5.L**	**A**	**Fast growth**	**50**	**Lumped**	**N**	**0,105**
	A.F.5-c.L	A	Fast growth	50	Lumped	N	0,1155
	A.F.5-d.L	A	Fast growth	50	Lumped	N	0,1260
	A.F.GM23.L	A	Fast growth	GM23	Lumped	N	0,227
	A.F.GM27.L	A	Fast growth	GM27	Lumped	N	0,198
	A.F.GM29.L	A	Fast growth	GM29	Lumped	N	0,130
15	**A.F.5.L**	**A**	**Fast growth**	**50**	**Lumped**	**N**	**0,105**
	A.F.GM31.L	A	Fast growth	GM31	Lumped	N	0,125
	A.F.GM37.L	A	Fast growth	GM37	Lumped	N	0,104

In Table 3.9, the simulations applying Model B are listed.

Table 3.9 Model B. Simulation series categorized by number, and individual simulations by indexes.

Series no.	Series index	Model	HRR	*F* [%] or GM's	Soot Transport	Soot deposition active (Yes/No)
16	B.C3.0.L	B	3000 kW	0	Lumped	N
	B.C3.3.L	B	3000 kW	30	Lumped	N
	B.C3.5.L	**B**	**3000 kW**	**50**	**Lumped**	**N**
	B.C3.7.L	B	3000 kW	70	Lumped	N
	B.C3.10.L	B	3000 kW	100	Lumped	N
17	B.C5.0.L	B	5000 kW	0	Lumped	N
	B.C5.3.L	B	5000 kW	30	Lumped	N
	B.C5.5.L	**B**	**5000 kW**	**50**	**Lumped**	**N**
	B.C5.7.L	B	5000 kW	70	Lumped	N
	B.C5.10.L	B	5000 kW	100	Lumped	N
18	B.C7.0.L	B	7000 kW	0	Lumped	N
	B.C7.3.L	B	7000 kW	30	Lumped	N
	B.C7.5.L	**B**	**7000 kW**	**50**	**Lumped**	**N**
	B.C7.7.L	B	7000 kW	70	Lumped	N
	B.C7.10.L	B	7000 kW	100	Lumped	N
19	B.C5.0.S.Y	B	5000 kW	0	Aerosol	Y
	B.C5.3.S.Y	B	5000 kW	30	Aerosol	Y
	B.C5.5.S.Y	**B**	**5000 kW**	**50**	**Aerosol**	**Y**
	B.C5.7.S.Y	B	5000 kW	70	Aerosol	Y
	B.C5.10.S.Y	B	5000 kW	100	Aerosol	Y

3.3. Model meshing

Grid sensitivity studies (GSS's) are conducted for both Model geometries to determine the grid cell sizes needed to ascertain cell size-independent solutions. The lowest HRRs results in the lowest values of the characteristic flame diameter (eq. 2.19), and thereby generally require the finest mesh resolutions (see section 2.4.1). As such, the simulation series with the lowest HRR-values, for each of the Model geometries, are subjected to the GSS.

3.3.1. Model A

Figure 3.7 show the mesh configuration applied for Model A. Three grid cell resolutions are applied for the GSS. Yellow outlines indicate interfaces between different meshes.

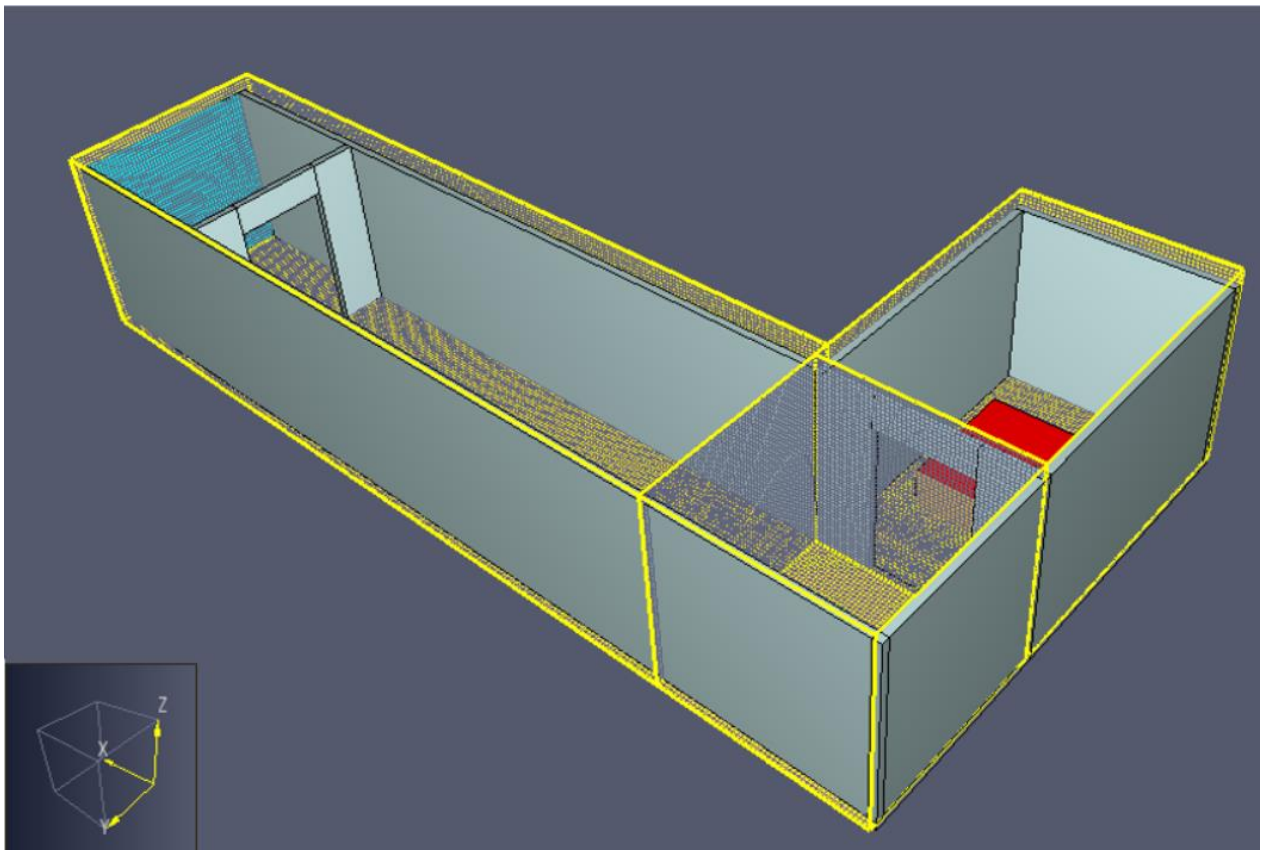

Figure 3.7 Meshing applied for simulation series using Model A. Yellow outlines indicate interfaces between different meshes. Snapshot in Pyrosim.

The mesh resolutions, and number of cells are shown in Table 3.10. Mesh numbers refer to the meshes from left to right in Figure 3.7 (number 3 refer to the fire-room). All mesh-resolutions use a ratio of ½ between grid cell sizes in the fire-room and the corridor.

Table 3.10 Meshing in Model A.

			Resolution 1		Resolution 2		Resolution 3	
Mesh	**Dimensions (x-y-z) [m]**	**Volume [m³]**	**dx [m]**	**Number of grid cells**	**dx [m]**	**Number of grid cells**	**dx [m]**	**Number of grid cells**
1	10,0 – 2,8 - 2,6	72,8	0,2	9100	0,1	72 800	0,05	582 400
2	2,6 - 2,6 - 2,6	17,576	0,2	2197	0,1	17 576	0,05	140 608
3	2,6 - 3,8 - 2,6	25,688	0,01	25 688	0,05	205 504	0,025	1 644 032
Total number of grid cells				**36 985**		**295 880**		**2 367 040**

The simulation series 1, 2 and 3 are subjected to the GSS. The simulations applied are the base simulations in every series, i.e. A.M.5.L, A.F.5.L and A.C1.5.L. Figure 3.8 shows the predicted mean soot densities in the corridor of Model A (see Figure 3.2) from the GSS. The grid cell sizes (dx) refer to the sizes mostly used for the individual mesh resolutions. The difference between the predicted soot densities of the two finest resolutions were approximately 3% on average. This indicates that mesh resolution 2 with dx=0,1 m is sufficiently grid cell size independent. As such, all simulations conducted for Model A use mesh resolution 2.

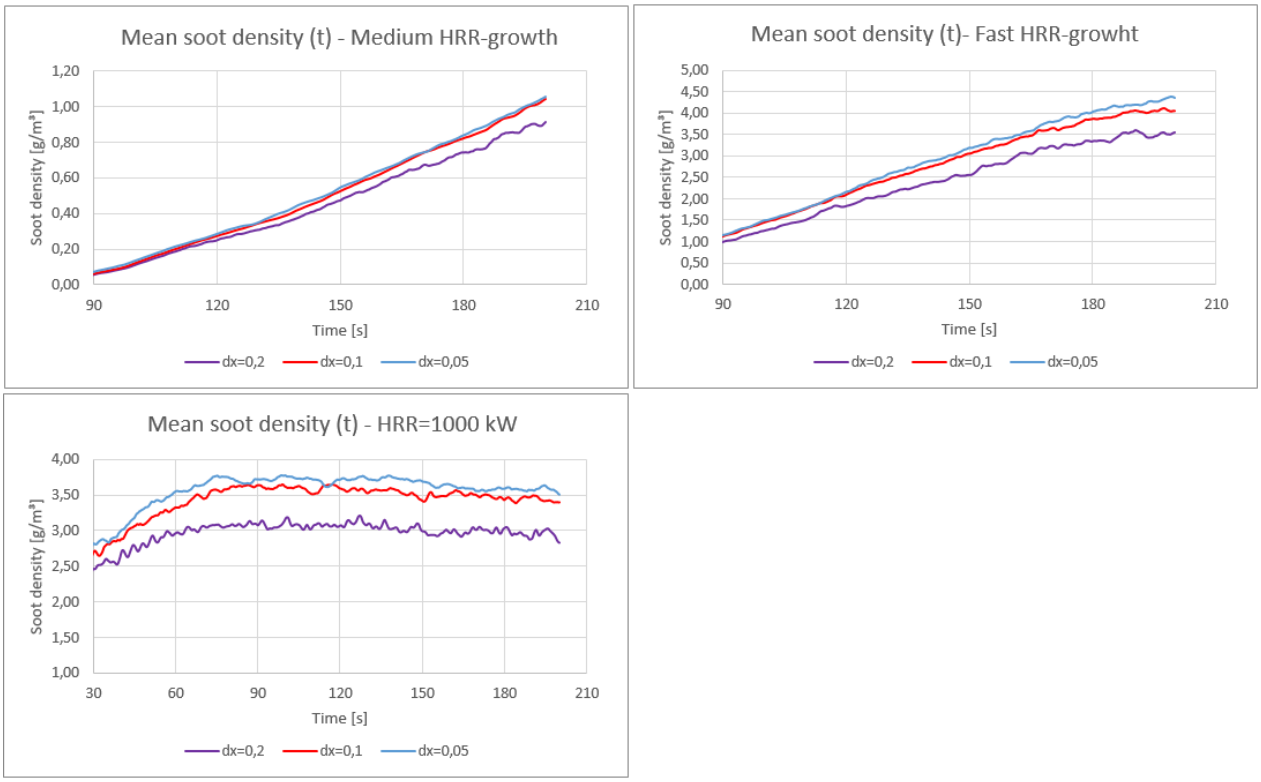

Figure 3.8 Predicted mean soot densities from GSS. Series applied from upper left: 1, 2, 3

The ratios of the characteristic flame diameters, D^*, to the grid cell sizes, dx, used for constant HRRs in Model A are shown in Table 3.11. Grid cell sizes of 0,05 m are used to resolve the fire, while grid cell sizes of 0,1 m resolve most of the Model volume.

Table 3.11 Ratios D^*/dx applied for Model A.

HRR [kW]	Cell size, dx [m]	D*/dx [-] ~
1000	0,1	9,6
1500	0,1	11,3
2000	0,1	12,6
1000	0,05	19,2
1500	0,05	22,6
2000	0,05	25,3

3.3.2. Model B

Three grid cell resolutions are applied for Model B. In Figure 3.9, meshing applied for the finest grid cell resolution for Model B is illustrated. Yellow outlines indicate interface between meshes.

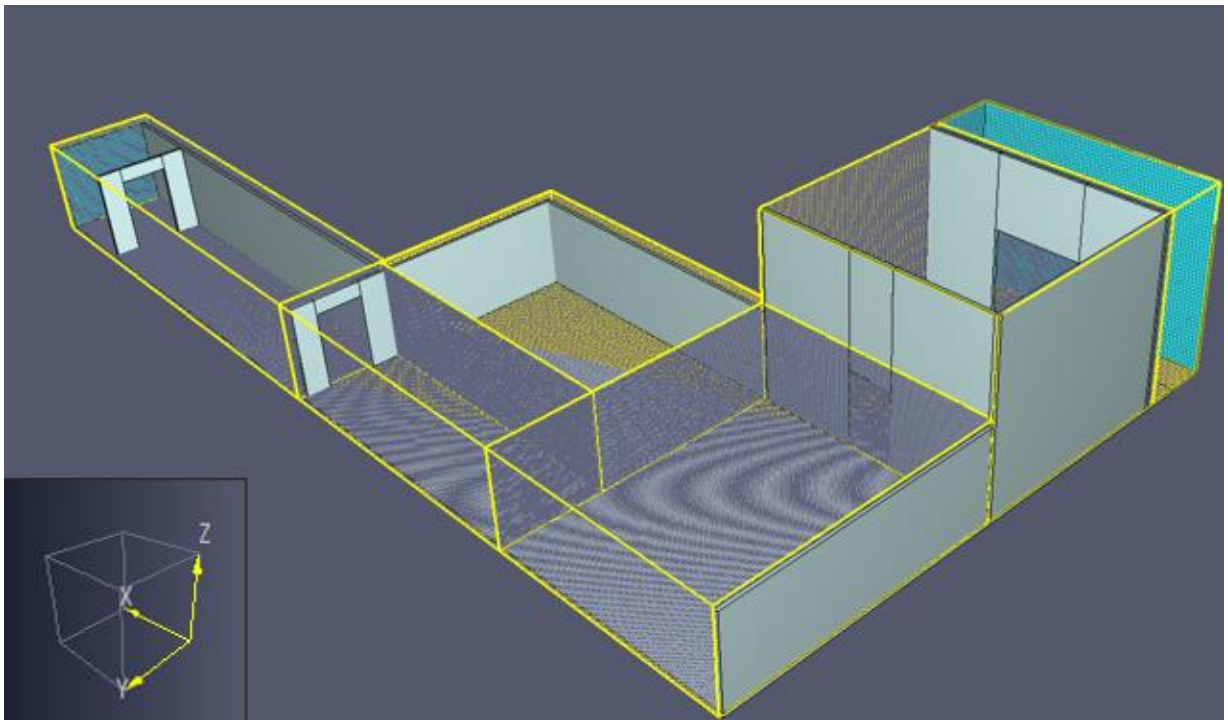

Figure 3.9 Meshing applied for the finest grid cell resolutions for simulation series using Model B. Yellow outlines indicate interface between different meshes. Snapshot in Pyrosim.

In Table 3.12, the mesh resolution with the finest grid cell resolution is described. Most meshes use grid cell sizes of 0,05 m. However, some also apply 0,1 m. This due to computational cost. Using 0,05 m on the entire domain would result in 5 114 720 grid cells, possibly requiring over a month of computational time. Mesh numbers, 1-6, refer to mesh volumes from left to right in Figure 3.9. Where necessary, mesh numbers are supplied with a short description.

Table 3.12 Meshing in Model B- finest grid cell resolution

			Resolution 1	
Mesh	**Dimensions (x-y-z) [m]**	**Volume [m^3]**	**dx [m]**	**Number of grid cells**
1	12,5 - 2,8 - 2,6	91	0,05	728 000
2 (interfacing corridor)	8,0 - 2,7 - 2,6	56,125	0,05	449 000
3	8,0 - 5,1 - 2,6	106,08	0,1	106 080
4	6,6 - 7,6 - 2,6	128,7	0,05	1 029 600
5 (fire-room)	6,6 - 5,6 - 5,0	198	0,05	1 584 000
6 (rear of fire room)	6,6 - 2,2 - 5,0	59,4	0,1	59 400
Total number of grid cells				**3 956 360**

In Figure 3.10, meshing applied for the two coarsest grid cell resolutions for Model B is illustrated. Yellow outlines indicate interface between meshes.

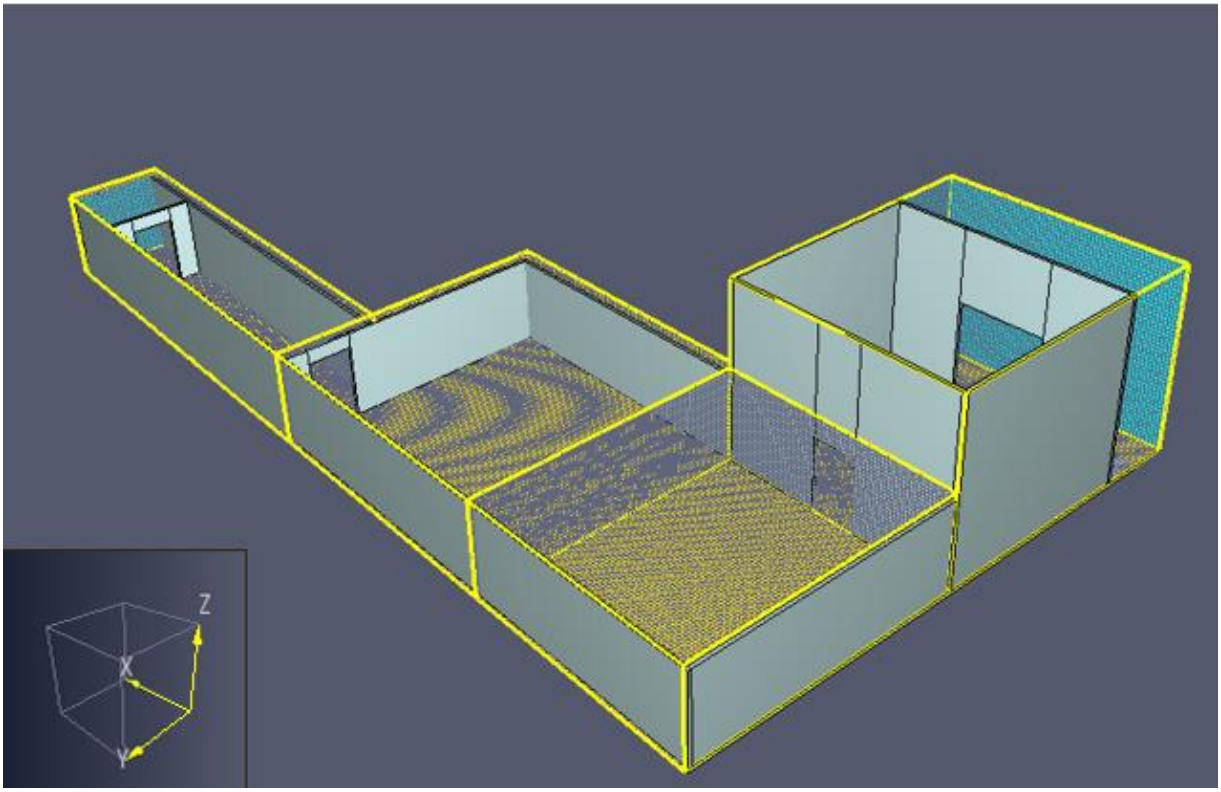

Figure 3.10 Meshing applied for the two coarsest grid cell resolutions for simulation series using Model B. Yellow outlines indicate interface between different meshes. Snapshot in Pyrosim.

In Table 3.13, the mesh resolutions with the two coarsest grid cell resolutions are described. Numbers, 1-4, refer to mesh volumes from left to right in Figure 3.10 (number 4 refer to fire-room).

Table 3.13 Meshing in Model B- two coarsest grid cell resolutions.

			Resolution 2		**Resolution 3**	
Mesh	**Dimensions (x-y-z) [m]**	**Volume [m^3]**	**dx [m]**	**Number of grid cells**	**dx [m]**	**Number of grid cells**
1	12,5 - 2,8 - 2,6	91	0,1	91 000	0,2	45 500
2	8,0 - 7,8 - 2,6	162,24	0,1	162 240	0,2	81 120
3	6,6 - 7,6 - 2,6	128,7	0,1	128 700	0,2	64 350
4	6,6 - 7,8 - 5,0	257,4	0,1	257 400	0,2	128 700
Total number of grid cells				**639 340**		**319 670**

Simulation series 16 and 17 are subjected to the GSS. The simulations applied are the base simulations in every series, i.e. B.C3.5.L and B.C5.5.L. Figure 3.11 shows the predicted mean soot densities in measurement position I in Model B (see Figure 3.4) from the GSS. The grid cell sizes (dx) refer to the sizes mostly used for the individual mesh resolutions. The difference between the predicted soot densities of the two finest resolutions were approximately 4% on average. This indicates that mesh resolution 2 with dx=0,1 m is sufficiently grid cell size independent. As such, all simulations conducted for Model B use mesh resolution 2.

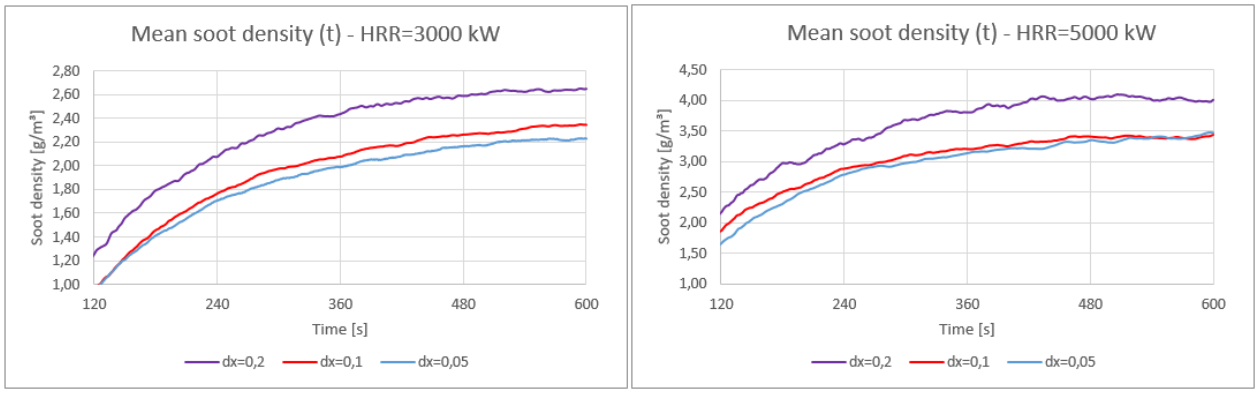

Figure 3.11 Predicted mean soot densities from GSS. Series applied from left: 16, 17.

The ratios of the characteristic flame diameters, D^*, to the grid cell sizes, dx, used for Model B are shown in Table 3.14.

Table 3.14 Ratios D^*/dx applied for Model B.

HRR [kW]	**Cell size, dx [m]**	**D*/dx [-] ~**
3000	0,1	14,9
5000	0,1	18,2
7000	0,1	20,9

3.4. Evaluation of correlation performance

In this section, the equations and procedures for evaluating the performances of the correlation factors are described. The equations are based on solving the correlation factor-equations for the output quantity, θ_a, (eq. 3.7 and 3.11) and applying the fuel parameters provided in Table 3.5. The ratios of the estimated to simulated time history-values, $\frac{\theta_{a,estimated}(t)}{\theta_{a,simulated}(t)}$, indicate the precision of estimation.

3.4.1. Interpreting ratios of estimation to simulation

First, means of interpreting the values of $\frac{\theta_{a,estimated}}{\theta_{a,simulated}}$ needs to be established. As the estimated mass quantity value of simulation output a is in the numerator of the ratio $\frac{\theta_{a,estimated}}{\theta_{a,simulated}}$, values above and below unity indicate over- and underestimations respectively. Figure 3.12 makes further inquiries as to interpretation of potential tendencies of estimation discrepancies. The figure plots exemplified ratios of $\frac{\theta_{a,estimated}}{\theta_{a,simulated}}$ (vertical axis) against exemplified values of correlation factors (horizontal axis). Every point represents one simulation of which estimations and simulations are made (for simulation a). Lines are drawn between the points to convey potential discrepancy tendencies. If under- and overestimations are observed for low and high values of the correlation factors respectively (red line), this indicates that the results of simulations in the series are more *similar* to each other than predicted by the correlation factors. Adversely, if over- and underestimations are observed for low and high values of the correlation factors respectively (blue line), this suggests that the results of simulations in the series are more *dissimilar* to each other than predicted by the correlation factors. Ideally, however, the ratio of $\frac{\theta_{a,estimated}}{\theta_{a,simulated}}$ should be close to unity for all values of the correlation factors (green line), meaning the estimated value is identical to the actual simulated value. The method of displaying correlation discrepancies in the example of Figure 3.12 is also applied in section 4.2 of the results chapter.

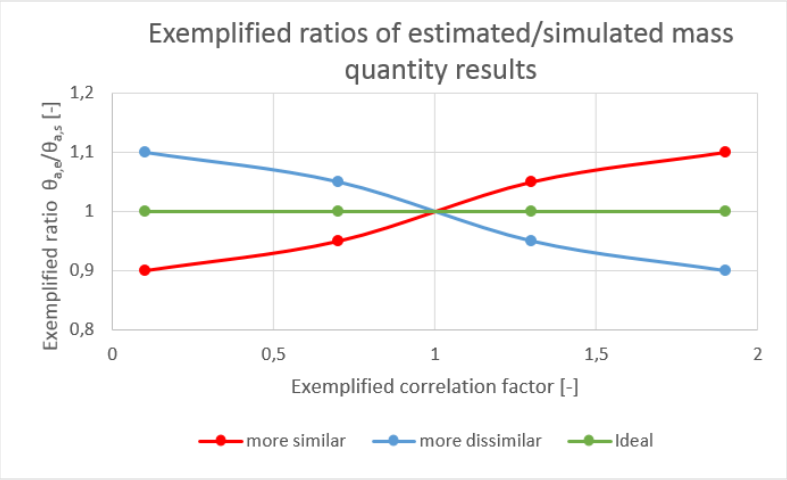

Figure 3.12 Examples of more (red) and less (blue) similarities of mass quantity output between simulations in a series, relative to the indications given by the correlation factors. Green line indicates pristine estimation.

3.4.2. Time averaging

Time averaging for the different series are based on HRR-values, as HRR is somewhat indicative of when stable flow patterns occur. The last 80 to 200 s of the simulation times are applied for time averaging. It must be noted, however, that estimation discrepancies were rather constant, independent on the choice of time averaging-interval. To support this, a few recorded non-averaged time histories of selected estimations and simulations are also shown in the results chapter (section 4.1) and Appendix B.4.

For time averaging, the following time intervals are applied:

- Medium growing fires in Model A: 120 to 200 s.
- Fast growing fires in Model A: 90 to 200 s.
- Constant HRRs in Model A and Model B: 400 to 600 s.

Unless otherwise specified, all results of this study are time averages. For instance, the presented volumetric mean soot densities for $\frac{\theta_{a,estimated}}{\theta_{a,simulated}}$, is the time- and volume averaged value. Only the first plot of section 4.1 and results presented in Appendix B.4 show instant values (time histories).

3.4.3. Trendline ratios

Trendlines are functions showing the prevailing direction and tendency of a dataset. The dataset is linearized, and small fluctuations are ignored. Trendlines, T_θ, for a dataset, $y(x)$, are calculated by [32]:

$$T_\theta(X) = \bar{y} + \frac{\sum_1^n (x_i - \bar{x})(y_i - \bar{y})}{\sum_1^n (x_i - \bar{x})^2}(X - \bar{x}) \tag{3.14}$$

where x_i and y_i are the values of the original dataset for $i = 1, 2, 3 \ldots n$, referring to values of the individual simulations in each series. $\bar{x}$ and $\bar{y}$ are the average values of all x_i and y_i in the dataset. X is the new input variable for the trendline function, T_θ. The subscript θ refers to mass quantity output, such as soot densities (S) and CO mass fractions (CO).

The trendlines are applied as substitutes for evaluating the differences in estimation discrepancy due to estimated mass quantity (soot densities, ρY_S, and CO mass fractions, Y_{CO}). Preferably, the ratios of $\frac{\rho Y_{S,a,estimated}}{\rho Y_{S,a,simulated}}$ to $\frac{Y_{CO,a,estimated}}{Y_{CO,a,simulated}}$ would be evaluated. However, since estimations of soot and CO-quantities apply different correlation factor-values for the same simulation, trendlines are more appropriate. For instance, estimations of the soot densities and CO mass fractions for simulations applying the set of fuel parameters indexed 0 (0% wood and 100% GM25), uses values of correlation factor 1 of 1,753 and 1,661 respectively (see Table 4.1). Using trendlines instead, allows substituting the correlation factor-values with a representable correlation factor-scale. As such, x_i and y_i, of eq. 3.14, represent correlation factor-values and time averaged ratios of estimation to simulation respectively. The values of X used for input to the trendlines are representative to the scope of correlation factor-values, ranging from approximately 0 to 2,0.

In this study, trendlines for soot density, T_s, and CO mass fraction, T_{CO}, are calculated. As both trendlines apply the same substituted correlation factor-variable, X, the ratios of the trendlines, T_s/T_{CO}, can be applied to evaluate potential differences in estimation discrepancy between the two quantities.

3.4.4. Summarizing performances

To summarize the performance of the correlation factors, the number of estimations yielding discrepancies within given percentile intervals are presented in columns and tables. The percentiles are calculated as such:

$$Estimation\ error\ [\%] = \left(1 - \left(\frac{\overline{\theta_{a,estimated}(t)}}{\overline{\theta_{a,simulated}(t)}}\right)\right) \cdot 100\% \tag{3.15}$$

Columns and tables are shown for every form of statistical output and recorded quantity, in section 4.4.

4. Results

This chapter provides and compares the estimated and simulated results. In the first section, estimated values are plotted against simulated values. Section 4.2 presents ratios of estimated to simulated values plotted against values of the correlation factors. For the first two sections, *only* the statistical volumetric mean soot density, ρY_{soot}, values are applied. Maximum soot density values and CO mass fractions are shown in Appendix B. This due to similar tendencies of estimation discrepancy occurring for most recorded output (as described in section 3.1.3). The last two sections convey statistical representations of the performance of the correlation factors. For statistical representation in the two last sections, all recorded output is applied. Section 4.3 use the trendline ratios (eq. 3.14) to investigate the difference in estimation precision due to output quantity (CO mass fraction and soot density). Section 4.4 use percentile discrepancy-values (eq. 3.15) to investigate the overall precision of the estimations conducted.

The position of measurements in the Models are repeated for clarity in Figure 4.1 and Figure 4.2.

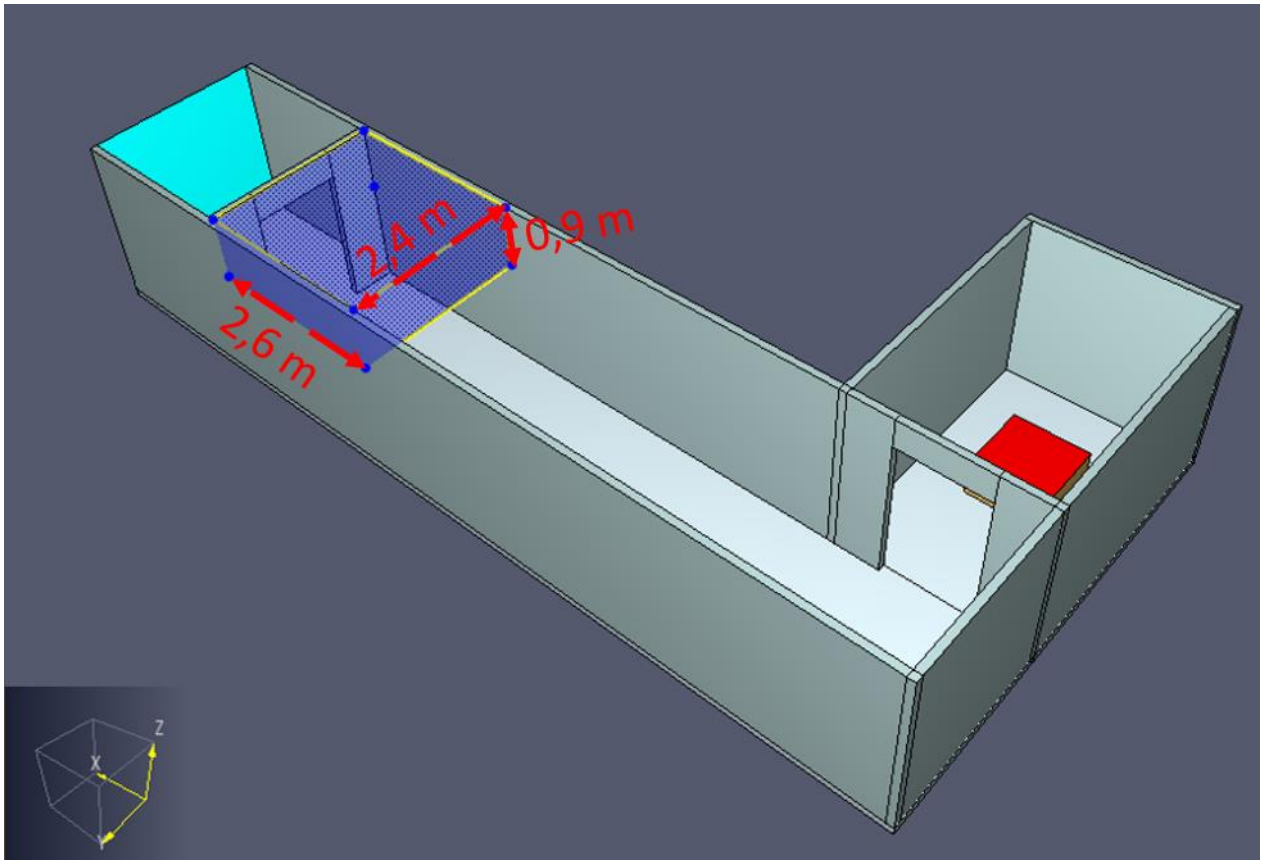

Figure 4.1 Illustration of location of measurements in Model A (blue cube with yellow outlines), with dimensions. Snapshot in Pyrosim.

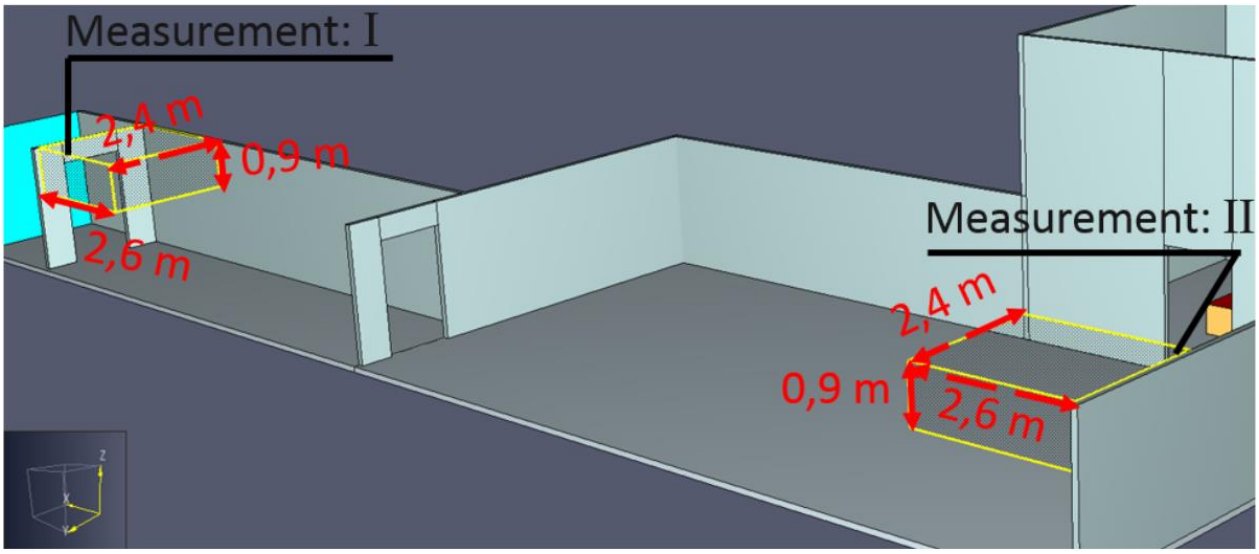

Figure 4.2 Illustration of locations of measurements in Model B (yellow outlines), with dimensions. Wall and ceiling omitted for illustration purposes. Snapshot in Pyrosim.

Table 4.1 show the calculated values for the correlation factors, in the four most right columns. Values are calculated by use of parameters provided in Table 3.5 (repeated in Table 4.1 for clarity), inserted into equation 3.6 and 3.10 for correlation factor 1 and 2 respectively. Simulations indexed 5 (indicated by **bold font**) are applied as base simulations for all estimations in every simulation series.

Table 4.1 Fuel properties, representing indexes and correlation factors. Fuel properties are collected and adapted from [30].

F [%] and/or fuel type	Formula	γ_{CO} $[g/g]$	γ_S $[g/g]$	$\Delta H_{C,ox}$ $[kJ/g_{ox}]$	ΔH_C $[kJ/g_f]$	Representing index	$\beta_{1,S}$	$\beta_{2,S}$	$\beta_{1,CO}$	$\beta_{2,CO}$
0	$CH_{1,7}O_{0,32}N_{0,07}$	0,028	0,194	12,0	18,0	0	1,753	1,693	1,661	1,604
30	$CH_{1,7}O_{0,44}N_{0,05}$	0,021	0,140	12,4	17,4	3	1,311	1,293	1,291	1,273
50	$\boldsymbol{CH_{1,7}O_{0,52}N_{0,04}}$	**0,016**	**0,105**	**12,6**	**17,1**	**5**	**1**	**1**	**1**	**1**
70	$CH_{1,7}O_{0,60}N_{0,02}$	0,011	0,069	12,8	17,1	7	0,656	0,667	0,687	0,698
100	$CH_{1,7}O_{0,72}N_{0,001}$	0,004	0,015	13,2	17,2	10	0,141	0,147	0,247	0,258
50	$CH_{1,7}O_{0,52}N_{0,04}$	0,016	0,0840	12,6	-	5-a	0,768	0,772	0,960	0,965
50	$CH_{1,7}O_{0,52}N_{0,04}$	0,016	0,0945	12,6	-	5-b	0,881	0,884	0,979	0,982
50	$CH_{1,7}O_{0,52}N_{0,04}$	0,016	0,1155	12,6	-	5-c	1,124	1,120	1,021	1,018
50	$CH_{1,7}O_{0,52}N_{0,04}$	0,016	0,1260	12,6	-	5-d	1,252	1,245	1,044	1,037
GM's										
Polyurethane (flexible) foams										
GM 23	$CH_{1,8}O_{0,35}N_{0,06}$	0,031	0,227	13,7	-	GM23	1,953	2,129	1,750	1,908
GM 27	$CH_{1,7}O_{0,3}N_{0,08}$	0,042	0,198	11,2	-	GM27	1,897	1,712	2,640	2,384
Polyurethane (rigid) foams										
GM 29	$CH_{1,1}O_{0,23}N_{0,10}$	0,310	0,130	12,6	-	GM29	1,005	1,034	1,573	1,617
GM 31	$CH_{1,2}O_{0,22}N_{0,10}$	0,038	0,125	11,9	-	GM31	0,983	0,959	1,961	1,913
GM 37	$CH_{1,2}O_{0,20}N_{0,08}$	0,024	0,104	12,7	-	GM37	0,602	0,643	0,911	0,973

4.1. Estimated and simulated soot density values

First in this section, Figure 4.3 presents plots of time histories of estimated (dotted lines) and simulated (solid lines) statistical volumetric mean soot density values. The plots show results from simulation series 16, 17, 18 and 19 using HRRs of 3000, 5000, 7000 and 5000 kW respectevely, applying Model B, and measurement position I (corridor in Figure 4.2). Estimations are made using correlation factor 1 (eq. 3.7) and the base simulation in each series, indexed 5 (black solid lines). All name-references refer to the fuel parameter index used for the simulations (see Table 4.1). The estimated time histories are additionally referred to by the letter "E".

The plots are shown to convey that estimation discrepancies are generally similar throughout the duration of the simulation time (set to 600 s for constant HRRs). Additional time history plots are provided in Appendix B.4, where the tendency is generally the same, i.e. relatively stable estimations independent of simulation duration. As such, time averaged values are deemed suitable to represent the discrepancies between estimation and simulation.

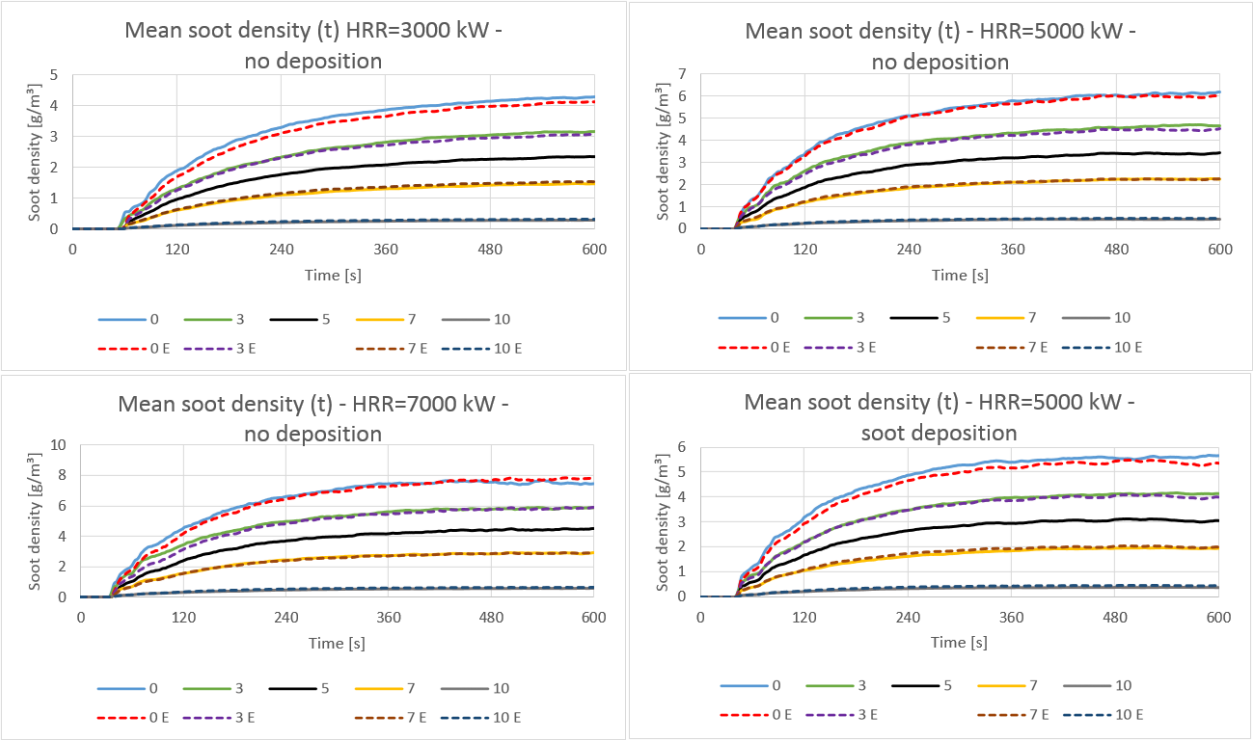

Figure 4.3 Time histories of estimated and simulated values of statistical mean soot density. Recorded values are from Model B, measurement I. Series applied from upper left: 16, 17, 18, 19

In the remaining plots of this section, depicted in Figure 4.4 through Figure 4.7, the time averaged values for the estimated statistical mean soot densities (vertical axis) are plotted against the simulated values (horizontal axis). Estimations are made using correlation factor 2, eq. 3.11 (correlation factors are differentiated in section 4.2). Plots are arranged according to the parameters fuel type, HRR and Model. In all plots, marker-names refer to series number and fuel parameter index. For instance, series 1 and fuel parameter index 0, is referred to by "1.0". All same-coloured markers apply the same simulation series. Different marker-symbols differentiate fuel parameter indexes. Baselines are supplied for indication of estimation discrepancies of 0%, -10% and 10%.

In Figure 4.4, the results for simulations applying Model A, growing HRRs (medium to the left and fast to the right) and the surrogate-fuel method are shown. Red, blue and green markers show time averaged results from simulations applying soot transported as part of lumped species (simulation index L), soot transported as aerosol with no deposition disabled (simulation index S.N), and soot transported as an aerosol with soot deposition enabled (simulation index S.Y), respectively. The plots show that estimated values match the simulated values quite well. Only slight under- and overestimations appear to be present.

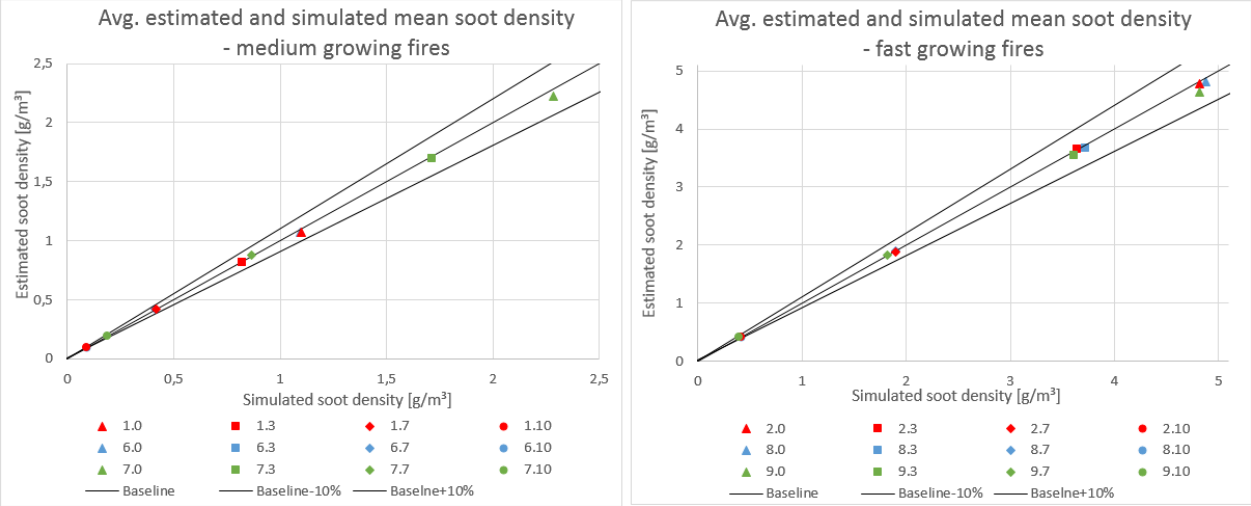

Figure 4.4 Estimated time averages of soot densities plotted against the simulated values. The points include all time evolving HRRs with fuel altering according to the surrogate-fuel method.

In Figure 4.5, the results from simulations applying Model A and constant HRRs are shown. Series applying disabled (soot transported as part of lumped species) and enabled soot deposition are shown in the left and right plot respectively. Red, blue and green markers show time averaged results from simulations applying HHRs of 1000, 1500 and 2000 kW respectively. The figures show less difference in soot density values between blue and green markers than that between red and blue markers, even if the differences in HRRs are the same. The effect is less pronounced when soot deposition is enabled (right plot). Otherwise, estimation discrepancies for all series in Figure 4.5 appear to be low.

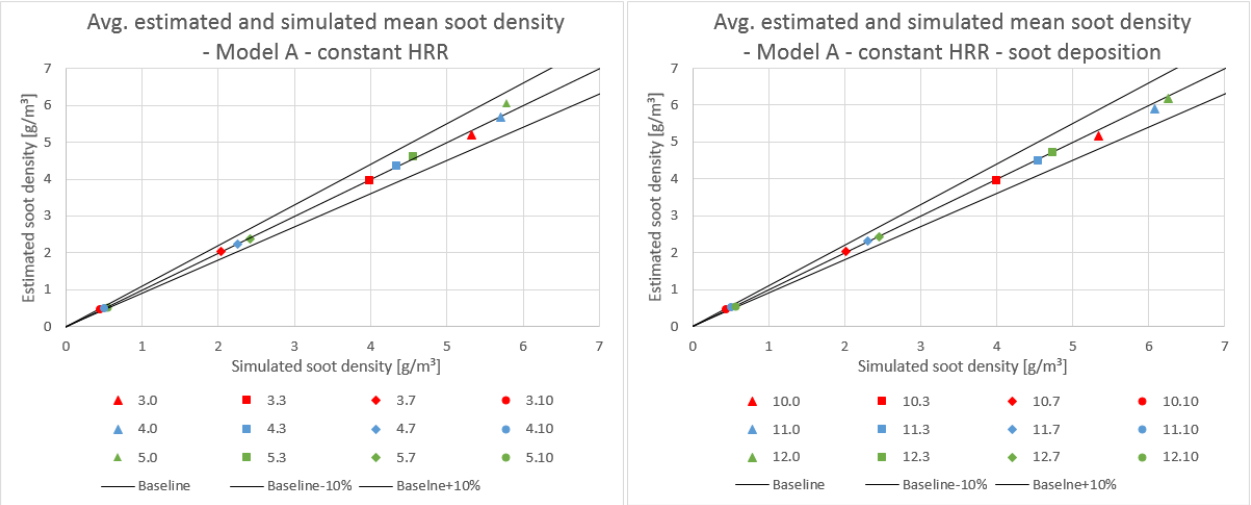

Figure 4.5 Estimated time averages of soot densities plotted against the simulated values. The points include all simulation series with constant HRRs in Model A.

In Figure 4.6, results from all series applying Model B are shown (measurement I to the left and II to the right). Red, blue, green and purple markers show time averaged results from simulations applying HRRs of 3000, 5000, 7000 and 5000 kW respectively. The estimated values appear to be generally similar to the simulated values. However, fuel parameters indexed 0 (threesomes) and 10 (circles) seems to yield some under- and overestimations respectively.

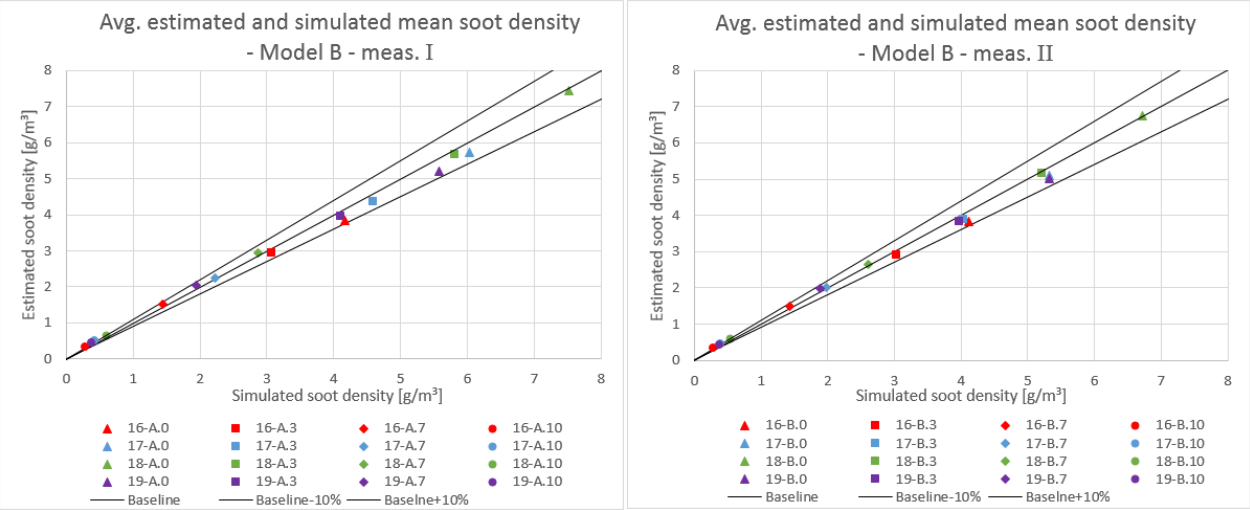

Figure 4.6 Estimated time averages of soot densities plotted against the simulated values. The points include all simulation series in Model B.

In Figure 4.7, the series applying Model A, growing HRRs and miscellaneous fuel types are shown. "Miscellaneous" refer to the fuel variation where only soot yield is varied (series 13 and 14), and the GM-series (series 15). Series 13 apply medium HRR-growth rate. Series 14 and 15 apply fast growth rate. Generally, the estimated and simulated values are rather similar. However, simulations with fuel index GM23 (or just "23", green threesome) seems to yield a somewhat high overestimation (approximately 10%).

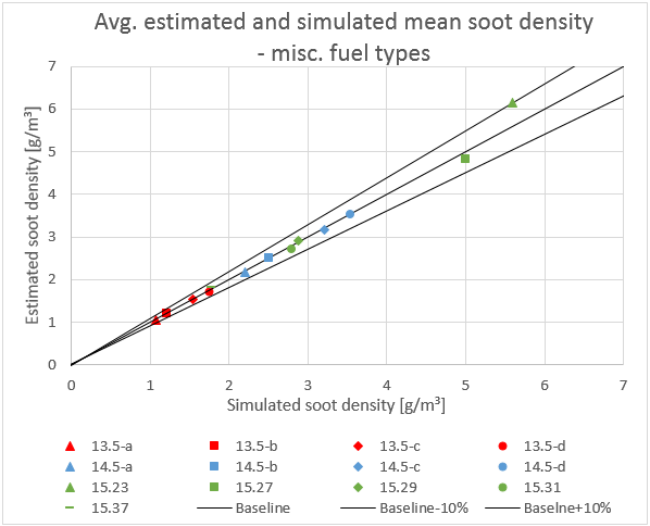

Figure 4.7 Estimated time averages of soot densities plotted against the simulated values. The points include simulation series applying miscellaneous fuel variations.

4.2. Ratios of estimated to simulated values

This section shows the time averaged ratios of the estimated statistical mean soot density values to the simulated values (vertical axis), i.e. the time averaged ratio $\frac{\theta_{a,estimated}}{\theta_{a,simulated}}$. The ratios are plotted against correlation factor values (horizontal axis). The estimated values for correlation factor 1 and 2 are calculated by use of eq. 3.7 and 3.11 respectively. Since the values of the correlation factors used to estimate results of a simulation are rather similar (values are presented in Table 4.1), two markers, representing one fire scenario, will be located closely on the horizontal axis, making individual simulations easily identifiable.

The categorization of the following sub-sections allows for comparing tendencies of discrepancy due to commonalities or peculiarities between fire scenario characteristics. Of particular interest are the tendencies for over- and underestimations for different values of correlation factors. Such tendencies are also referred to as increased similarities or dissimilarities among individual simulations in a series, relative to the predictions made by the correlation factors (as exemplified in section 3.4.1).

4.2.1. Differentiating HRR, Model geometry and position of measurement

Figure 4.8 through Figure 4.11 show plots using the lumped species transport method (for all species, included soot), simulation indexes L. All plots convey results from simulations applying the surrogate-fuel method (fuel indexes 0 to 10). For these series, the values of correlation factors range from approximately 0,14 to 1,7. High values correspond to a low percentage of wood in the surrogate fuel (fuel indexes 0 and 3), and vice versa. In all following plots, increased HRR between simulation series, tends to yield lower and higher ratios of estimation to simulation for low and high values of the correlation factors respectively. This means that the simulation results of individual simulations in a series are increasingly more similar, than predicted by the correlation factors, when HRR increases.

Figure 4.8 show ratios for series applying Model A and growing HRRs (medium to the left and fast to the right). The simulation series applied are 1 (left) and 2 (right). The ratio $\frac{\theta_{a,estimated}}{\theta_{a,simulated}}$ is generally close to unity for all correlation factor-values, for both medium and fast HRR-growth. There is, however, a slight decrease and increase of $\frac{\theta_{a,estimated}}{\theta_{a,simulated}}$ for low and high values of the correlation factors respectively, when HRR is increased (going from the left plot to the right plot).

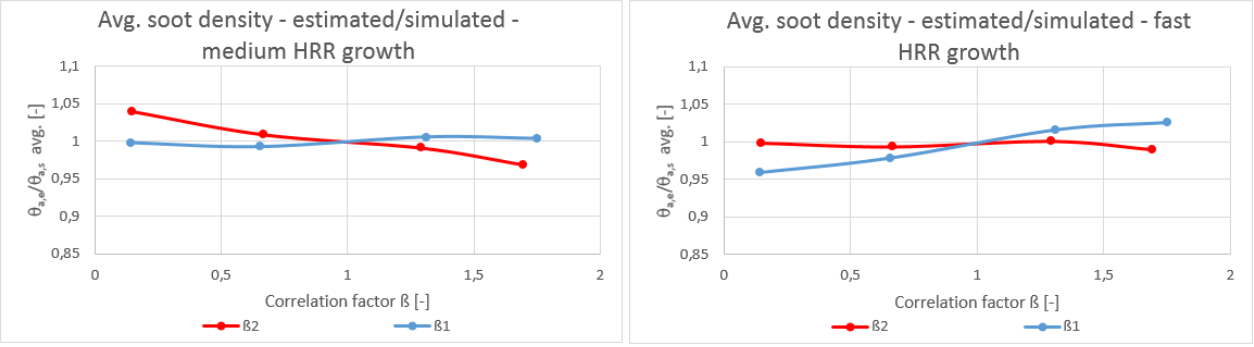

Figure 4.8 Model A, growing HRRs. Simulation series from left: 1, 2.

In Figure 4.9, simulation series applying Model A and constant HRRs are shown. The simulation series from upper left are 3, 4 and 5. The tendency for reduced values of the ratios for low correlation factors (and vice versa), for increased HRR, is especially apparent for these plots. As such, individual simulation results in one simulation series, become more similar, when the HRR of the series increase, compared to the predictions made by the correlation factors. The plots show that the ratios $\frac{\theta_{a,estimated}}{\theta_{a,simulated}}$ are generally closer to unity using correlation factor 2 than 1, except for HRR=1000 and the correlation factor-values above 1,5.

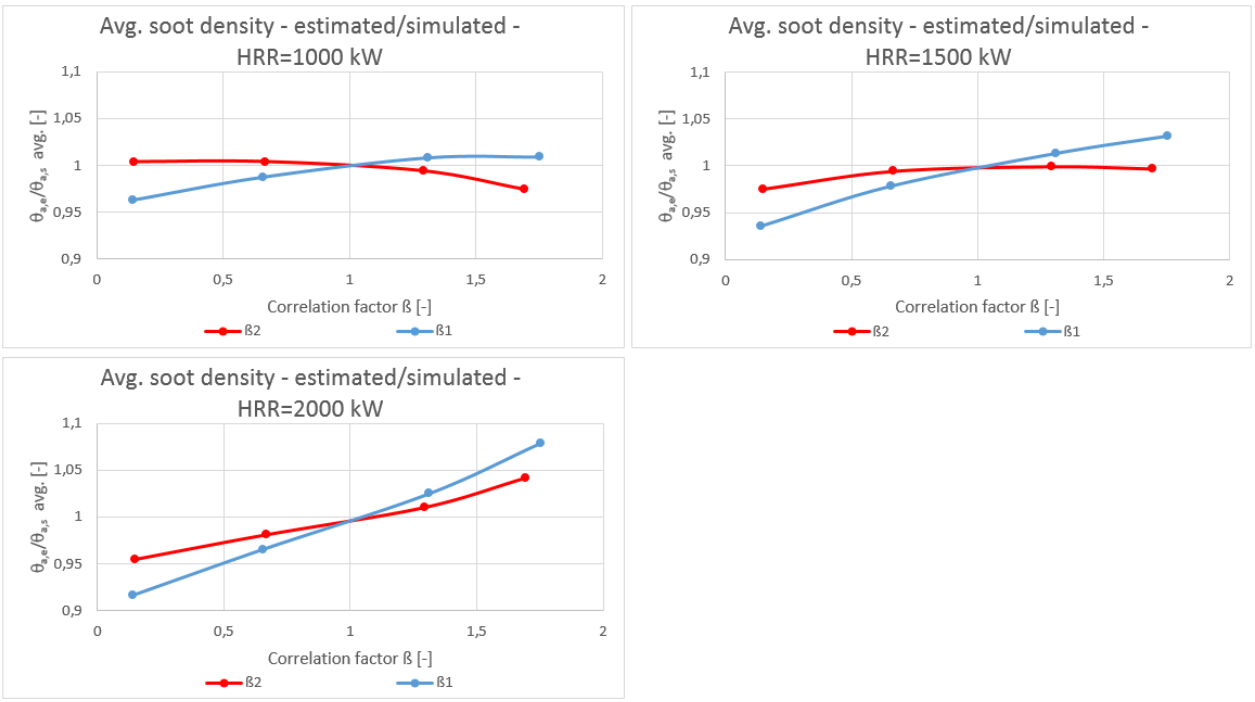

Figure 4.9 Model A, constant HRR. Simulation series from upper left: 3, 4, 5.

In Figure 4.10 (measurement I) and Figure 4.11 (measurement II) simulation series applying Model B are shown. Series used in the figures are 16, 17 and 18, from the upper left plots. Low values of the correlation factors tend to yield a relatively high degree of overestimations. High values of the correlation factors generally tend to yield underestimations, except for HRR=7000 kW. The discrepancies are reduced with increased values of HRR. By comparing measurements I and II, it appears discrepancies increase with increased distance from the fire origin (I is further away than II). In summary, this signify that results of individual simulations in a series becomes increasingly similar, compared to predictions made by the correlation factors, when HRR is increased and/or when the position of measurement is closer to the fire origin.

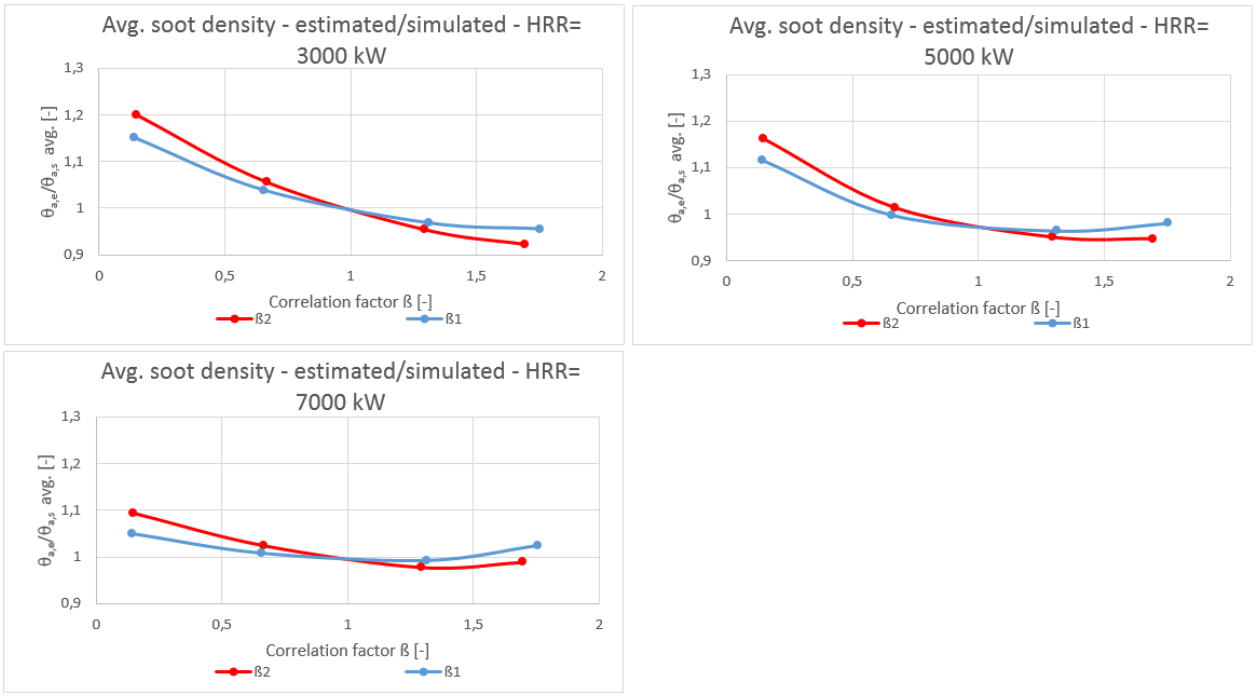

Figure 4.10 Model B, measurement position I. Simulation series and position of measurements from upper left: 16, 17, 18.

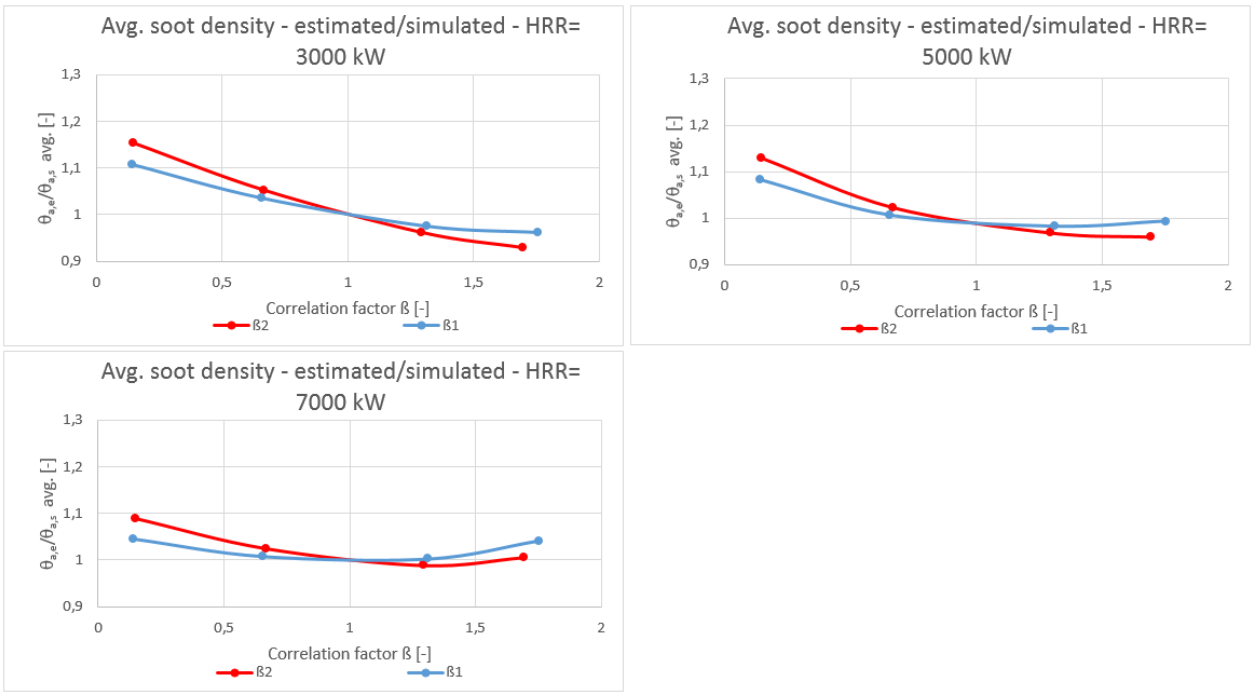

Figure 4.11 Model B, measurement position II. Simulation series and position of measurements from upper left: 16, 17, 18.

4.2.2. Differentiating transport mechanisms and soot deposition

Figure 4.12 through Figure 4.15 compare estimation results from series applying different transport mechanisms for soot and soot deposition. All plots convey results from simulations applying the surrogate-fuel method.

Figure 4.12 show results from series 1, 6 and 7 (from upper left), using medium growing HRRs. In Figure 4.13, results from series 2, 8 and 9 are shown (from upper left), using fast growing HRRs. Both figures show essentially no differences in estimation discrepancies due to species transport and/or deposition. Additionally, values of $\frac{\theta_{a,estimated}}{\theta_{a,simulated}}$ are generally close to unity.

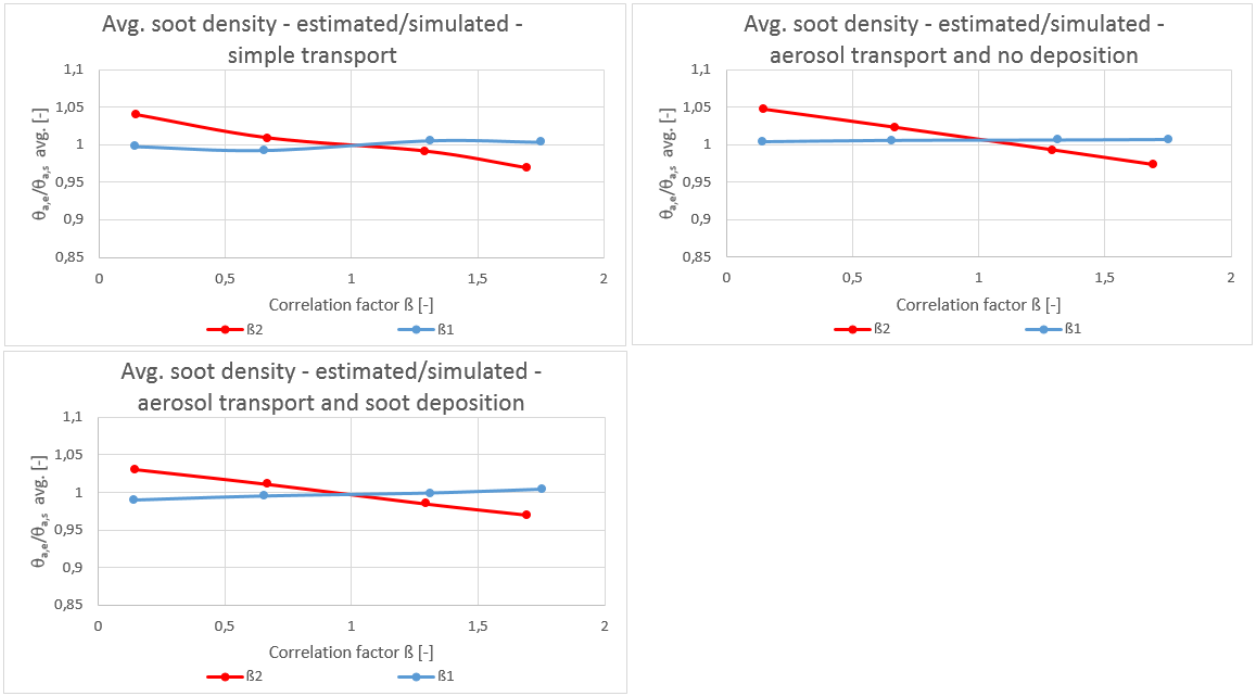

Figure 4.12 Model A, medium HRR growth. Simulation series from upper left: 1, 6, 7.

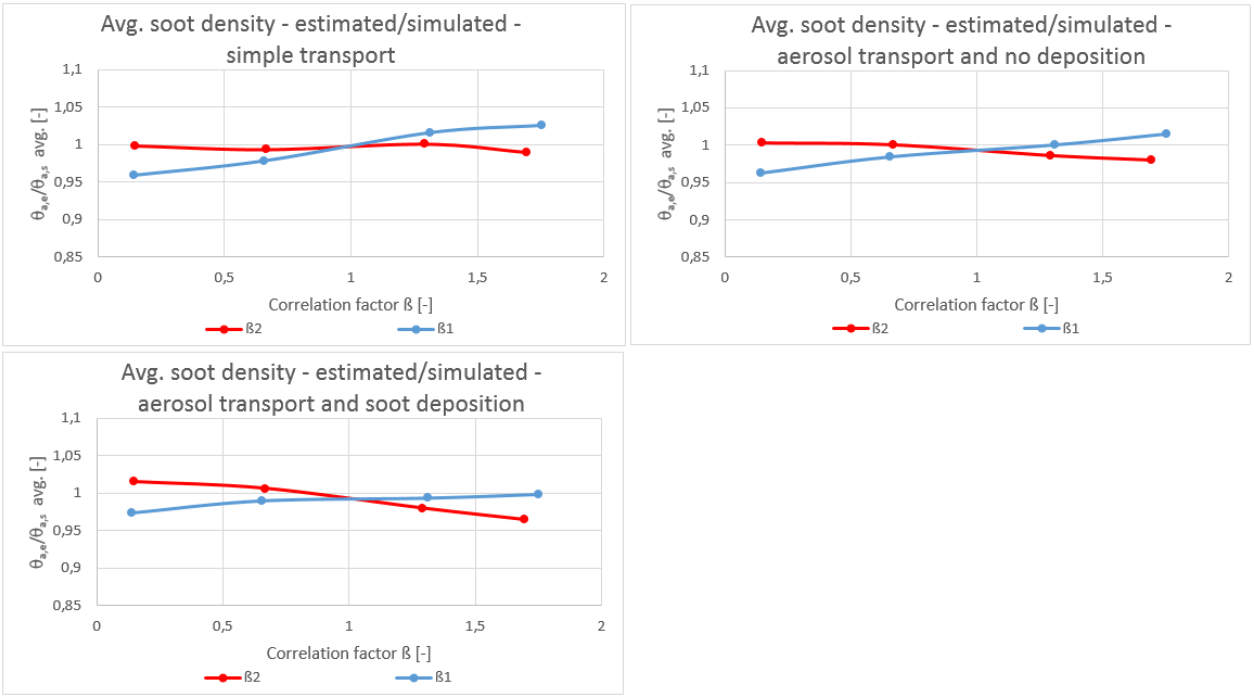

Figure 4.13 Model A, fast HRR growth. Simulation series from upper left: 2, 8, 9.

Figure 4.14 show ratios for the simulation series applying Model A and constant HRRs. In the left column, series 3, 4 and 5 are shown, while in the right column, series 10, 11 and 12 are shown. Increased HRR tends to yield lower and higher ratios for low and high values of the correlation factors respectively. This tendency is less pronounced for series applying active soot deposition (right column). This suggests results of individual simulations in a series are slightly more dissimilar when activating soot deposition.

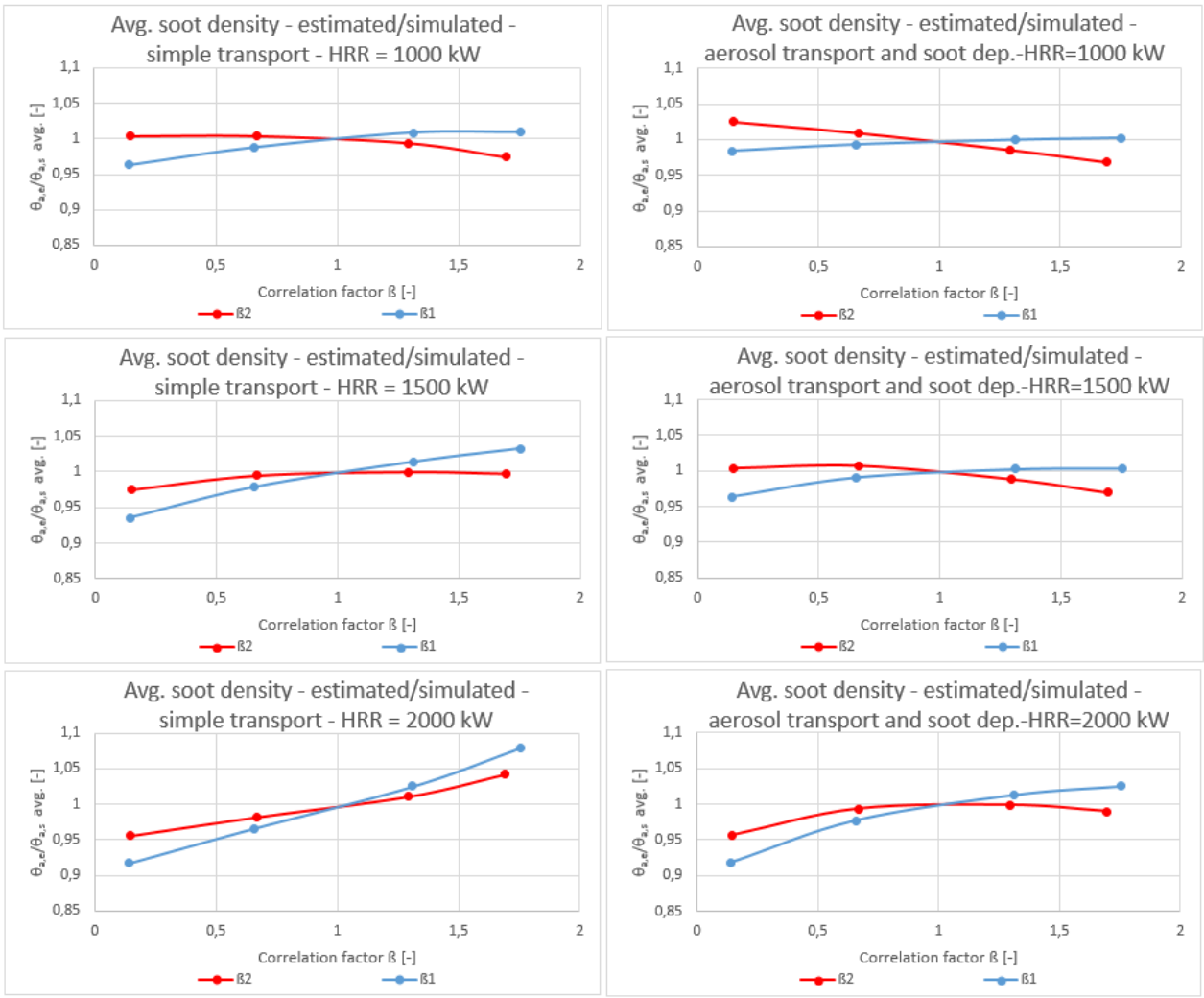

Figure 4.14 Model A, constant HRR. Simulation series from upper left: 3, 10, 4, 11, 5, 12.

Figure 4.15 show ratios for the simulations of Model B, applying HRR of 5000 kW. In the left column, series 17 (no deposition) is used, while in the right column, series 19 (active soot deposition) is applied. Upper and lower row depict results from measurement position I and II respectively. The discrepancies tend to increase when soot deposition mechanisms are active (right column). Similar to Model A, (Figure 4.14), this suggests individual simulation results of a series are more dissimilar when activating soot deposition.

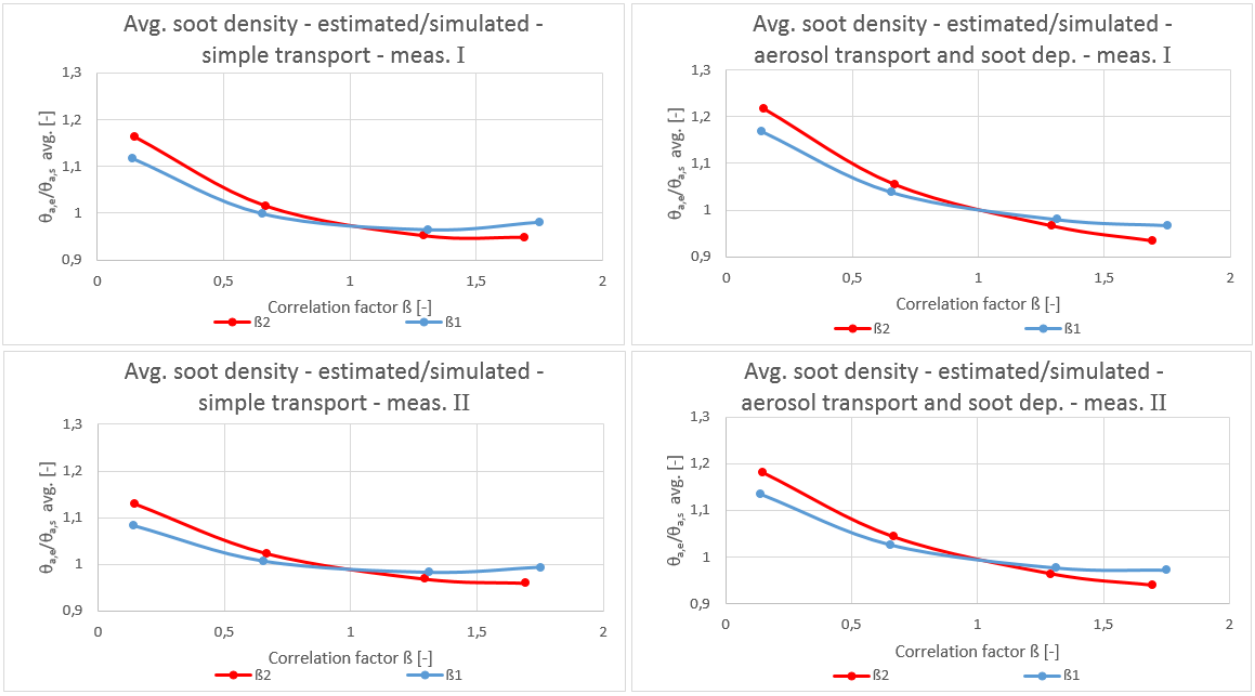

Figure 4.15 Model B. Simulation series and position of measurements from upper left: 17-I, 19-I, 17-II, 19-II.

4.2.3. Differentiating miscellaneous fuel-type variations

Figure 4.16 and Figure 4.17 show results from series applying miscellaneous fuel type-variations compared with the surrogate-fuel variation. For the latter, the horizontal axis (correlation factor-values) are configured for better comparison, meaning the axis are adjusted so that correlation factor-values of different plots are more similar to each other. All simulation series are conducted using Model A and growing HRRs.

Figure 4.16 show the ratios of series 1 and 2 (left column) compared to series 13 and 14 (right column). The former two series apply the surrogate-fuel variation. The latter two series use fuel parameter variations where only soot yield is altered. For this variation, high values of the correlation factors correspond to higher soot yields, and vice versa. All plots show that the estimated values are in good agreement with the simulated values. Most notably is the plot for the fast growth rates (lower row), where the ratios for relatively high correlation factors seem to change in the opposite directions.

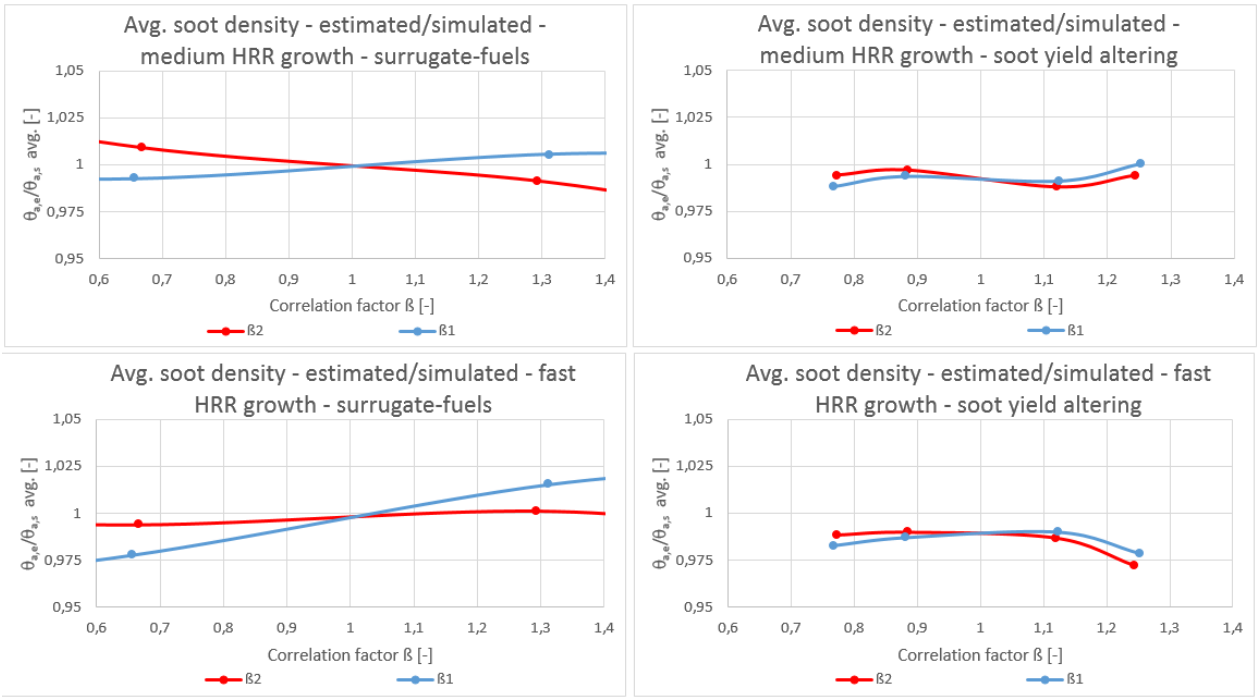

Figure 4.16 Model A, surrogate-fuels compared to fuels where only soot yield is altered. Series from upper left: 1, 13, 2, 14.

In Figure 4.17, both plots show results from simulations applying Model A and fast HRR-growth. The left plot show results using surrogate-fuels (series 2). The right plot show results applying the GM-series (series 15). For the GM-series, high values of the correlation factors correspond to low GM-numbers. Notice should be taken as to the non-linearity of the ratios for the GM-series. The non-linearity is generally higher for correlation factor 2 than 1. However, a relatively large drop in ratios is observed going from the second highest to the highest value of correlation factor 1.

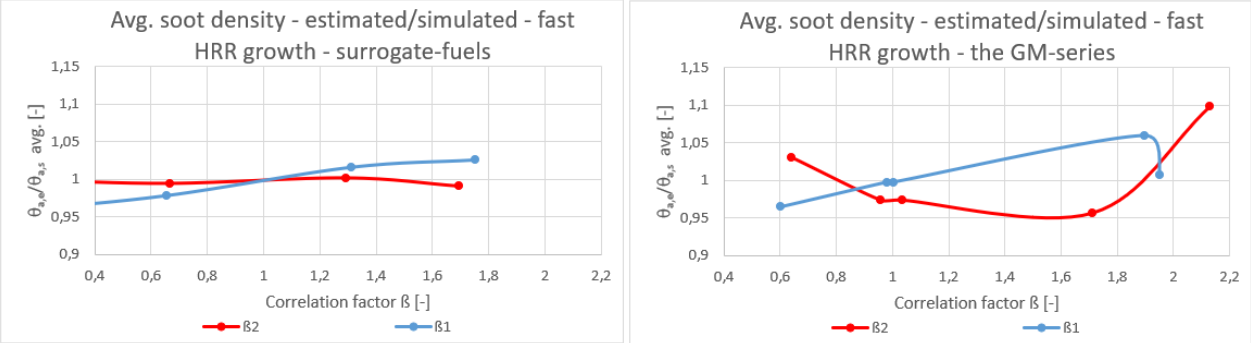

Figure 4.17 Model A, surrogate-fuel series 2 (left) and the GM-series 15 (right).

4.3. Trendline ratios

The trendlines, T_θ, are the linearization of data in the plots provided in section 4.2 and Appendix B.1-B.3, computed using eq. 3.14. In this section, the ratios of these trendlines T_S/T_{CO} are applied to convey differences in estimation precision due to estimated quantity, i.e. soot density and CO mass fraction. The ratios of the trendlines (vertical axis) are plotted against values of X (here, representing correlation factor-values along the horizontal axis). In Figure 4.18, the average values of the trendline ratios, for the statistical volume mean (solid lines) and volume maximum (dotted lines) are plotted for correlation factor 1 (blue lines) and 2 (red lines), against values of X representable for most values of correlation factors applied in this study. The trendline ratios are averaged over *all* simulation series and positions of measurement. For simulation series in Model A (15 series) one position of measurement is applied. For simulation series in Model B (4 series), there are two positions of measurement. As such, Figure 4.18 convey the average values of T_S/T_{CO}, consisting of 23 ($15 \cdot 1 + 4 \cdot 2$) trendline ratios, for every form of statistical volumetric output (mean and maximum) and correlation factor.

Ratios tend to decrease and increase slightly with decrease and increase of X-values respectively. However, the average values of the trendline ratios are generally very close to unity, with the highest average discrepancy of 2%. This indicates that soot densities and CO mass fractions are, on average, estimated rather similarly. Thereby, it is deemed reasonable to choose only one output quantity for depiction of representable estimation discrepancies (in sections 4.1 and 4.2), herein the statistical volumetric mean soot density values.

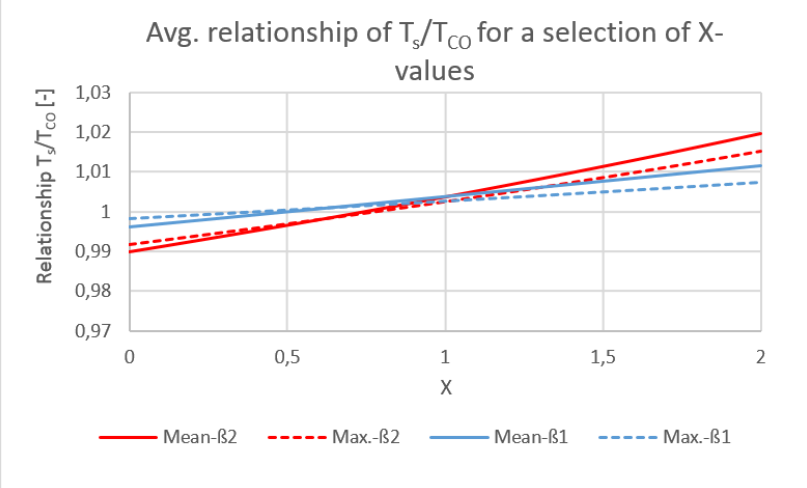

Figure 4.18 Ratios of the trendlines, T, for soot density and CO mass fractions. The plot shows the average ratio of all trendlines for selected X-values.

4.4. Summarized performance

The performance of the correlation factors are summarized in Figure 4.19, and Table 4.2 through Table 4.5. The percentile discrepancies are calculated using eq. 3.15, based on the data provided in section 4.2 and Appendix B.1 through B.3.

Figure 4.19 show columns of the numbers of estimation discrepancies within selected percentile intervals. Left and right plot-column show the soot densities and CO mass fractions respectively. The two upper plots illustrate the number of discrepancies for both statistical volumetric medium and maximum output quantities. The four lower plots differentiate the number of estimation errors within percentile intervals for statistical volumetric mean and maximum output quantities. The plots show that most discrepancies are within ∓5%. Additionally, more of the estimations ascertained by use of correlation factor 1, attain discrepancies in the lower percentile intervals, ∓2,5%. All discrepancies above 20% stem from estimations of output from simulations in Model B, using low values of correlation factor 2 and low HRRs. The largest attained discrepancy is approximately 22% (series 19, measurement I, see Figure 4.15).

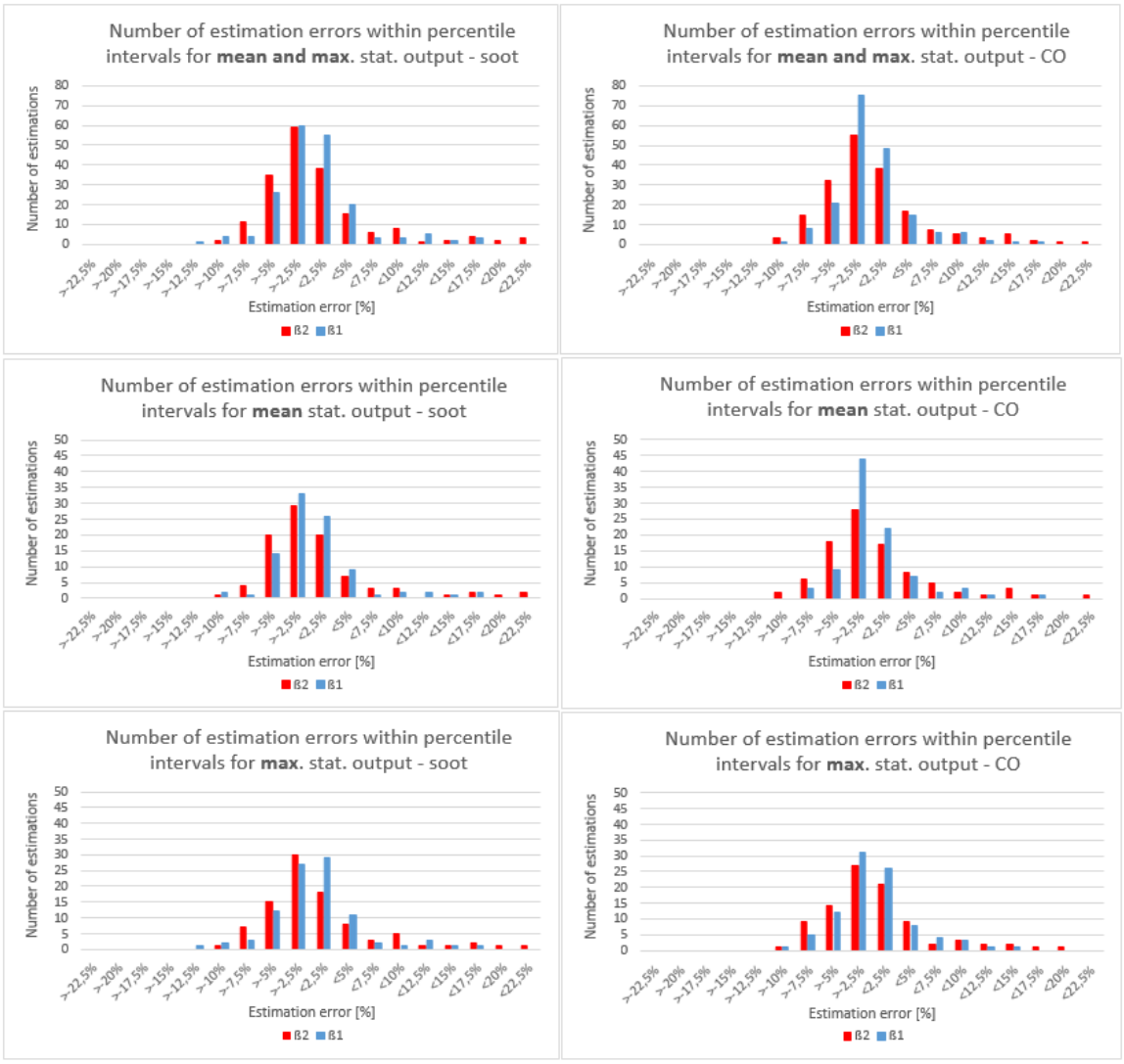

Figure 4.19 The number of estimation discrepancies within percentile intervals for all estimations.

The percentiles of estimation discrepancies within percentile intervals of ∓5%, ∓10% and between 20% and 22,5%, are shown in Table 4.2 and Table 4.3. In both tables, forms of statistical output are differentiated. The tables also show the total number of estimations. The first table show the results for soot density values, the second table show results for CO mass fraction values. This depiction suggests that there are little differences in discrepancies between estimations of different species quantities and different forms of statistical output, for the percentile intervals applied.

Table 4.2 Percentile of estimations with estimations errors within selected percentile intervals. Soot density values.

Statistical output	Mean and maximum	Mean	Maximum
Total number of estimations	372	186	186
Percentile discrepancy intervals	**Percentile of estimations within given percentile interval**		
$< \lvert \mp \mathbf{5}\% \rvert$	82,6 %	84,9 %	80,6 %
$< \lvert \mp \mathbf{10}\% \rvert$	93,9 %	94,1 %	93,5 %
$\mathbf{20}\%$ **to** $\mathbf{22,5}\%$	0,8 %	1,1 %	0,5 %

Table 4.3 Percentile of estimations with estimations errors within selected percentile intervals. CO mass fraction values.

Statistical output	Mean and maximum	Mean	Maximum
Total number of estimations	372	186	186
Percentile discrepancy intervals	**Percentile of estimations within given percentile interval**		
$< \lvert \mp \mathbf{5}\% \rvert$	81,8 %	83,8 %	80,4 %
$< \lvert \mp \mathbf{10}\% \rvert$	95,7 %	95,7 %	95,7 %
$\mathbf{20}\%$ **to** $\mathbf{22,5}\%$	0,3 %	0,5 %	0,0 %

The percentiles of estimation discrepancies within percentile intervals of ∓5%, ∓10% and between 20% and 22,5%, are shown in Table 4.4 and Table 4.5. In both tables, forms of statistical output are differentiated. The tables also show the total number of estimations. The two tables differ in use of correlation factor. The first and second table show results attained applying correlation factor 1 and 2 respectively. The tables indicate that, on average, correlation factor 1 performs better than correlation factor 2, for all depicted percentile intervals.

Table 4.4 Percentile of estimations with estimations errors within selected percentile intervals. Correlation factor 1

Statistical output	Mean and maximum	Mean	Maximum
Total number of estimations	372	186	186
Percentile discrepancy intervals	**Percentile of estimations within given percentile interval**		
$< \lvert \mp \mathbf{5}\% \rvert$	86,5 %	88,6 %	84,3 %
$< \lvert \mp \mathbf{10}\% \rvert$	96,0 %	96,2 %	95,7 %
$\mathbf{20}\%$ **to** $\mathbf{22,5}\%$	0,0 %	0,0 %	0,0 %

Table 4.5 Percentile of estimations with estimations errors within selected percentile intervals. Correlation factor 2

Statistical output	Mean and maximum	Mean	Maximum
Total number of estimations	372	186	186
Percentile discrepancy intervals	**Percentile of estimations within given percentile interval**		
$< \lvert \mp \mathbf{5}\% \rvert$	77,9 %	79,5 %	76,8 %
$< \lvert \mp \mathbf{10}\% \rvert$	93,5 %	93,5 %	93,5 %
$\mathbf{20}\%$ **to** $\mathbf{22,5}\%$	1,1 %	1,6 %	0,5 %

5. Discussion

The results of this study, and possible causes for the observed discrepancies between estimation and simulation are discussed in this chapter. The discussion primarily revolves around relating the various simulation series characteristics to tendencies of estimation discrepancies by use of the correlation factors. First, in section 5.1, causations between discrepancies, and both the HRR and positions of measurement, are discussed. In section 5.2, the effects of enabling aerosol transport and soot deposition mechanisms are elaborated. Further, in section 5.2, inquiries are made as to the potential causations between discrepancy tendencies and different fuel parameter variations. Section 5.4 discusses variations in estimation discrepancy for different forms of mass quantity output and the correlation factors. Additionally, section 5.4 discusses the overall performance of the correlation factors and applicability.

The structure of each section is generally similar. First, references are made to sections in the results chapter and the associated results. Further, the most significant results are described, and causations for observed estimation discrepancies are discussed.

5.1. Discrepancies due to revised HRR and position of measurement

In this section, results presented in section 4.2.1 are discussed. These results apply simulation series 1 through 5 (Model A) and series 16 through 18 (Model B). All series in the section apply the lumped species transport method (default in FDS) for all species (including soot). This entails that all species are treated as gaseous species, and no deposition mechanisms are activated [17]. Additionally, all series apply the surrogate-fuel method (fuel parameter indexes from 0 to 10). No series apply the same value of HRR.

The largest discrepancy using growing HRRs and Model A (series 1 and 2) was attained using medium HRR growth and correlation factor 2 with a value of 0,15. This was an overestimation of approximately 4% (see Figure 4.8). Series 3, 4 and 5 applied Model A and constant HRRs of 1000, 1500 and 2000 kW respectively. For these series, the largest discrepancies were attained using the highest value of HRR (series 5) and correlation factor 1. The lowest and highest value of correlation factor 1 yielded under- and overestimations respectively of approximately 8% (see Figure 4.9). For the series using Model B, series 16, 17 and 18, HRRs of 3000, 5000 and 7000 kW were applied respectively. Two positions of measurement were used in the Model, herein measurement I and II, where the former was located furthest away from the fire origin. The largest discrepancies were attained applying correlation factor 2, the lowest value of HRR (series 16), and measurement I. The lowest and highest values of correlation 2 factor yielded over- and underestimations of 20% and 9% respectively (see Figure 4.10).

One of the most notable tendencies, common for all results depicted in section 4.2.1, was the increased similarities of individual simulation results in each series, as the value of HRRs increase. For instance, Figure 4.9 depict the results of series 3, 4 and 5, applying Model A and HRRs of 1000, 1500 and 2000 kW respectively. For low HRRs (series 3) and low values of correlation factors, the values of $\frac{\theta_{a,estimated}}{\theta_{a,simulated}}$ were close to unity. As higher values of HRR were applied, going from series 3 to 5, the ratios of $\frac{\theta_{a,estimated}}{\theta_{a,simulated}}$ were reduced, for the low correlation factor-values. This means that the simulated values were increasingly higher than the estimated values, or rather, that the estimated value of simulation a, was closer to the base

simulation b, than predicted by the correlation factors. For high values of the correlation factors, the increased similarities between simulation results of individual simulations in a series, are indicated by increased values of $\frac{\theta_{a,estimated}}{\theta_{a,simulated}}$. This is due to the simulated value being lower than the estimated value, and thereby closer to the value of the base simulation (examples of discrepancy-interpretations are provided in section 3.4.1). For Model B, the same tendency of increased similarities between the base simulations and the remaining simulations in the series, was also observed when the distance between the position of measurement and fire origin was reduced (going from measurement I to II, depicted in Figure 4.10 and Figure 4.11 respectively).

To summarize the above, the results of section 4.2.1 indicates that mass quantity results of individual simulations in a series become increasingly similar, compared to the estimations given by the correlation factors, as HRRs increase and/or when the distance between the position of measurement and fire origin is reduced. This may be due to the increased energy content, and magnitude of the turbulent structures of the flow, for either high levels of HRR or in the vicinity of the fire. For such cases, the turbulent characteristics of the flow, may be somewhat more dominating to the mixing rate of the species. As such, the variation in species mass production rates (eq. 3.4) between individual simulations in a series, may be less influential to species mixing. However, the species mass production rates (function of correlation factor 1, eq. 3.4) should still account for all mass of the species being introduced to the computational domain. If species mass concentrations of individual simulations in a series are more similar than predicted by the correlation factors in one location, the concentrations should therefore be more dissimilar in a different location. These dissimilarities appear where turbulent mixing is less dominant, herein for series applying low values of HRR and/or distant to the fire origin. Subsequently, the observed tendencies of relatively increased dissimilarities of measured species quantities may also be interpreted as similarities in species mass accumulation rates between individual simulations in a simulation series, prior to reaching the position of measurement. For instance, if the mass accumulation rates of a species are somewhat similar in simulation a and b, and more mass is being produced in b, then comparably less mass (also accounting for differences in mass production rates) will be convectively transported from one location to another in simulation a. This causation is quite plausible, considering that neither correlation factor accounts for differences in accumulation rates or convective transport of a species (see eq. 2.36, mass transport).

5.2.Discrepancies du to soot deposition

In this section, results presented in section 4.2.2 are discussed, where series using different transport mechanisms for soot, and options for soot deposition, are compared. These series include 1 through 12 in Model A, and 17 and 19 in Model B. Common for all series are the fuel parameter-variation, herein the surrogate-fuel method (indexed 0 to 10). Deposition mechanisms applied are (default of FDS) gravitational settling, thermophoresis (movement towards or away from walls due to temperature gradients), diffusive deposition (migration due to concentrations gradients) and turbulent deposition (deposition due to impact) [16]. Additionally, default soot particle properties have been employed.

The series applying HRR growth rates (1, 2 and 6 through 9) are depicted in Figure 4.12 and Figure 4.13. In series 1 and 2, soot was transported as a gas, while series 6 and 8 transported soot as an aerosol, without enabling soot deposition mechanisms. For series 7 and 9, soot was transported as an aerosol and deposition

mechanisms were activated. For all these series, there were essentially no differences in estimation discrepancy. This is likely due to the gravitational and thermophoretic velocities, being relatively small compared to the convective velocity term in the mass transport equation (eq. 2.36). Thereby, when treating soot as an aerosol, but without deposition mechanisms, the solutions to the mass transport equations may generally be similar to simulations where soot is treated as a gaseous species. Further, when the soot mass production rate is also relatively small (which may be the case in early stages of a growing fire), differences in estimation discrepancies due to adding soot deposition may also be somewhat small.

However, when applying constant HRRs for the series applying Model A (series 3, 4, 5 and 10, 11, 12) and Model B (series 17 and 19), active soot deposition mechanisms yielded slightly increased dissimilarities between individual simulations in each simulation series (recalling increased dissimilarities signify increased and decreased ratios of $\frac{\theta_{a,estimated}}{\theta_{a,simulated}}$ for low and high values of the correlation factors respectively). This is likely due to soot deposition acting like a mass sink, effectively adding a subsequent source term to the mass transport equation [16]. As the added mass source term is not accounted for by the correlation factors, deposition mechanisms could increase the differences in mass quantity simulation results between individual simulations in a series. This, for instance, due to non-linear alterations in mass deposition for linear alterations in fuel parameters. Since Model A, without soot deposition (series 3-5), tended to yield increased similarities between individual simulations in a series, when HRR was increased, adding soot deposition (series 10-12) generally *reduced* discrepancies (see Figure 4.14). Adversely, without soot deposition in Model B (series 17), results of individual simulations in the series tended to be more dissimilar. Thereby, adding soot deposition (series 19) and effectively increasing the dissimilarities due to the added mass source term, discrepancies were *increased* (see Figure 4.15).

5.3.Discrepancies due to fuel-type variations

In this section, results presented in section 4.2.3 are discussed, where series using miscellaneous fuel types are compared. Series applied for comparison are 1, 2, 13, 14 and 15. Common for all series is the use of growing HRRs and Model A.

Simulation series 1 and 2 are compared to 13 and 14 in Figure 4.16. The former two apply the surrogate-fuel method, while in the two latter, individual simulations in each series differ only in terms soot yield. Series 1 and 13 apply medium HRR-growth rate, while series 2 and 14 apply fast HRR-growth. For all of these series, only low estimation discrepancies are attained. The largest discrepancy, using the soot yield-variation, was attained for fast HRR-growth (series 14) and high correlation factor-values. This discrepancy was an underestimation of approximately 2,5% (both correlation factors). In comparison, the surrogate-fuel variation attained an overestimation of approximately 2% (correlation factor 1). The discrepancy seen for series 14, may be caused by the relation between heat loss and the soot content of the smoke. Generally, when the soot content increase, so does heat loss by thermal radiation [9]. When heat is lost, the gas temperature is reduced. Considering the relation between temperature and density (asserted through the ideal gas law, eq. 2.44), reduced temperatures coincide with increased densities. As such, the correlation factors may yield underestimations when *only* soot yield is increased. However, the opposite tendency is not observed when reducing soot yields (corresponding to a low correlation factor) in the same simulation series (series 14), rendering the causation somewhat inconclusive. It must be noted, however, that linear

alterations in fuel input parameters should not be expected to yield linear alterations in the energy transport equations (via, for instance, heat loss). As such, the causation may be valid, but not necessarily particularly influential.

Simulation series 2 is compared to simulation series 15 in Figure 4.17. Both use fast HRR growth rate. The former applies the surrogate-fuel method, while the latter apply the polyurethane GM-series. The two plots of time averaged ratios of $\frac{\theta_{a,estimated}}{\theta_{a,simulated}}$ against correlation factors differ mainly in two manners. First, there are relatively large differences in discrepancies between estimations using different correlation factors. For instance, for high values of the correlation factors, there is a difference of approximately 10% between the estimation discrepancy using correlation factor 1 and 2. This is due to the relatively large differences in correlation factor-values between correlation factor 1 and 2 for the GM-series (which can also be seen in Table 4.1). Second, the plots of the GM-series are more non-linear than the surrogate-fuel series. This is likely due to all fuel parameters being linearly altered in the surrogate-fuel method, while in the GM-series, fuel parameter-alterations between individual simulations are non-linear (see Table 4.1). Estimation discrepancies using correlation factor 2 may be considered especially non-linear. From the second highest to highest correlation factor-value, the estimation discrepancies change from -5% to +10%, a difference of 15%. This may be due to one fuel-parameter in particular, namely the heat of combustion per unit mass of oxygen, $\Delta H_{C,ox}$. The second highest and highest value of the correlation factor correspond to fuel parameters associated with GM 27 and GM 23 respectively. Table 4.1, show that $\Delta H_{C,ox}$ alters from $11{,}2\ kJ/g_{ox}$ to $13{,}7\ kJ/g_{ox}$, for GM 27 and GM 23 respectively, which is both the lowest and highest value of $\Delta H_{C,ox}$ applied in this study. The base simulation applies $\Delta H_{C,ox} = 12{,}6\ kJ/g_{ox}$. As $\Delta H_{C,ox}$ is reduced for the same value of HRR, the need for oxygen supply increases. When oxygen supply is increased, the hot product gases may be prone to increased cooling due to more interactions with air. Considering the ideal gas law (eq. 2.44), reduced gas temperatures may correspond to increased densities. As such, relatively high and low values of $\Delta H_{C,ox}$, compared to the base simulation, may correspond to over- and underestimations respectively. For the case of the surrogate fuels, however, the differences in $\Delta H_{C,ox}$ between individual simulations are relatively small compared to the differences between GM 27 and GM 23. Nor does the tendencies of estimation discrepancy seem to follow the above-stated causation with alterations in $\Delta H_{C,ox}$. As such, the differences in $\Delta H_{C,ox}$ between simulation a and b likely needs to be particularly high for the variable to be particularly influential.

5.4. Statistical performance and evaluation of applicability

In this section, statistical results presented in section 4.3 and 4.4 are mainly discussed. Results presented in other sections of the results chapter are also discussed when relevant. First, section 5.4.1 discusses differences in estimation discrepancies for the different mass quantity outputs, and what output may potentially be best predicted. This includes the four measured mass output quantities, herein the statistical volumetric mean and maximum soot densities and CO mass fractions. Second, which correlation factor may perform better, and under what circumstances, is discussed in section 5.4.2. Lastly, section 5.4.3 discusses overall performance of the correlation factors, and potential limits of applicability.

5.4.1. Differences in discrepancies due to form of mass quantity output

Results presented in section 4.3 and 4.4 facilitate the means of discussing differences in estimation discrepancies for the different forms of mass quantity output.

In section 4.3, Figure 4.18, the trendline ratios, T_S/T_{CO}, averaged over the trendlines for every simulation series in this study are presented. The ratios of T_S/T_{CO} are plotted against values of X, representative for the scale of correlation factor-values mostly applied in this study. Statistical volumetric mean and maximum output, as well as individual correlation factors, are differentiated. The trendline ratios indicate that estimation discrepancies were generally similar independent of whether density- or mass fraction measurements were made. This was the case for both statistical volumetric mean and maximum output. A maximum average relative difference in estimation discrepancy between soot density measurements and CO mass fraction measurements of approximately 2% was attained (mean statistical output, correlation factor 2). As such, the trendline ratios indicate that, on average, estimation discrepancies for different values of the correlation factors (represented by X) and for different forms of mass quantity output, were essentially the same. Since the trendlines of T_S and T_{CO} are based on estimation discrepancies due to estimations of soot densities, ρY_S, and CO mass fractions, Y_{CO}, respectively, the small deviations of T_S/T_{CO} from unity is either due to the average difference in the bulk density, ρ, between individual simulations in a series, or due to the difference of estimating a soot-quantity or a CO quantity. As FDS applies the lumped species approach [16], the choice of primitive product species to be estimated is generally arbitrary. Thereby, it is likely that ρ was, on average, slightly altering between individual simulations in a series.

For evaluation of which species mass quantity (soot densities or CO mass fractions) may be better predicted, the results depicted in Table 4.2 and Table 4.3, are considered. In particular, the columns showing the combined percentiles of estimations for both statistical mean and maximum values are reviewed (most left column). The soot density estimations were slightly more precise in the discrepancy interval of $\mp$5% than CO mass fractions. 82,6% versus 81,8% of the estimations were within this percentile interval respectively. However, for the discrepancy intervals of $\mp$10% and 20% to 22,5%, CO mass fraction-estimations performed more favourably than soot density estimations. Here, 95,7% versus 93,9% and 0,3% versus 0,8% of the estimations were within these discrepancy percentile distributions respectively. As such, this study suggests that CO mass fractions may be somewhat better predicted than soot densities. Considering that soot density is dependent on two variables (density, ρ, and mass fractions, Y_S), while CO mass fraction is only dependent on one (Y_{CO}), this may be plausible. However, the differences were, on average, miniscule.

To discuss which statistical mass quantity output (mean or maximum) may be better predicted, the results depicted in section 4.4, Table 4.2 and Table 4.3, are again considered. These tables show the percentile of estimations within given intervals of percentile estimation discrepancies. Statistically, there were little differences in accuracy between estimations of statistical volumetric mean or maximum values. The largest differences occur in the percentile interval of $\mp$5%. Approximately 84% to 85% of all statistical mean values performed within this discrepancy interval, compared to approximately 80,5% of the statistical maximum values. This suggests that estimations of the statistical volumetric mean values may be somewhat more precise than the maximum values. However, in the discrepancy interval of 20% to 22,5%, the statistical maximum values were estimated somewhat more favourably, by approximately 0,5 percentage points. Nonetheless, the overall results of this study seem to suggest that volumetric mean values may be somewhat better predicted than maximum values. This may be due to modelling of mass diffusive transport, which is

mass migration due to concentration gradients [15]. It is likely that the grid cell containing the maximum value of a species quantity, also contains a higher concentration of that species than any of its adjacent grid cells. As such, the species variable in that grid cell may be especially prone to alterations in diffusive transport, between different simulations in a series. However, the differences between measuring mean and maximum values were, on average, rather small.

5.4.2. Best performing correlation factor

Section 4.4, Table 4.4 and Table 4.5, convey the percentiles of estimations within intervals of selected percentile discrepancies. These intervals are ∓5%, ∓10% and 20% to 22,5%. From these tables, it appears correlation factor 1 predicted the mass quantity values better than correlation factor 2, for all depicted percentile intervals. The differences in estimation precision were especially pronounced in the ∓5% percentile interval. For the statistical volumetric mean and maximum statistical output combined, 86,5% of all estimations applying correlation factor 1 were within this interval, compared to 77,9% using correlation factor 2, a difference of 8,6 percentage points. This suggests that correlation factor 1 was, on average, better suited for estimating mass quantity output. This may be due to correlation factor 1 accounting for the mass production rates, prone to change the lumped product species mass fraction, Z_p (which is the mass transport variable of FDS). For correlation factor 2 to make reasonable predictions on the other hand, Z_p (and density, ρ, for species density measurements) needs to change considerably less than the mass fractions, $a_{\alpha,p}$, of the primitive species, α, in the lumped product species.

However, for the surrogate-fuel variations (fuel simulation indexes 0 to 10), which is used for most simulations in this study, correlation factor 1 is higher than 2 for low values of the correlation factors, and vice versa (see Table 4.1). Therefore, the best performing correlation factor depended on whether under- or overestimations were likely for either high or low values of the correlation factor. This signify that correlation factor 1 predicted higher dissimilarities between simulation results in a simulation series. As described in section 5.1, estimations in simulation series where the position of measurement is in the vicinity of the fire origin and/or when the value of HRR is high, individual simulation results in the series were generally more similar than predicted by the correlation factor (for instance series 4 and 5 depicted in Figure 4.9). In such cases, correlation factor 2 may be preferred. Adversely, for estimations of quantities distant to the fire origin and/or series with low values of HRR, simulation results were generally more dissimilar than predicted by the correlation factors (for instance series applying Model B, depicted in Figure 4.10). In such cases, correlation factor 1 may be more favourable.

5.4.3. Overall performance and applicability

The overall performance is evaluated by averaging the values of the combined statistical volumetric mean and maximum values in Table 4.2 and Table 4.3 (most left column) (the same values may also be attained by averaging the values in Table 4.4 and Table 4.5 (most left column)). Out of a total of 744 estimations, 82,2% and 94,8% performed within the discrepancy percentile interval of $\mp 5\%$ and $\mp 10\%$ respectively. Approximately 0,5% deviated above 20%, with a maximum deviation of approximately 22%. Considering the scope of values of correlation factors, mostly approximately 0,14 to 1,7 (see Table 4.1), estimations by use of the correlation factors may be deemed reasonable. This scope is indicative of the difference in fuel parameters between the base and estimated simulation, possibly causing alterations in the FDS transport equations for mass, momentum and energy. Thereby, increasing the difference between unity and the value of the correlation factors, corresponds to increased potential for estimation discrepancy. This is also seen for almost all simulation series, namely, relatively small and large correlation factor-values, generally correspond to reduced estimation precision, and thereby reduced applicability.

Further, applicability of the correlation factors may also be evaluated in terms of the scenarios of which they may be used. For instance, if the visibility distance through smoke is evaluated, acceptable visibility is dependent on low values of soot density. For a visibility distance of 10 m, and using the default values of FDS to compute this distance (see section 2.4.5), a soot density value of approximately 0,03 g/m^3 is needed (solving eq. 2.42 for ρY_S). In comparison, for series 16 (Model B and HRR=3000 kW), measurement I, a time averaged value of approximately 0,3 g/m^3 was the lowest attained in this series (fuel parameter index 10). As such, attaining decent visibility distance may require the measurement to be made particularly far away from the fire origin and/or for a scenario where the value of HRR is very low. From the results in this thesis, such cases may be especially prone to over- and underestimations for low and high values of the correlation factors respectively (see for instance Figure 4.10, depicting results from Model B).

Lastly, the applicability and reliability of the correlation factors may be increased by use of several base simulations, instead of merely one, which was the procedure of this thesis. This would potentially be beneficial in that the tendency of discrepancy may be revealed. For instance, for the series applying surrogate-fuels in this study (all except 13-15), the discrepancy tendencies were generally somewhat linear, relative to the value of correlation factor. This linearity may be exploited in evaluating the likely estimation discrepancy for a new set of simulation series. Knowing the potential tendency of estimation discrepancy, could naturally be used to make more accurate predictions. However, for series in Model B, estimation discrepancies for underestimations tended to be somewhat higher than discrepancies for overestimations. As such, pristine linearity should naturally not be expected. Additionally, for the GM-series, individual fuel simulation parameters varied non-linearly (see Table 4.1), relative to alterations in correlation factor-values. Thereby, estimation discrepancies were also non-linear, especially for correlation factor 2.

6. Conclusion

The objective of this thesis has been to investigate the feasibility of applying the results of one FDS simulation to encompass estimations of other simulations species mass quantity-results (i.e. densities and/or mass fractions of soot, CO, etc.) if fuel simulation input parameters are revised. In this context, fuel parameters refer to chemical composition of the fuel, product species yields (such as CO and soot) and heat of combustion. If reasonable estimations of simulation output may be produced based on only one simulation, possible consequences of alterations in simulation parameters may be revealed, using far less recourses compared to conducting several simulations.

To investigate this possibility, correlation factors have been developed and proposed (in chapter 3). These assume that functions exist for correlating mass quantity output of two simulations applying different sets of fuel parameter input. Two correlation factors, defined as functions of input parameters of two simulations, have been developed. The first, correlation factor 1, emphasize the significance of the source term to the FDS mass transport equation, namely the species mass production rate. The second is based on the method of which FDS retrieves information about the primitive species mass fractions from the lumped species.

To assess the performance of the correlation factors, 93 simulations have been conducted, divided over 19 different simulation series (series are listed in section 3.2.8). Each series consists of 4-5 simulations, whereas one of these is the *base* simulation. The mass quantity output of the base simulation has been multiplied with each individual correlation factor to predict the mass quantity output of the other simulations in the series. The estimations have further been compared to the actual simulations, facilitating the means of assessing potential tendencies of estimation discrepancy. For every *individual* simulation in each series, *only* fuel parameters are altered. The magnitude of fuel parameter variations between individual simulations are indicated by the value of the correlation factors. Most correlation factor-values of this study varied between approximately 0,14 to 1,7 (see Table 4.1). For every simulation *series*, parameters concerning Model geometry (two different geometries), HRR (8 different HRRs), fuel-type variation (3 different variations), and mode of soot transport mode have been altered. These parameters were assumed to affect the solutions to the FDS mass transport equations, and thereby, the estimation precision.

The assessed species mass quantity outputs were the statistical volumetric mean and maximum values of soot densities and CO mass fractions. The quantities were measured in stationary volumes located near the ceiling in different distances from the fire origin. In the smallest Model geometry (Model A), one location was used, relatively near the fire origin (see Figure 3.2). In the largest Model geometry (Model B), two locations have been applied, one far away from the fire origin and one somewhat closer (see Figure 3.4).

To evaluate the feasibility of correlating input and output from different simulations, this study has focused on potential differences in estimation discrepancy due to characteristics of the simulated fire scenarios. Additionally, findings regarding potential differences in estimation discrepancy due to the form of mass quantity output, as well as the differences in estimation precision for the individual correlation factors, are sought. Tendencies for either under- or overestimations for low or high values of the correlation factors are of particular interest. Under- and overestimations for low and high values of the correlation factors respectively, signify that the mass quantity results of individual simulations in a series are more similar than predicted by the correlation factors. Oppositely, over- and underestimations for low and high values of the correlation factors, signify that values of mass quantity output of individual simulations in a series are more dissimilar than predicted by the correlation factors (see example in section 3.4.1). The main findings of the study are described in the following paragraphs.

Causations between the value of HRR and the distance between the fire source and position of measurement have been evaluated (provided in section 5.1). The findings suggest that mass quantity output from individual simulations in a series are slightly more similar (under- and overestimations for low and high values of the correlation factors respectively) than predicted by the correlation factors, when the value of HRR is relatively large, and/or when measurements are made in the vicinity of the fire origin. Adversely, when HRR is low and/or when measurements are made distant to the fire, mass quantity output from individual simulations in a series are more dissimilar than predicted by the correlation factors.

The effects on estimation precision due to enabling or disabling soot deposition mechanisms are discussed in section 5.2. In this study, default soot particle properties and deposition mechanisms were applied. In conclusion, enabling soot deposition slightly increased the dissimilarities between individual simulations in the simulation series. As such, for simulation series where mass quantity output from individual simulations in the series were more similar and dissimilar to each other than predicted by the correlation factors, estimation discrepancies were reduced and increased respectively, when enabling soot deposition mechanisms.

In section 5.2, inquiries are made as to the differences in estimation precision due to fuel parameter variations. Findings indicate that increased soot yields relative to the base simulation, may have caused increased thermal radiative heat loss, that in turn reduced the temperature of the smoke. This could subsequently result in increasing densities relative to the base simulation, leading to underestimations by use of the correlation factors. However, the adverse effect was not observed when reducing the soot yields, rendering the causation somewhat ambiguous. Further, it was found that relatively large alterations in heat of combustion per unit mass of oxygen consumed, $\Delta H_{C,ox}$, could particularly influence the estimation precision. Increased $\Delta H_{C,ox}$, relative to the base simulation, reduce the necessity for oxygen (or air) entrainment to sustain a specified HRR. Thereby, less interaction between the hot gases and air may occur, inhibiting cooling of the hot gases. As increased temperatures coincide with reduced densities, increased $\Delta H_{C,ox}$ relative to the base simulation may cause overestimations for high values of the correlation factors. Adversely, reduced $\Delta H_{C,ox}$ could cause underestimations. However, the phenomenon is only seen when the base simulation and the simulation of which estimations are made, apply particularly different values of $\Delta H_{C,ox}$.

Differences due to the mass quantity output, herein the four different types assessed, statistical volumetric mean and maximum soot densities and CO mass fractions are discussed in section 5.4.1. On average, only miniscule differences in estimation precision was observed, suggesting that the form of estimated statistical volumetric output, and primitive product species, was relatively arbitrary.

Section 5.4.2 discusses what correlation factor is most applicable and under what circumstances. Since the values of the two correlation factors were rather similar, the differences in estimation discrepancies were generally small. However, dividing discrepancies into percentile intervals of ∓5%, ∓10% and 20 to 22%, out of a total of 372 estimations per correlation factor (all estimations included), correlation factor 1 performed somewhat more favorably in all intervals. In particular, correlation factor 1 performed better in the interval of ∓5%, with a favourable difference of 8,6 percentage points (86,5%-77,9%). This is likely due to correlation factor 1 accounting for the species mass production rates, prone to alter the transported lumped product species mass fraction variable, Z_p. However, for most simulation series (using the surrogate-fuel variations), the correlation factor values differed in that correlation factor 1 predicted higher dissimilarities than correlation factor 2, between individual simulations in a simulation series. Thereby, for

series where individual simulations mass quantity results were generally more similar than predicted by the correlation factors, correlation factor 2 made better estimations. Oppositely, for series where individual simulations were generally more dissimilar than predicted by the correlation factors, correlation factor 1 performed more favourably.

Finally, overall precision and applicability of the correlation factors is discussed in section 5.4.3. From the 93 simulations conducted, 744 estimated results have been produced and compared to actual simulations. Dividing discrepancies into intervals, out of the 744 estimations, 82,2% and 94,8% performed within the discrepancy percentile interval of ∓5% and ∓10% respectively. Approximately 0,5% deviated above 20%, with a maximum deviation of approximately 22%. As such, there was generally good agreement between the estimations and simulations. Even if some over- and underestimations were made for a few series, these may be deemed minor.

Thereby, the results of this study suggest that reasonable estimations of mass quantity output of a simulation with revised fuel parameter input relative to a base simulation are feasible. This by applying the correlation factors presented and mass quantity output of a base simulation. As such, the correlation factors may provide effective means of increasing insight as to possible consequences of altering fuel parameter input of a simulation. Compared to conducting multiple simulations, the procedure is naturally less computationally expensive. Nonetheless, it must be noted that the findings of this study mainly apply for the series of simulations performed. However, given that other simulation series bear similar scenario characteristics, it is likely that the observed tendencies of estimation precision and deviation are applicable. As this is naturally quite challenging to precisely determine, the correlation factors should be used with caution. The simplest manner of reducing uncertainty is to refrain from estimations of simulation results where fuel parameter simulation input differs significantly from the base simulation. Such differences are often indicated by the value of the correlation factors. Large differences between unity and the value of the correlation factor indicate large differences in fuel parameter input, which generally coincide with increased potential for estimation discrepancy. Additionally, applying several base simulations instead of only one may also provide insight as to the tendency of estimation discrepancy, due to alterations in fuel parameter input (discussed in section 5.4.3). Such insight, however, depends on somewhat linear alterations in fuel parameters, for instance through the surrogate-fuel method.

6.1. Further studies

As to further studies, the following suggestions are made to enhance the precision and reliability of the correlation factors:

- **Validation:** investigate whether correlation factors and their potential discrepancies correspond with experimental data. Simulation- and experiment series likely needs vast simplifications compared to the series investigated in this study. A large enclosure would be preferred, to emulate typical building fire scenarios. However, trade-offs normally need to be made between enclosure size, costs and number of possible experiments. Validation experiments may be conducted by applying different fuel mixtures, preferably in liquid and/or gaseous form. This to better control the fuel loss rate and facilitate estimations of HRR. Additionally, the characteristics of the fuel parameters need to be well known.
- **Scenarios:** conduct simulations of scenarios where mass quantities are in the border-line of tenability criterions for egress. For soot density values, this may require low HRR and/or large distances from the origin of fire, possibly causing increased differences in species fractions between individual simulations in a series than predicted by the correlation factors. This meaning over- and underestimations for low and high values of the correlation factors respectively (as seen for many simulations applying Model B, see for instance Figure 4.10).
- **Measurements:** conduct simulations where point-data devices, measuring species mass quantities, are included in vertical and horizontal arrays from the floor to the ceiling and away from the fire source respectively. This may reveal discrepancy tendencies due to relative redistribution of mass (mixing effects) in different positions in the enclosure relative to the hot gas layer and fire source. Insight as to the role of the accumulation rate and/or convective transport mechanisms on the discrepancy tendencies may be provided using such simulation set-ups.
- **Parameter sensitivity:** findings of this study has indicated what fuel parameters may be especially significant regarding estimation discrepancies by use of the correlation factors (for instance soot yields and heat of combustion per unit mass of oxygen consumed). A thorough parameter sensitivity study, altering individual fuel parameters between each simulation, may yield increased insight as to the significance of each fuel parameter.

Appendix

A Calculations

Expanded versions of the correlation factors are provided in this Appendix chapter. In addition, calculations needed to assess reasonable values HRRPUA and HRR time-evolution are shown.

A.1 The correlation factors

The correlation factors are shown in the methods chapter in compressed form only. Here, the correlation factors are expanded to clarify calculation procedure. Subscripts and variables are described in section 2.4.4 and 3.1. The functions of correlation factor 1, $\beta_{\theta,1}$, and 2, $\beta_{\theta,2}$, equation 3.6 and 3.10 respectively, are repeated for clarity:

$$\beta_{\theta,1} = \frac{\dot{m}_{\alpha,a}}{\dot{m}_{\alpha,b}}$$

and:

$$\beta_{\theta,2} = \frac{a_{\alpha,p,a}}{a_{\alpha,p,b}}$$

respectively. The mass production rate of species α, used to ascertain correlation factor 1, may be expressed in expanded form by combining eq. 3.4 and 3.5:

$$\dot{m}_{\alpha} = \frac{\gamma_{\alpha}\dot{Q}W_F}{\Delta H_{C,ox}W_{O_2}\left(x + \frac{y}{4} - \frac{z}{2} + W_F\left(\frac{\gamma_S}{W_S}\left(\frac{3X_H}{4} - 1\right) - \frac{\gamma_{CO}}{2W_{CO}}\right)\right)}$$

For correlation factor 1, little additional information and expressions are required, only mole weight data and expressions for the mole weights of soot and fuel. These may be expressed by (adapted from [17]):

$$W_S = X_H W_H + (1 - X_H)W_C \tag{A.1}$$

and:

$$W_F = xW_C + yW_H + zW_O + vW_N \tag{A.2}$$

respectively. Mole weight data is provided in Table A.1.

Table A.1 Mole weight data. Collected from [17].

Species and atoms	Mole weight [g/mol]
O_2	31.998800
N_2	28.013400
H_2O	18.015280
CO_2	44.009500
CO	28.010100
Soot ($C_{0,9}H_{0,1}$)	10.910420
C	12.0107
H	1.007940
N	14.006700
O	15.999400

Eq. 2.31 is used to ascertain correlation factor 2. In expanded form, eq. 2.31 may be expressed:

$$a_{\alpha,p} = \frac{\nu_{\alpha,p} W_\alpha}{\nu_{S,p} W_S + \nu_{N_2,p} W_{N_2} + \nu_{H_2O,p} W_{H_2O} + \nu_{CO_2,p} W_{CO_2} + \nu_{CO,p} W_{CO}}$$

The stoichiometric coefficient for species α may be solved through eq. 2.38 and by applying mole weights instead of mass terms (adapted from [17]):

$$\nu_{\alpha,p} = \frac{W_F}{W_\alpha} \gamma_\alpha \tag{A.3}$$

Balancing the chemical reaction in eq. 2.37, allows for solving the stoichiometric coefficients of the primitive species constituents of the products (adapted from [17]):

$$\nu_{CO_2,p} = x - \frac{W_F}{W_{CO}} \gamma_{CO} - (1 - X_H) \frac{W_F}{W_S} \gamma_S + \nu_{CO_2,a} \tag{A.4}$$

$$\nu_{H_2O,p} = \frac{y}{2} - \frac{X_H W_F}{2 W_S} \gamma_S + \nu_{H_2O,a} \tag{A.5}$$

$$\nu_{N_2,p} = \frac{v}{2} + \nu_{N_2,a} \tag{A.6}$$

Combining eq. A.3 through A.6, provides for a further expansion of eq. 2.31:

$$a_{\alpha,p} = \frac{\gamma_\alpha W_F}{\gamma_S W_F + \left(\frac{v}{2} + \nu_{N_2,a}\right) W_{N_2} + \left(\frac{y}{2} - \frac{X_H W_F}{2 W_S} \gamma_S + \nu_{H_2O,a}\right) W_{H_2O} + \left(x - \frac{W_F}{W_{CO}} \gamma_{CO} - (1 - X_H) \frac{W_F}{W_S} \gamma_S + \nu_{CO_2,a}\right) W_{CO_2} + \gamma_{CO} W_F}$$

By use of the fuel parameters provided in Table 3.5, the correlation factors for both soot and CO mass quantities may now be calculated. The results of the calculations are provided in Table 4.1.

A.2 Supplementary calculations to determine HRRPUA and HRR evolution

To determine the HRRPUA and the method of emulating the αt^2-fires, the fire Froude number (eq. 2.20) and flame height (eq. 2.21) relative to ceiling height are assessed. References to these procedures are made in section 3.2.2.

The fire Froude number and ceiling height are expressed in relation to the fire diameter, D. Equations are sought where these parameters are expressed in terms of HRRPUA and HRR instead. The fire surface area, A, and diameter are related by:

$$A = \frac{\pi}{4} D^2 \tag{A.7}$$

Setting $A = \frac{\dot{Q}}{\dot{Q}''}$, and solving for D, the fire Froude number and flame height may be expressed in terms of HRRPUA and HRR by:

$$\dot{Q}^* = \frac{\dot{Q}}{\rho_\infty c_p T_\infty \sqrt{g}} \left(\frac{4\dot{Q}}{\pi \dot{Q}''} \right)^{-5/4} \tag{A.8}$$

and:

$$L_f = \sqrt{\frac{4\dot{Q}}{\pi \dot{Q}''}} \left(3{,}7 (\dot{Q}^*)^{\frac{2}{5}} - 1{,}02\right) \tag{A.9}$$

respectively. Calculating the fire Froude number, ambient values of $\rho_\infty = 1{,}204\ kg/m^3$ [33] and $T_\infty = 293\ K$ [17] are applied. For the specific heat and gravitational acceleration, values of $1{,}006\ kJ/kgK$ [34] and $9{,}81\ m/s^2$ [17] are used.

In Figure A.1, the values of the fire Froude numbers and flame height (both vertical axis) above the fire VENT (0,5 m above the floor) are shown. These are plotted against values of HRRPUA (horizontal axis), for the values of HRR selected for simulation in this study. A value of approximately unity is sought for the fire Froude number, as this is characteristic for accidental fires [19]. Additionally, it is preferred to reduce flame impingement on the ceilings, due to the possibilities of reduced oxygen entrainment to the flame. The ceiling height is 2,4 and 5,0 m for Model A and B respectively. Finally, a single value of HRRPUA is preferred for all simulations. With these considerations combined, a value of 1000 kW/m^2 is deemed appropriate. This value allows for both limited flame impingement while still ascertaining a fire Froude number not far from unity (0,4-0,6).

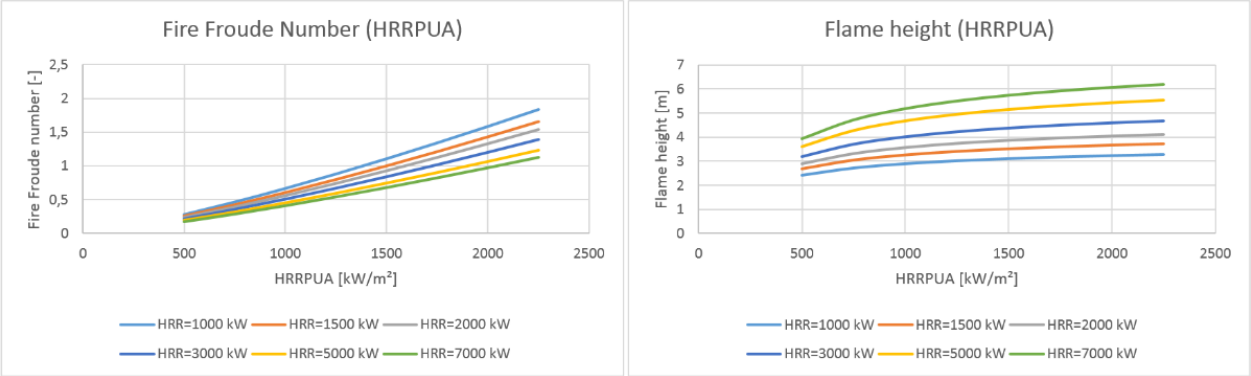

Figure A.1 Fire Froude numbers (left) and flame height above fire VENT (right) for different values of HRR and HRRPUA.

As to the growth rates, two different methods of specifying time evolution of HRR in FDS are considered. The first being the time ramp of HRRPUA. This keeps the fire area constant but evolves the HRR in time by increasing HRRPUA. The second method is to assert radially spreading fires, the spread rate of which is repeated below for clarity (eq. 3.13) [25]:

$$v_f = \sqrt{\frac{\alpha}{\pi \dot{Q}''}}$$

As this is the radial velocity, the fire diameter increases by twice the spread rate in [m/s]. As such, the diameter may be described as a function of the spread rate, v_f, by:

$$D = t \cdot 2\sqrt{\frac{\alpha}{\pi \dot{Q}''}} \tag{A.10}$$

where t represents the evolution in time. Since the diameter increases linearly with time, the area increases exponentially (considering eq. A.7). With a constant HRRPUA, this emulates the αt^2-fire.

To assess these methods, the fire Froude numbers and flame heights are again evaluated. For the first method, the fire Froude number-expression (eq. 2.20) can be applied with only slight adjustments. The expression for HRR in the numerator is only substituted with the expression the αt^2-fire of eq. 2.8, resulting in:

$$\dot{Q}^*(t) = \frac{\alpha t^2}{\rho_\infty c_p T_\infty \sqrt{gD} D^2} \tag{A.11}$$

The equation for the flame height (eq. 2.21) needs no further alterations. Two constant values of the diameter are applied to check the corresponding value of the fire Froude number and flame height. These are 1,13 and 1,59 m, corresponding to a VENT area of 1 m^2 and 2 m^2 respectively. These VENT areas are approximate to the ones applied for most simulations using Model A, where growing fires are applied (see Table 3.2).

For the second method, i.e. applying the radially spreading fire, the diameter in the expression for the fire Froude number is substituted with eq. A.10, resulting in:

$$\dot{Q}^*(t) = \frac{\alpha t^2}{\rho_\infty c_p T_\infty \sqrt{g}} \left(t \cdot 2\sqrt{\frac{\alpha}{\pi \dot{Q}''}} \right)^{-5/2} \tag{A.12}$$

Similarly, the diameter in the expression for the flame height is substituted with eq. A.10, resulting in:

$$L_f(t) = t \cdot 2\sqrt{\frac{\alpha}{\pi \dot{Q}''}} (3{,}7(\dot{Q}^*)^{\frac{2}{5}} - 1{,}02) \tag{A.13}$$

where eq. A.12 is applied as input for $\dot{Q}^*$.

The medium- (blue) and fast (red) -growing fires are applied as input to the fire Froude number and flame height in Figure A.2 and Figure A.3 respectively. These are plotted against time (horizontal axis), with a scale representing the simulation time applied for the growing fires (200 s). Dotted lines show the evolutions using a constant diameter and a time ramp of HRRPUA (eq. A.11 and eq. 2.21). The left and right plots apply diameters of 1,13 and 1,59 m respectively, corresponding to a VENT area of 1 m^2 and 2 m^2. For the solid lines, the HRRPUA is constant at 1000 kW/m^2 and HRR evolves as a function of increasing diameter (eq. A.12 and A.13). No other values of HRRPUA are applied, as this value is previously determined (elaborated above Figure A.1).

The radially spreading fire allows for a value of the fire Froude number somewhat closer to unity than the time ramped HRRPUA (Figure A.2). Thereby, the radially spreading fire is preferred, considering the fire Froude number. As to the flame height, it is preferred that the height is mostly below 2,4 (ceiling height of Model A is 2,4 m). This is not completely satisfied for either methods of emulating fire growth. However, for areas of 2 m^2 (diameters of 1,59 m), the radially spreading fire results in a slightly more favorable flame height (right plot of Figure A.3). As such, the radially spreading fire (eq. 3.13) is considered the most suitable to emulate the αt^2-fire in this study.

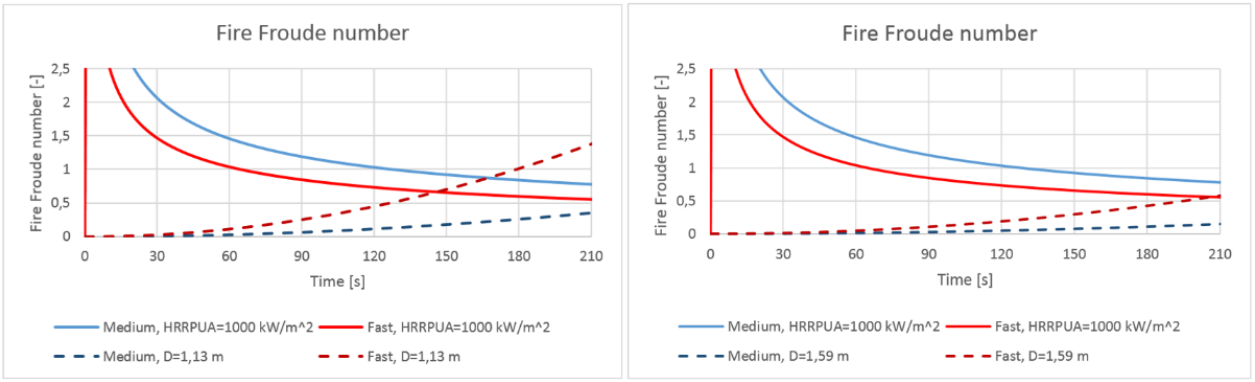

Figure A.2 Time evolution of the fire Froude number for fast (red) and medium growth (blue) rates. Dotted lines are representing the application of constant diameters. The continuous lines use constant HRRPUA.

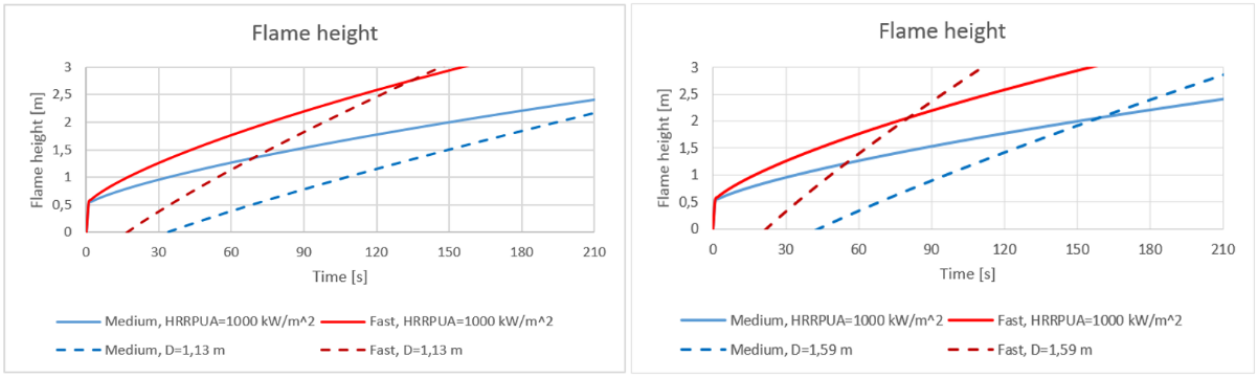

Figure A.3 Time evolution of flame height for fast (red) and medium growth (blue) rates. Dotted lines are representing the application of constant diameters. The continuous lines use constant HRRPUA.

B Additional results

In the results chapter (chapter 4), most plots depict results from the statistical mean values of soot density. This is due to the ratios of estimation to simulation generally being the same, independently of the measured quantity or the form of statistical output. The remaining measurements, the maximum soot densities, and mean and maximum CO mass fractions, are provided in Appendix B.1 through B.3. As all results are time averaged, Appendix B.4 provide selections of representative time history plots of the estimated and simulated mean soot densities. Notice should be taken as to terms applied in the plot-names. For instance, the left plot of Figure B.1 is named "Avg. soot density - estimated/simulated - medium HRR growth". The term "Avg." (or average) refers to *time* averaging of the plotted variable (see section 3.4.2), and must not be confused with the *volume* averaging, or statistical volumetric mean values.

B.1 Maximum soot densities

Differentiating HRR, Model geometry and position of measurement

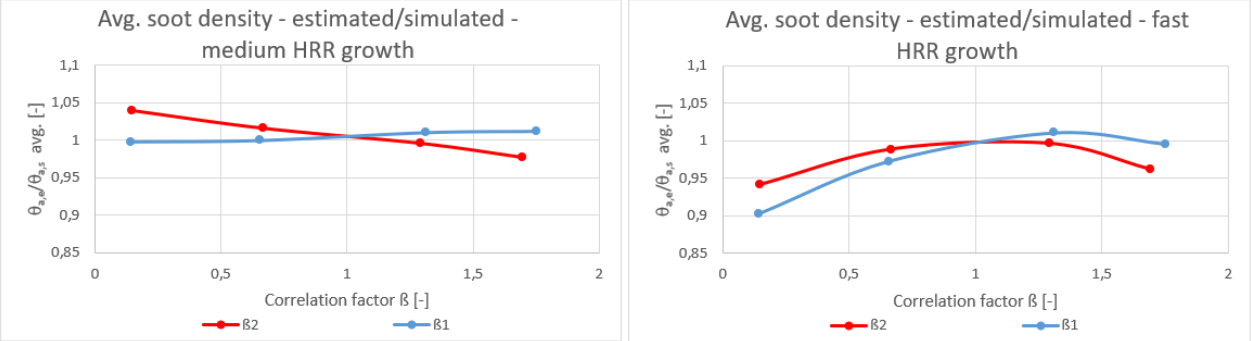

Figure B.1 Model A, growing HRRs. Simulation series from left: 1, 2.

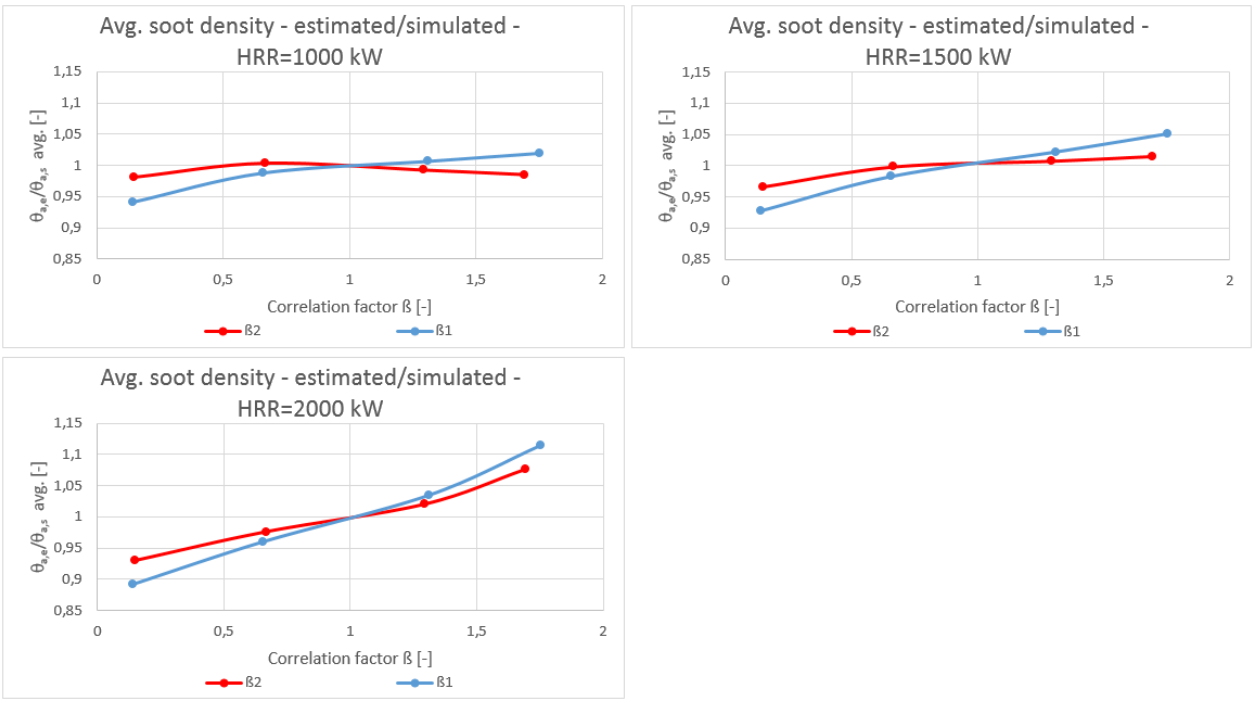

Figure B.2 Model A, constant HRR. Simulation series from upper left: 3, 4, 5.

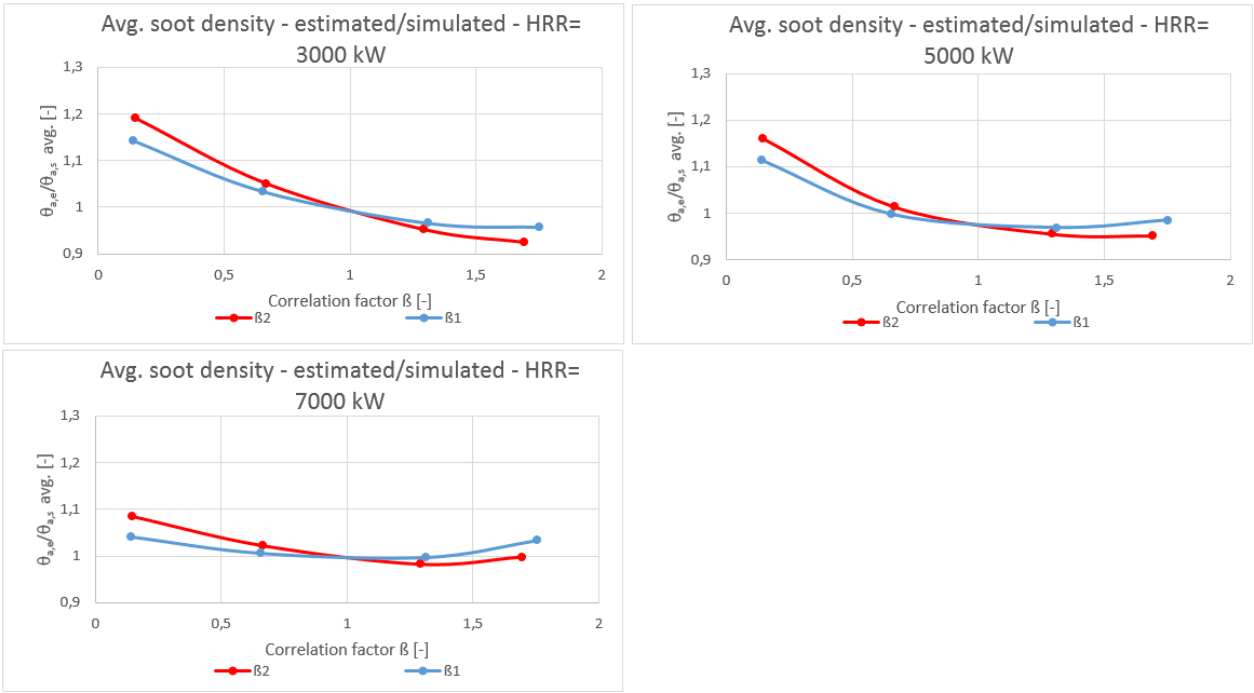

Figure B.3 Model B, measurement position I. Simulation series and position of measurements from upper left: 16, 17, 18.

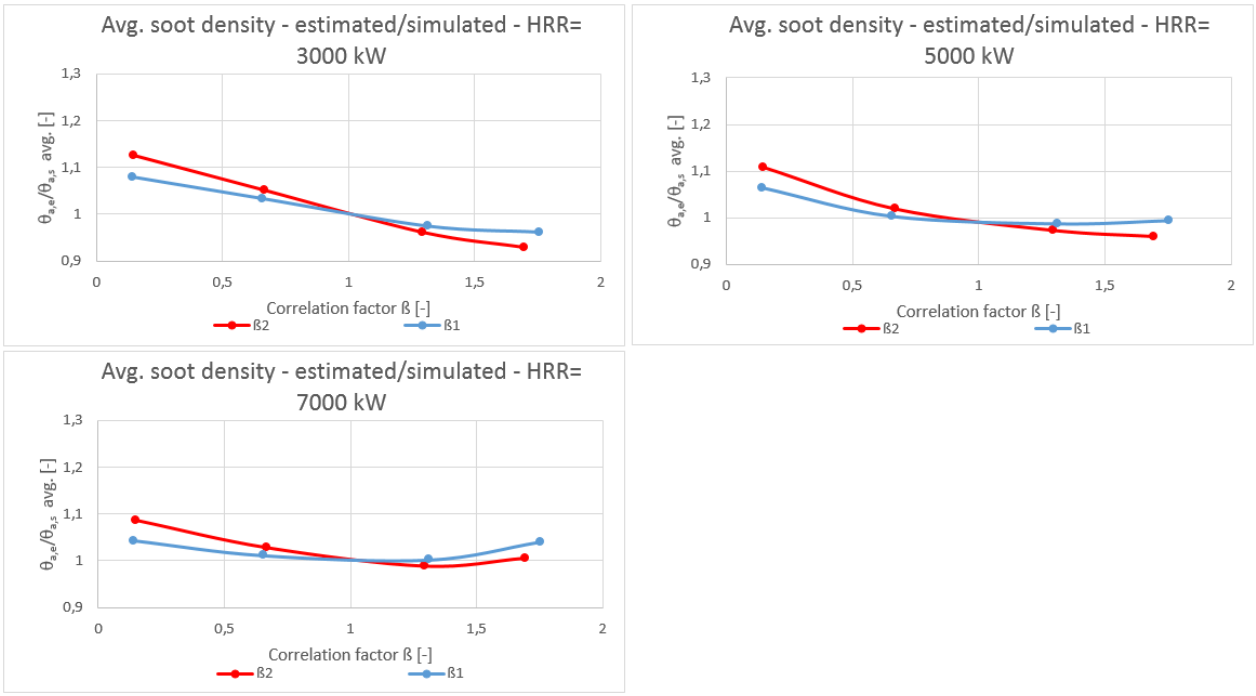

Figure B.4 Model B, measurement position II. Simulation series and position of measurements from upper left: 16, 17, 18.

Differentiating transport mechanisms and soot deposition

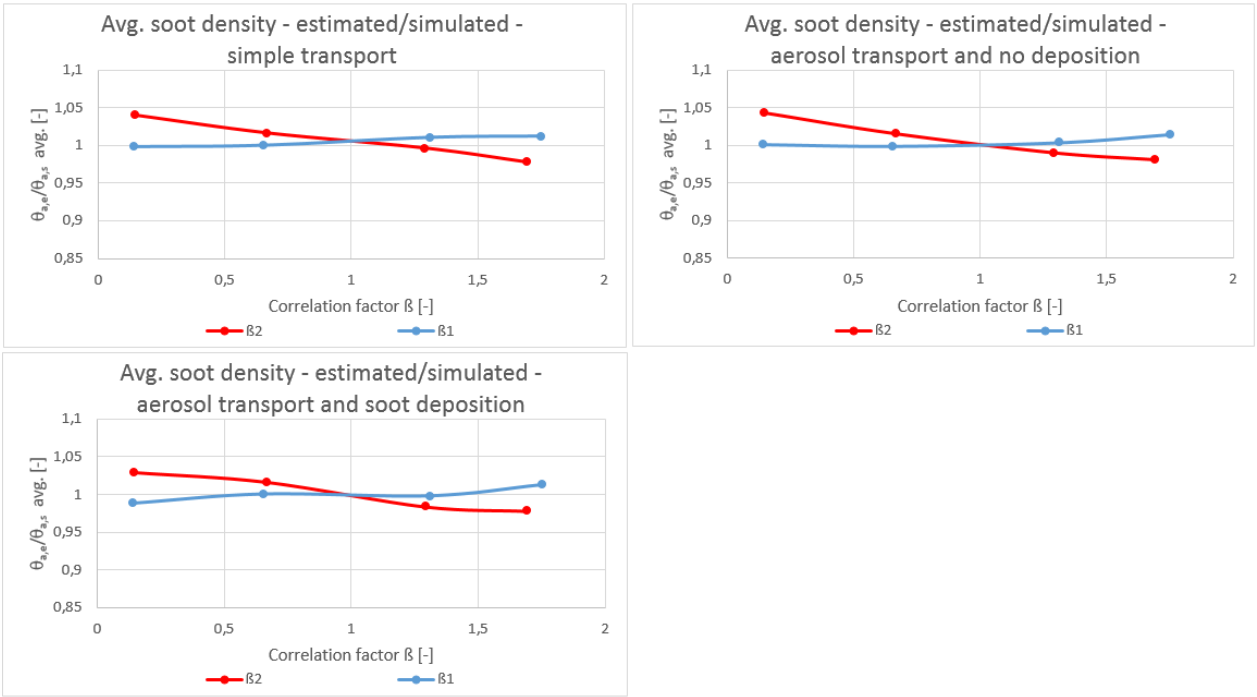

Figure B.5 Model A, medium HRR growth. Simulation series from upper left: 1, 6, 7.

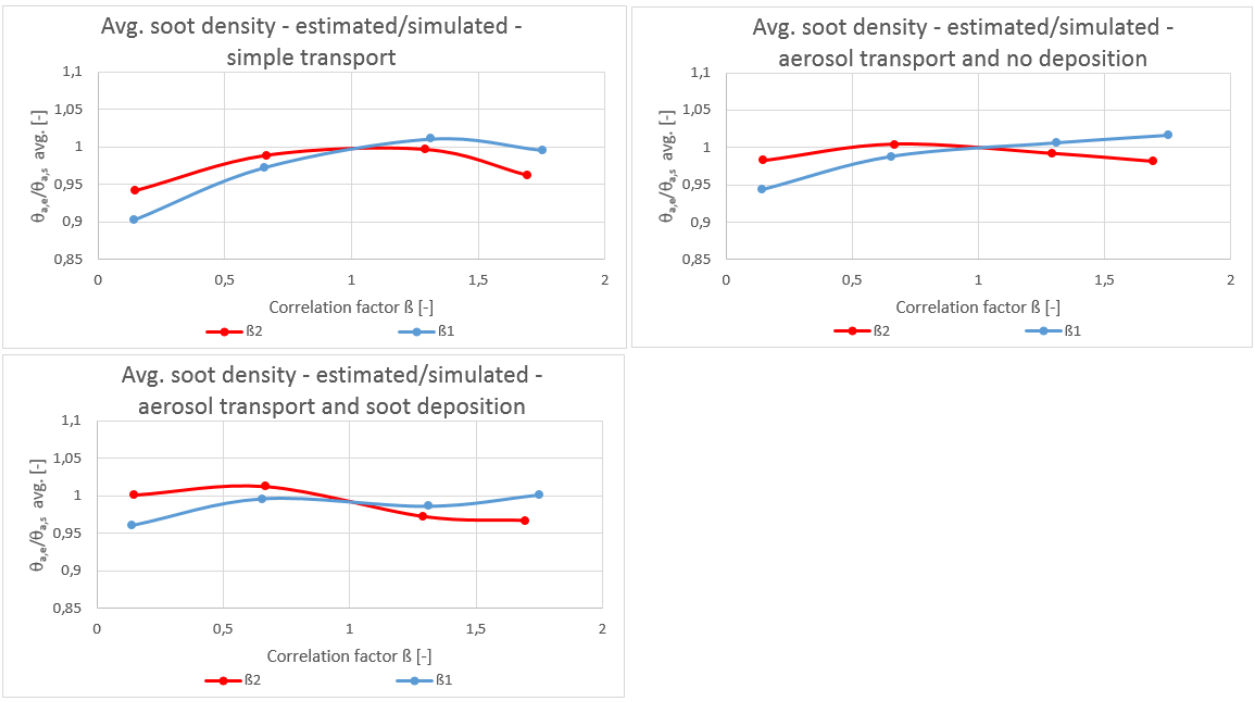

Figure B.6 Model A, fast HRR growth. Simulation series from upper left: 2, 8, 9.

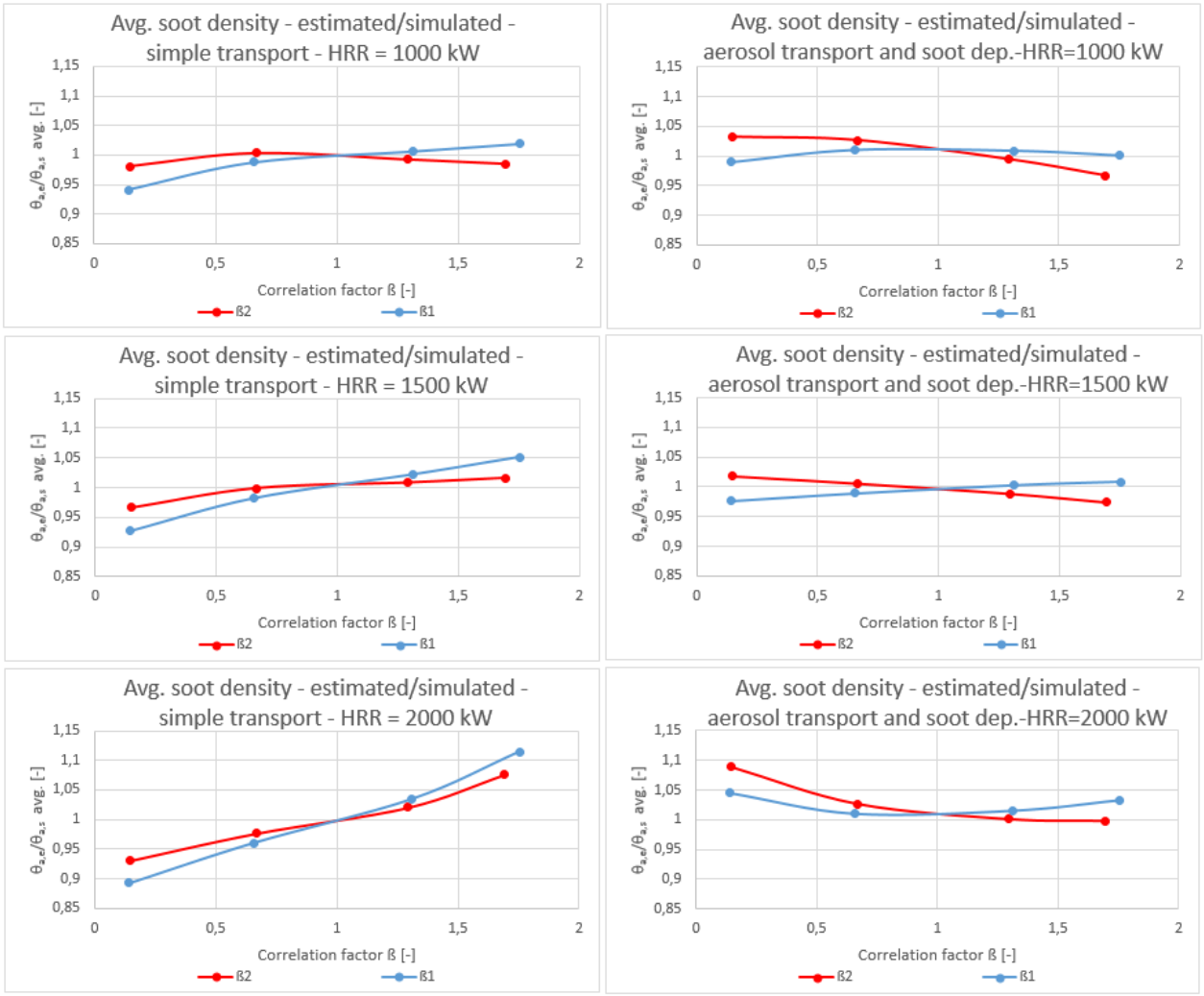

Figure B.7Model A, constant HRR. Simulation series from upper left: 3, 10, 4, 11, 5, 12.

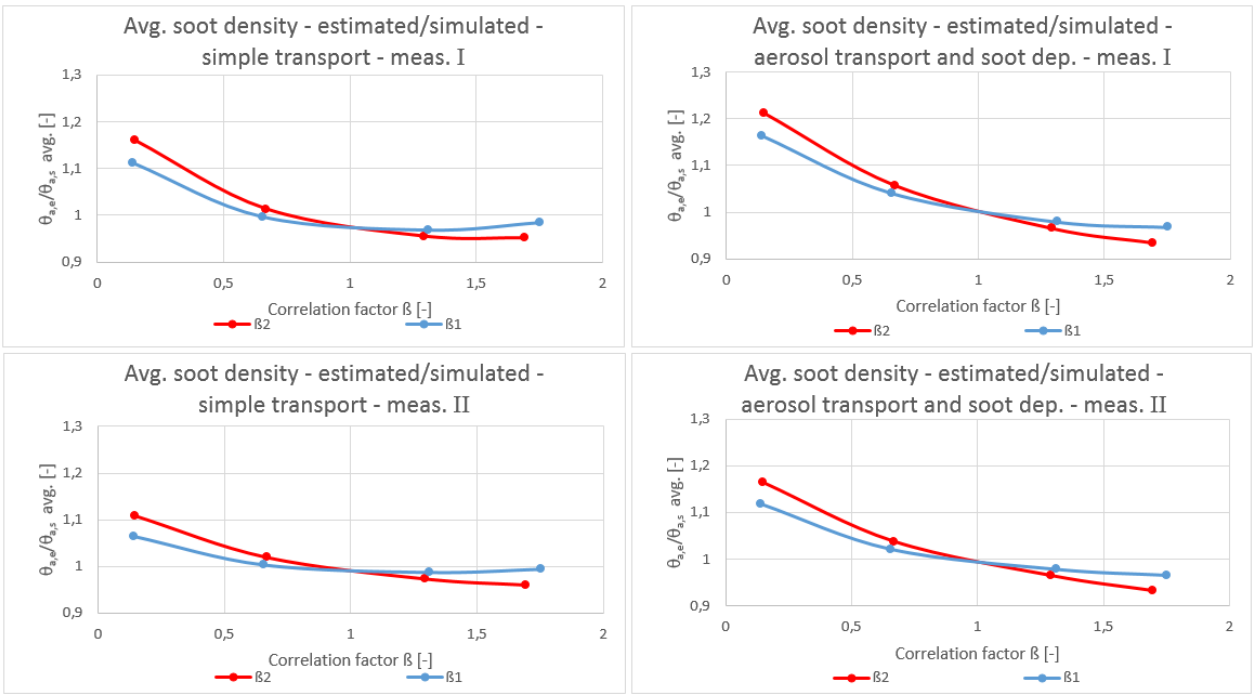

Figure B.8 Model B. Simulation series and position of measurements from upper left: 17-I, 19-I, 17-II, 19-II.

Differentiating miscellaneous fuel-type variations

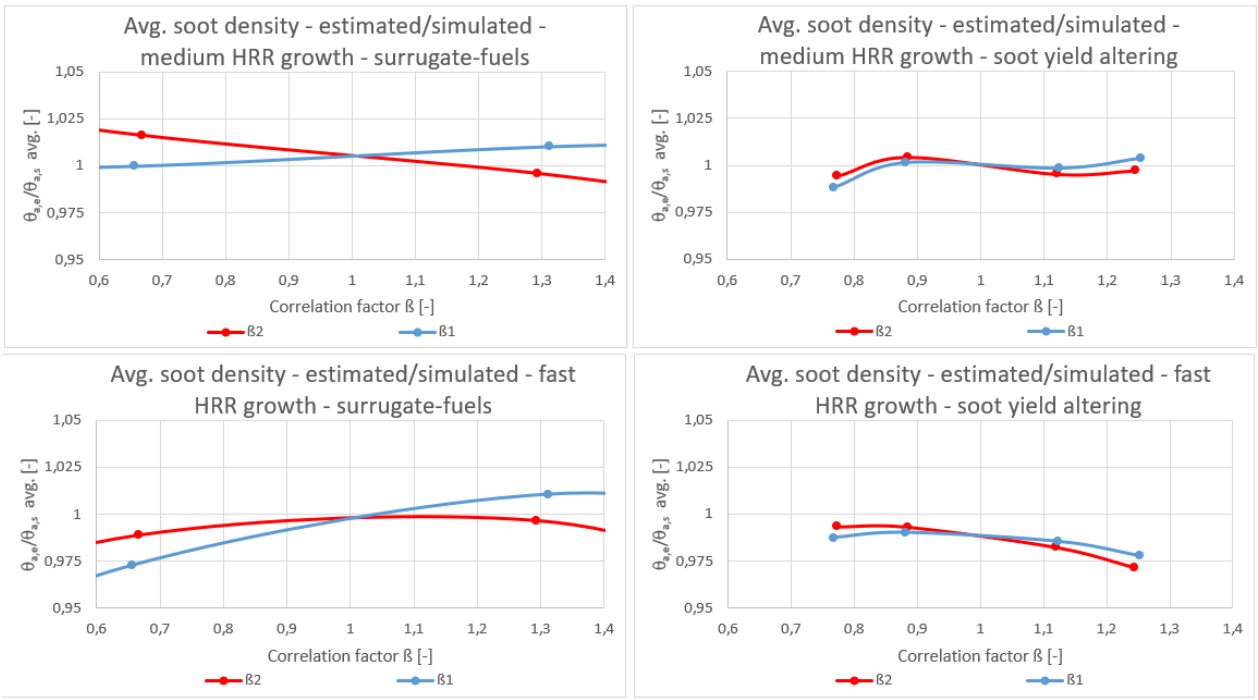

Figure B.9 Model A, surrogate-fuels compared to fuels where only soot yield is altered. Series from upper left: 1, 13, 2, 14.

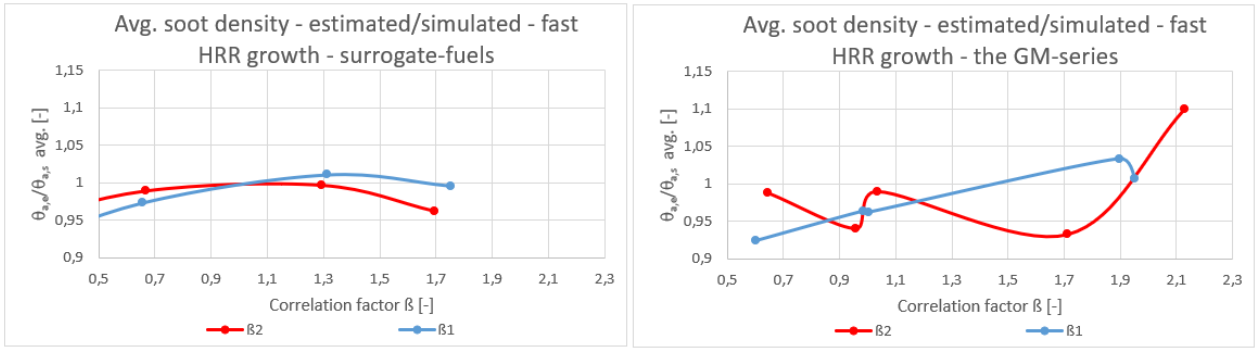

Figure B.10 Model A, surrogate-fuel series 2 (left) and the GM-series 15 (right).

B.2 Mean CO mass fractions

Differentiating HRR, Model geometry and position of measurement

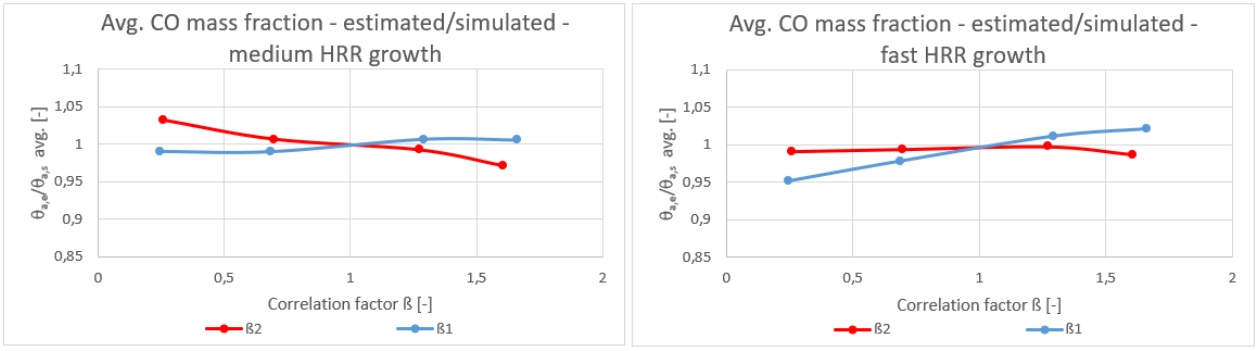

Figure B.11 Model A, growing HRRs. Simulation series from left: 1, 2.

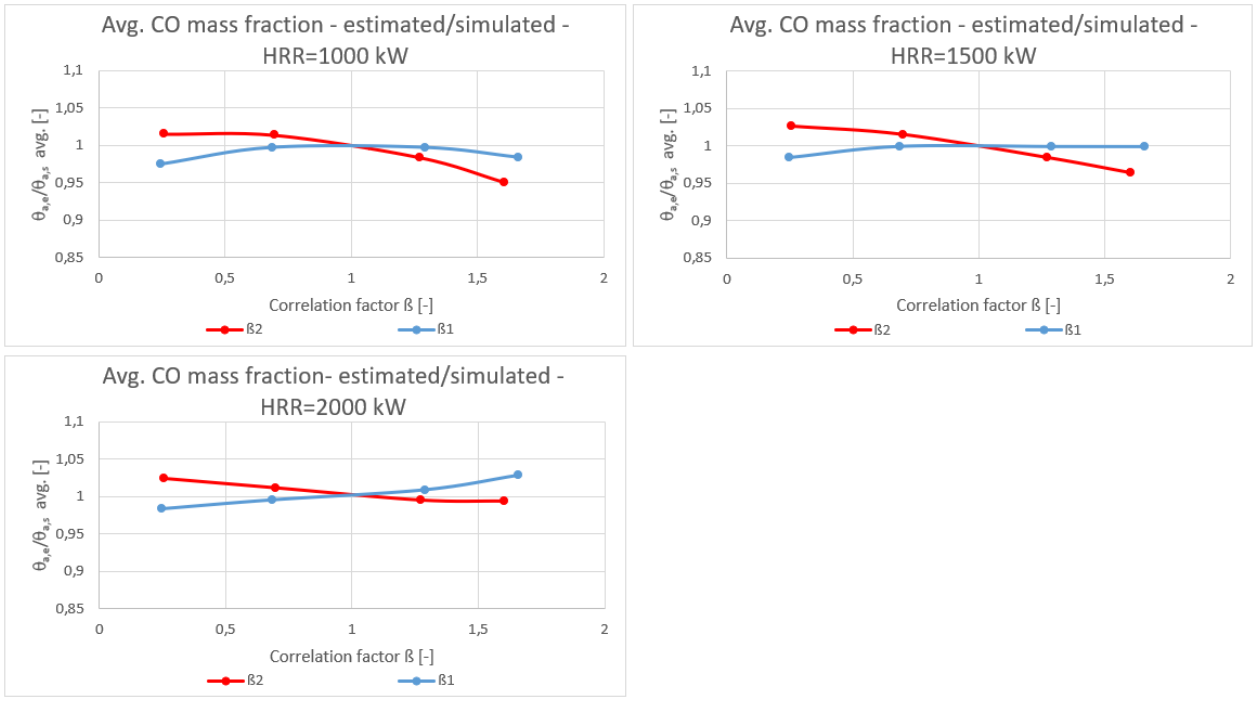

Figure B.12 Model A, constant HRR. Simulation series from upper left: 3, 4, 5.

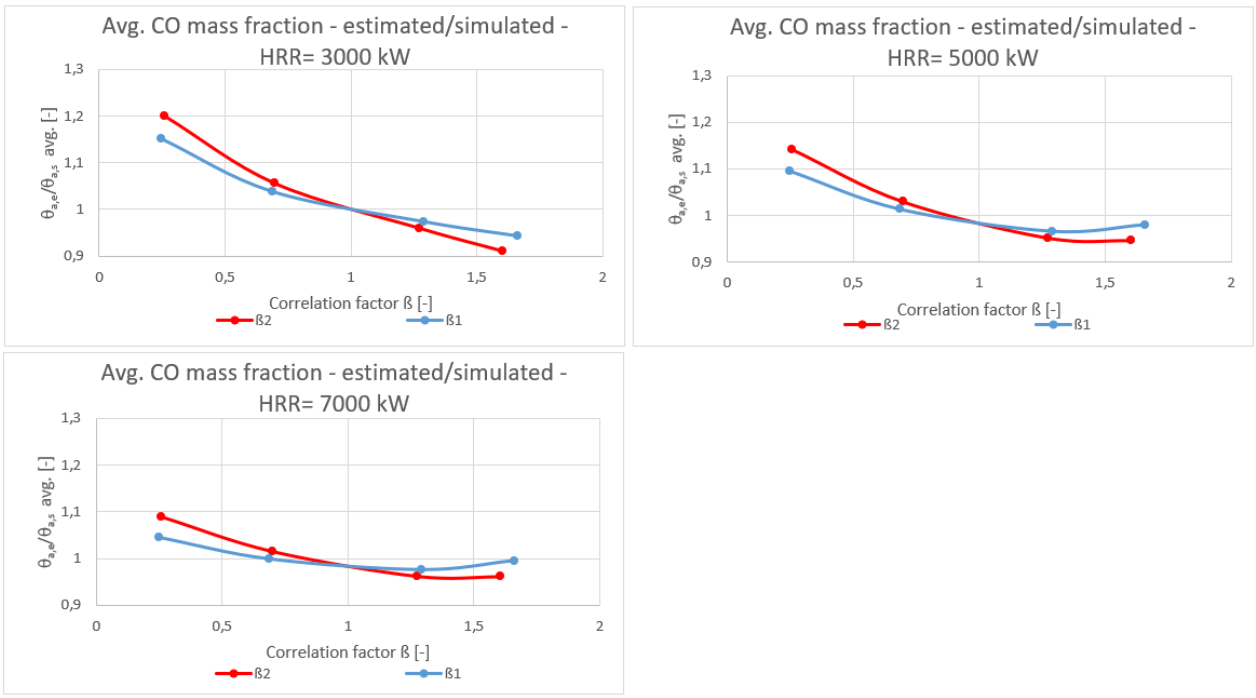

Figure B.13 Model B, measurement position I. Simulation series and position of measurements from upper left: 16, 17, 18.

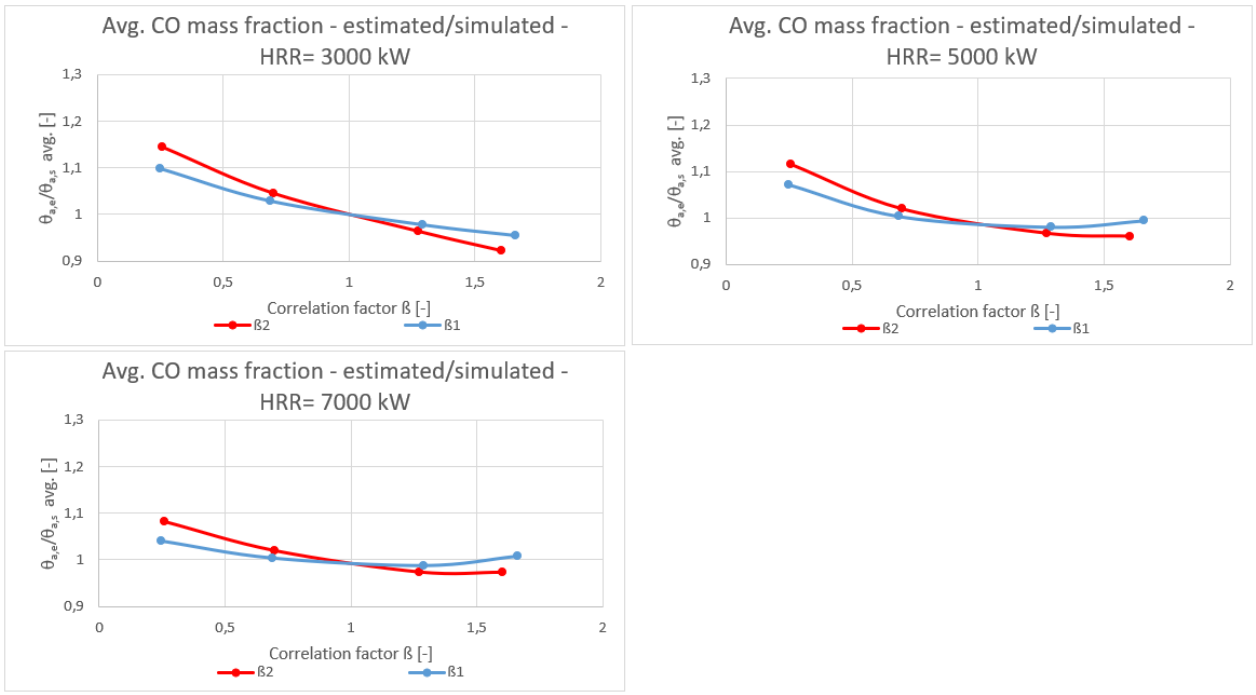

Figure B.14 Model B, measurement position I. Simulation series and position of measurements from upper left: 16, 17, 18.

Differentiating transport mechanisms and soot deposition

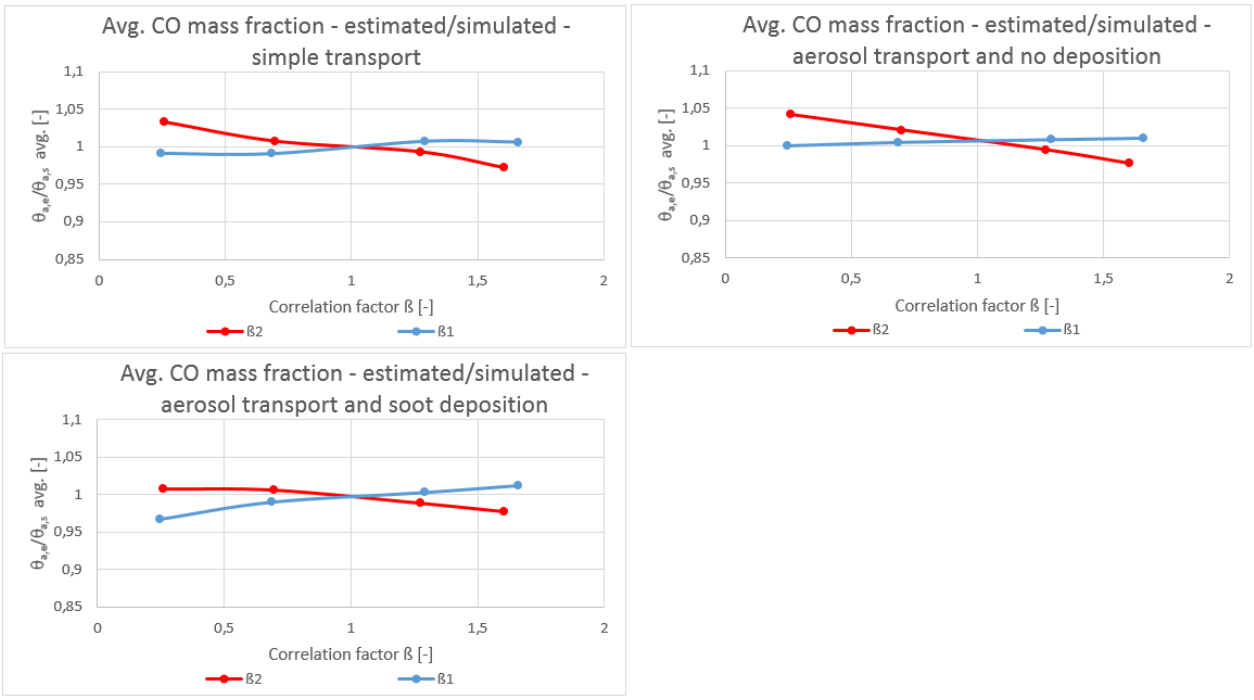

Figure B.15 Model A, medium HRR growth. Simulation series from upper left: 1, 6, 7.

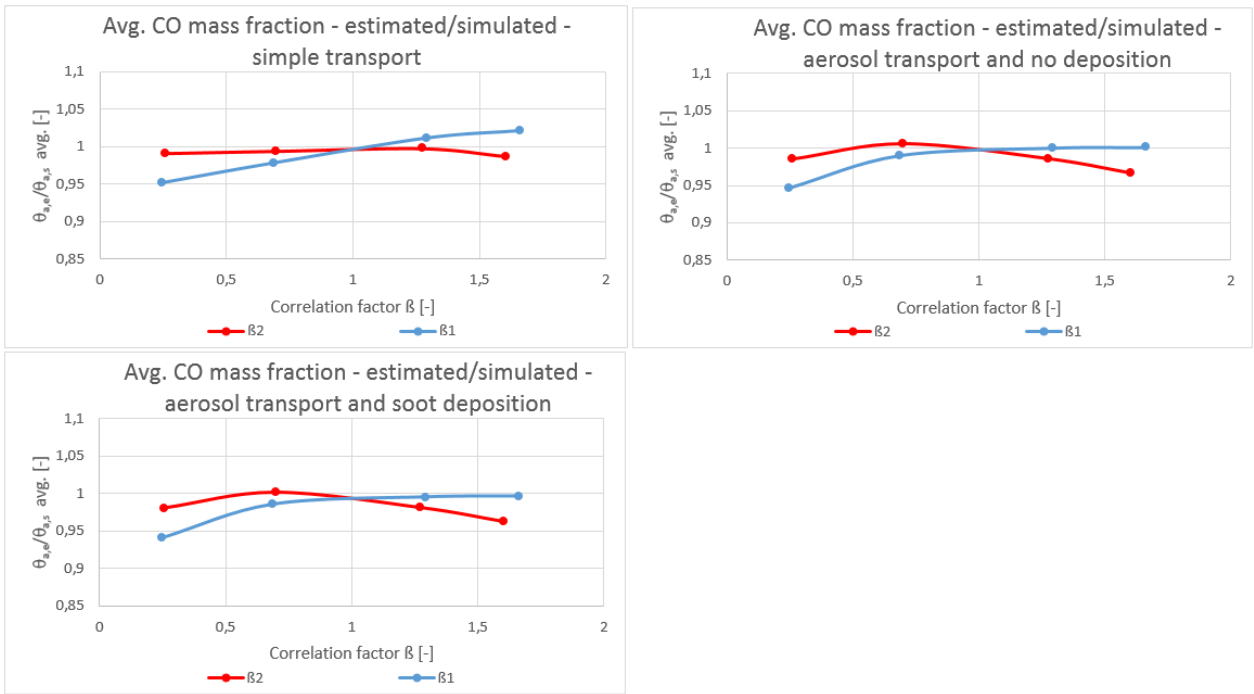

Figure B.16 Model A, fast HRR growth. Simulation series from upper left: 2, 8, 9.

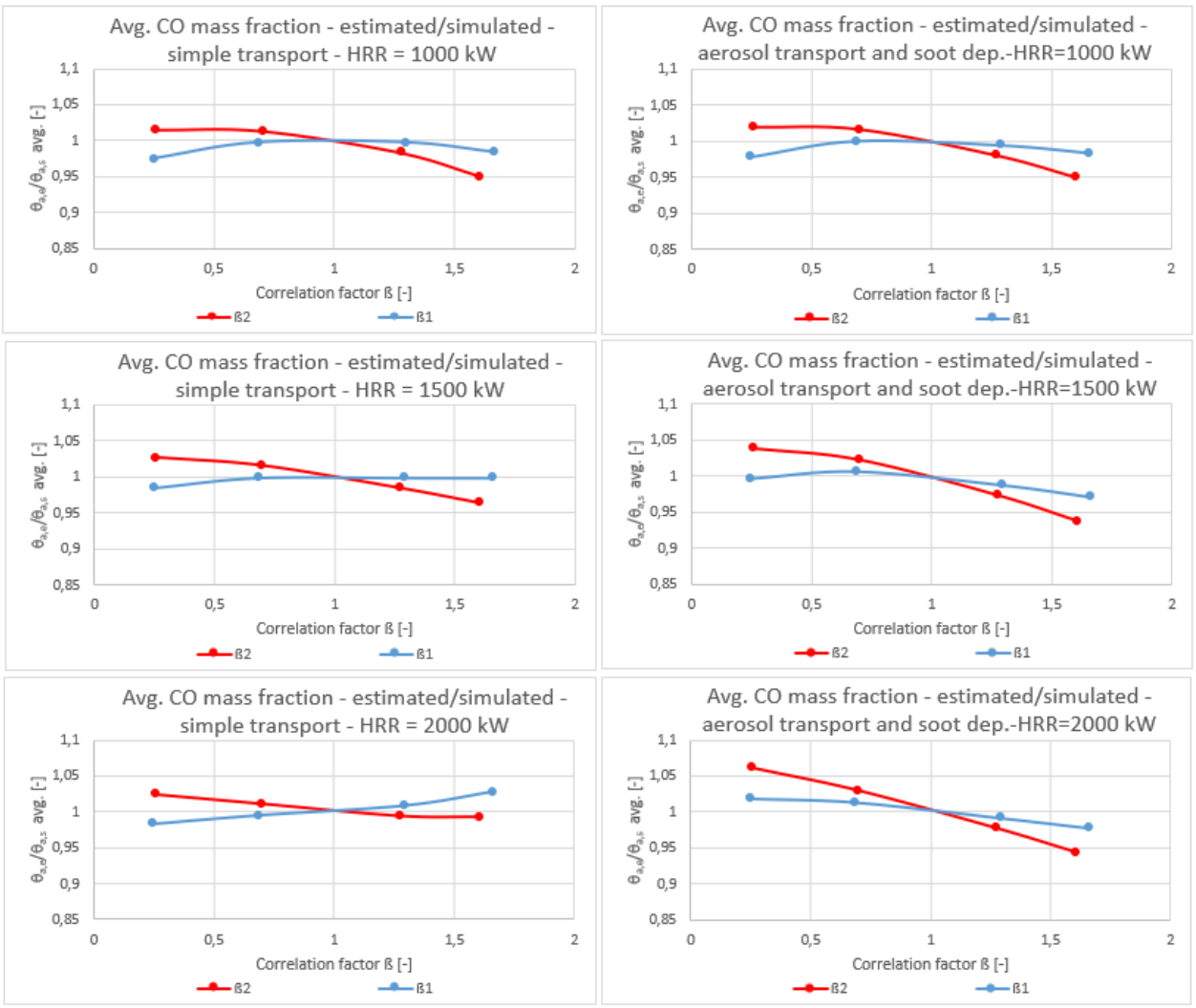

Figure B.17 Model A, constant HRR. Simulation series from upper left: 3, 10, 4, 11, 5, 12.

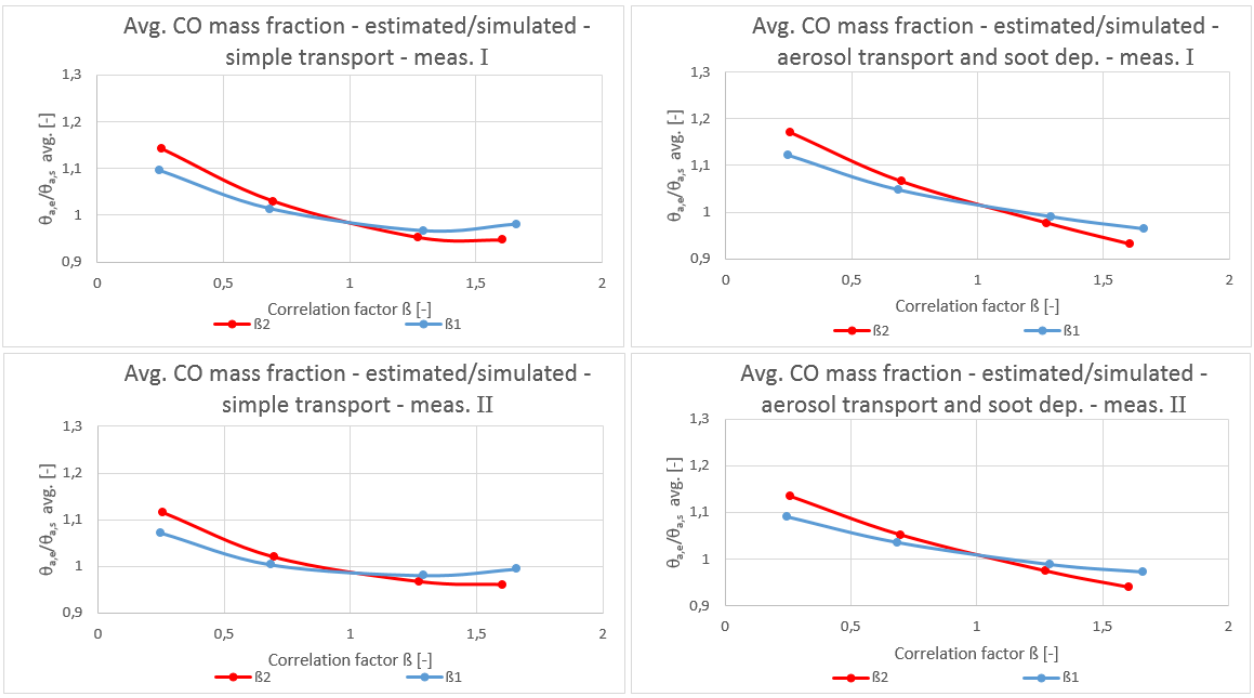

Figure B.18 Model B. Simulation series and position of measurements from upper left: 17-I, 19-I, 17-II, 19-II.

Differentiating miscellaneous fuel-type variations

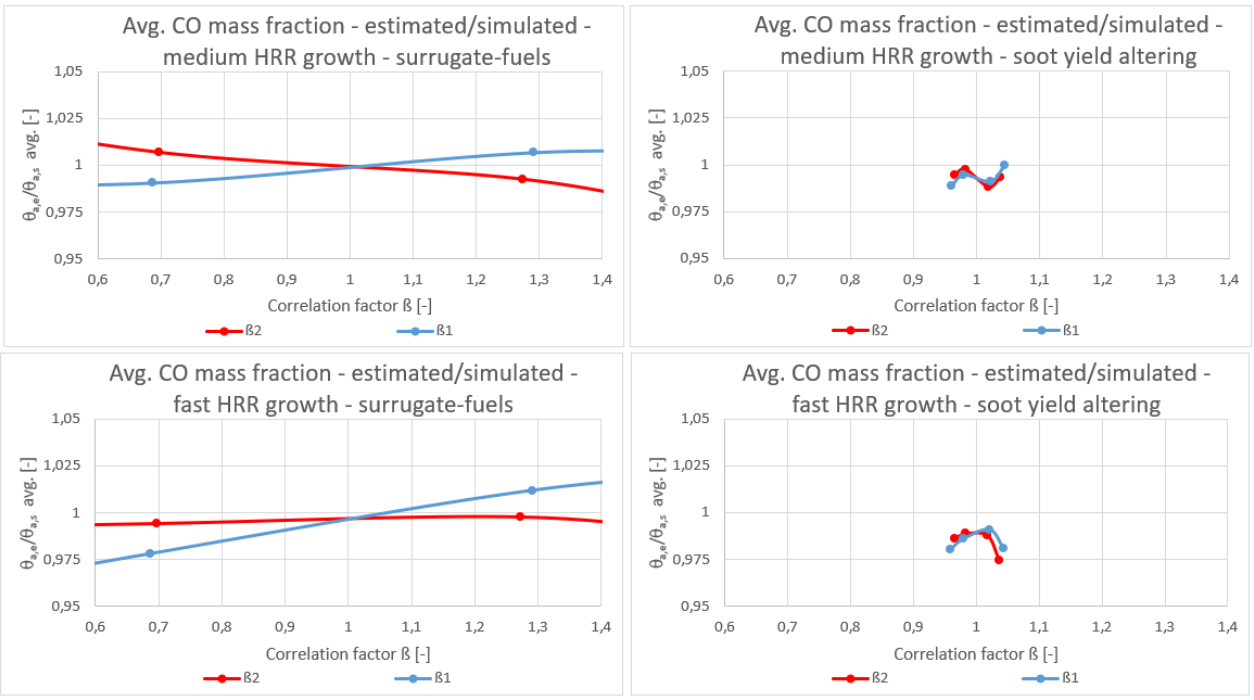

Figure B.19 Model A, surrogate-fuels compared to fuels where only soot yield is altered. Series from upper left: 1, 13, 2, 14.

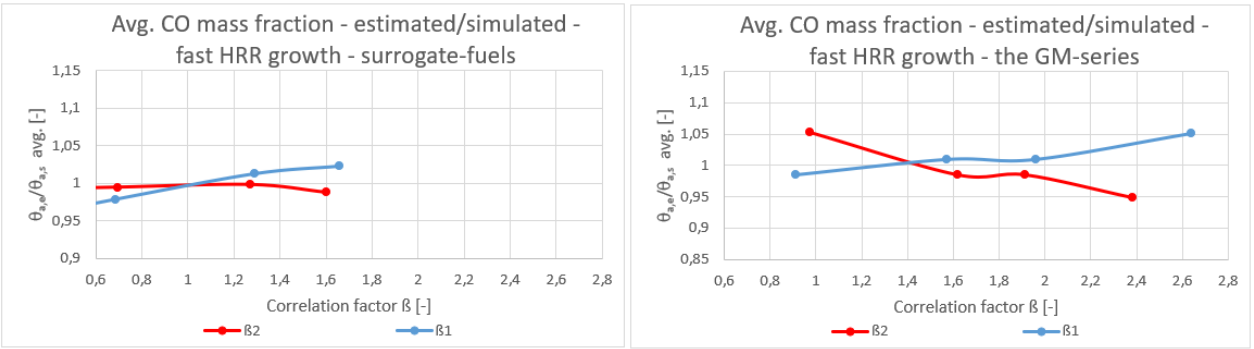

Figure B.20 Model A, surrogate-fuel series 2 (left) and the GM-series 15 (right).

B.3 Maximum CO mass fractions

Differentiating HRR, Model geometry and position of measurement

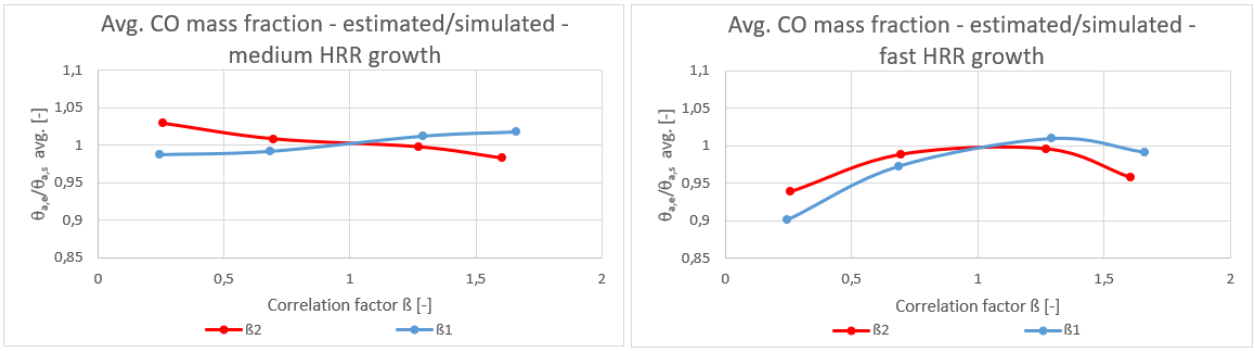

Figure B.21 Model A, growing HRRs. Simulation series from left: 1, 2.

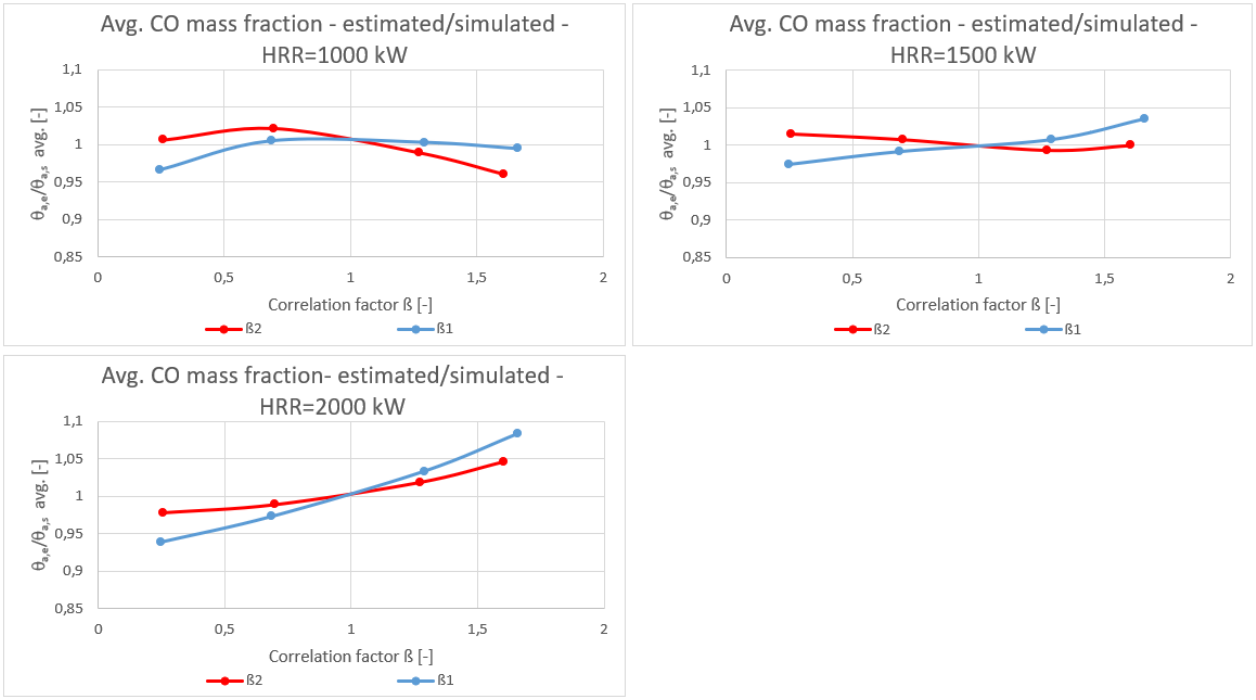

Figure B.22 Model A, constant HRR. Simulation series from upper left: 3, 4, 5.

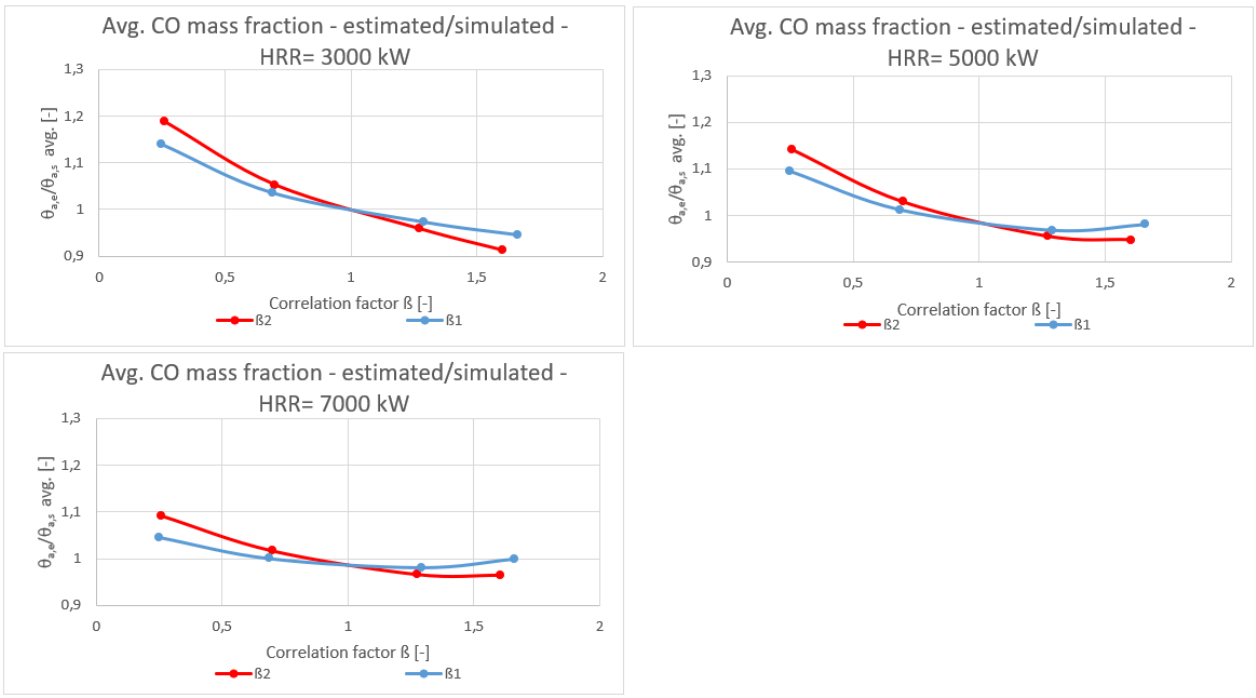

Figure B.23 Model B, measurement position I. Simulation series and position of measurements from upper left: 16, 17, 18.

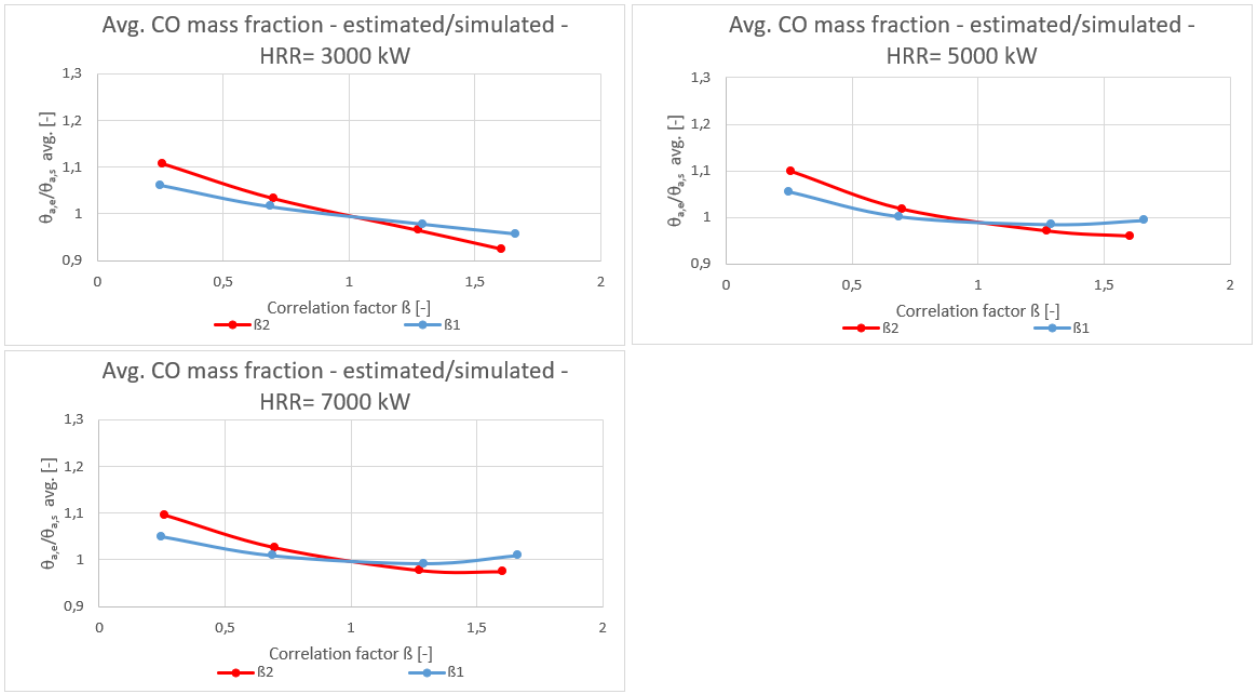

Figure B.24 Model B, measurement position II. Simulation series and position of measurements from upper left: 16, 17, 18.

Differentiating transport mechanisms and soot deposition

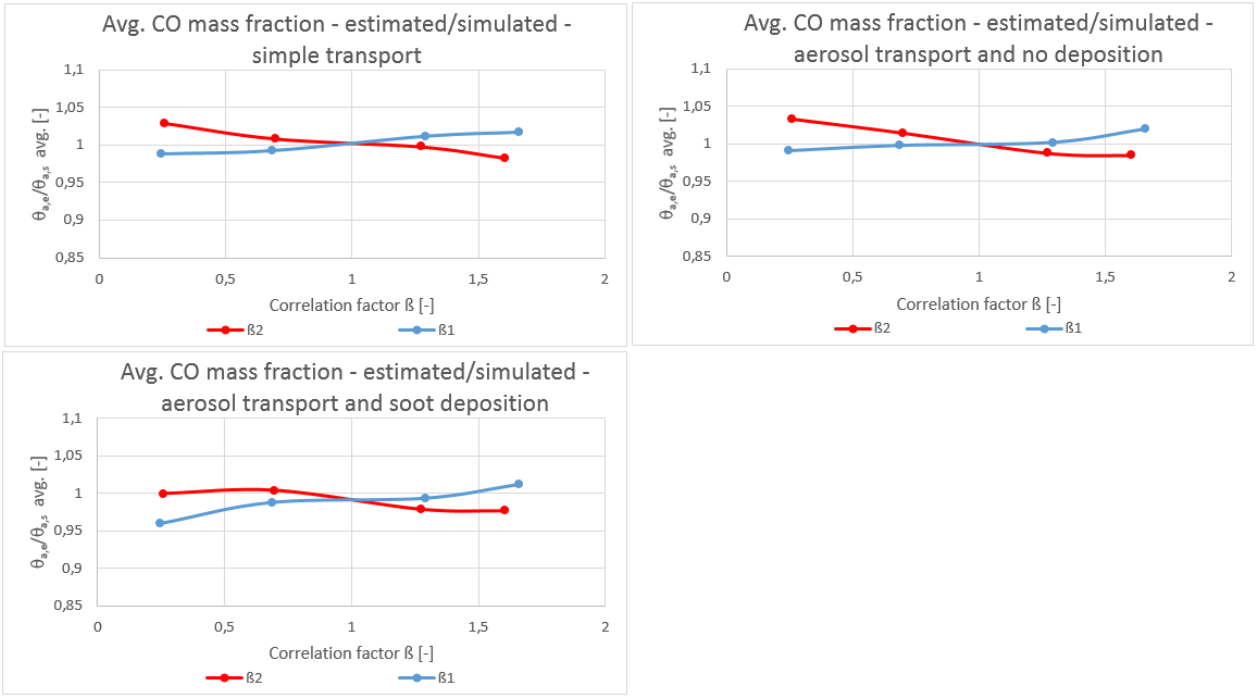

Figure B.25 Model A, medium HRR growth. Simulation series from upper left: 1, 6, 7.

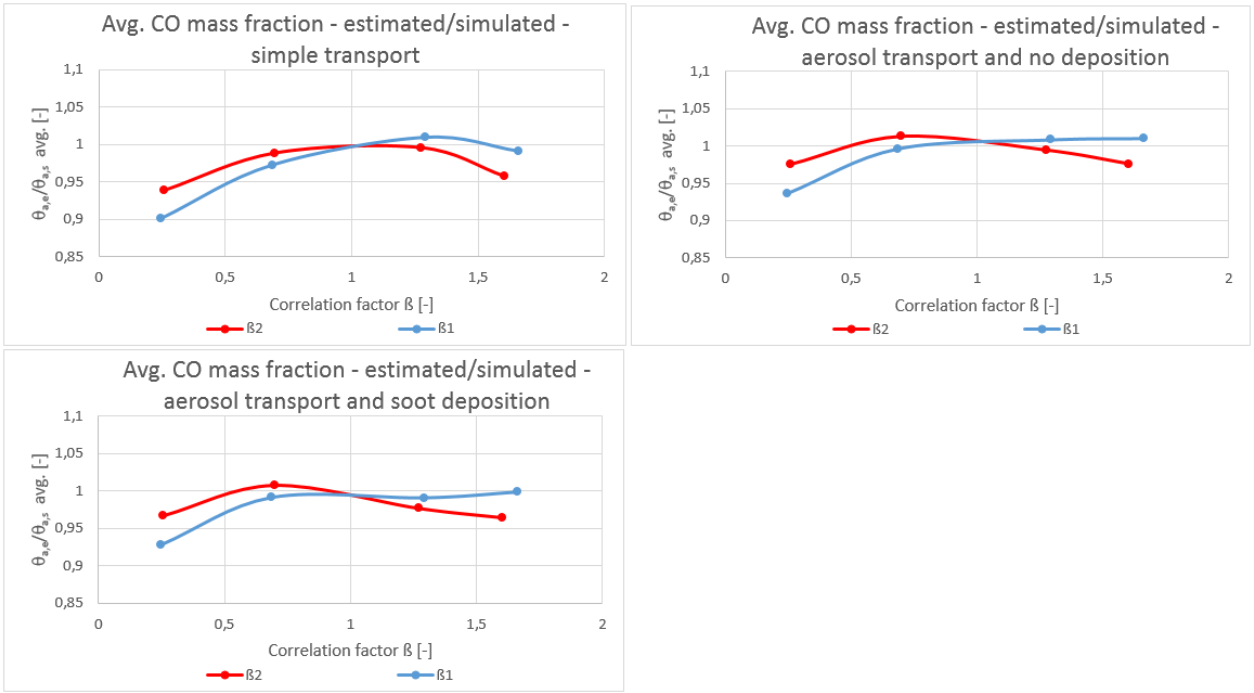

Figure B.26 Model A, fast HRR growth. Simulation series from upper left: 2, 8, 9.

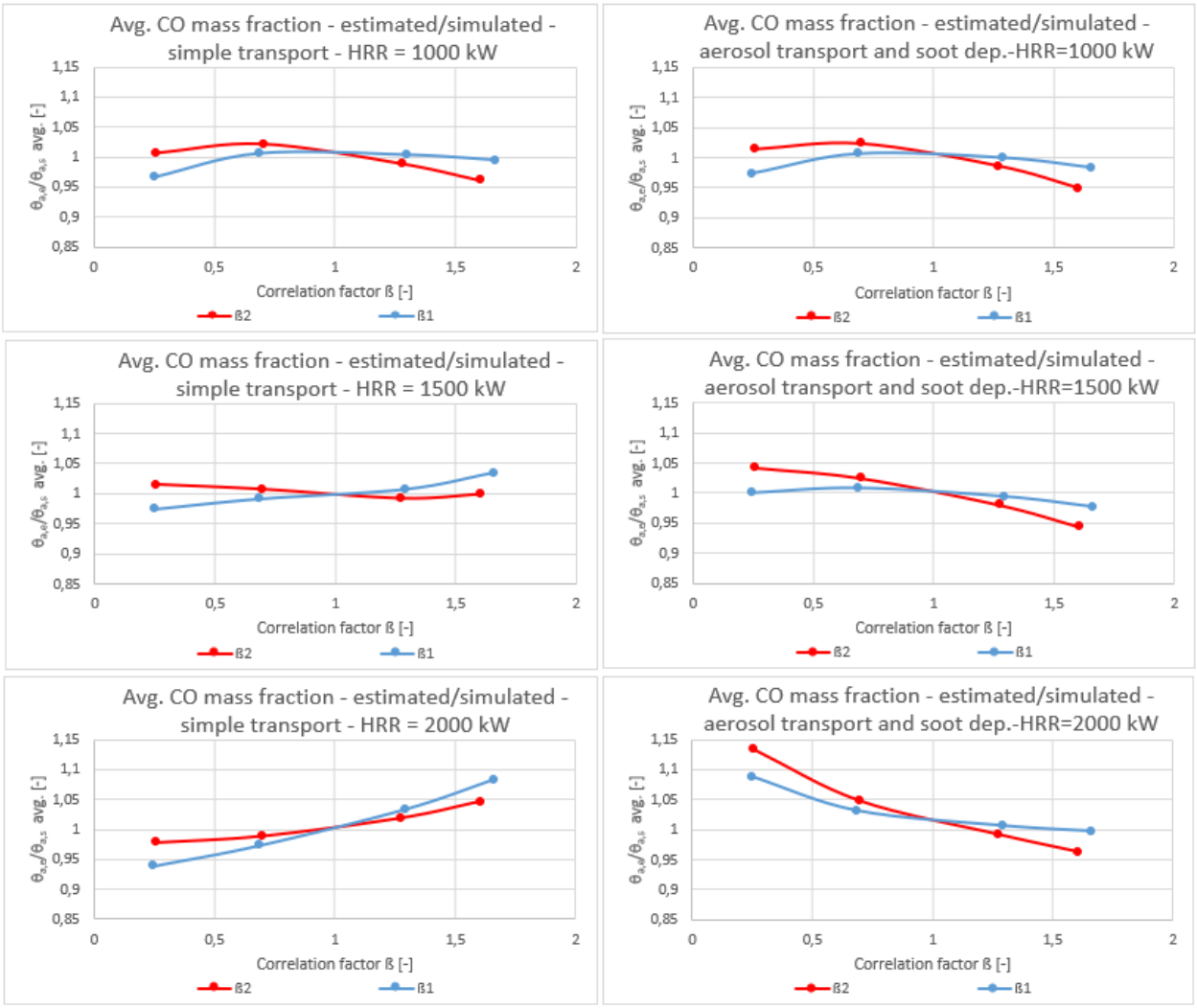

Figure B.27Model A, constant HRR. Simulation series from upper left: 3, 10, 4, 11, 5, 12.

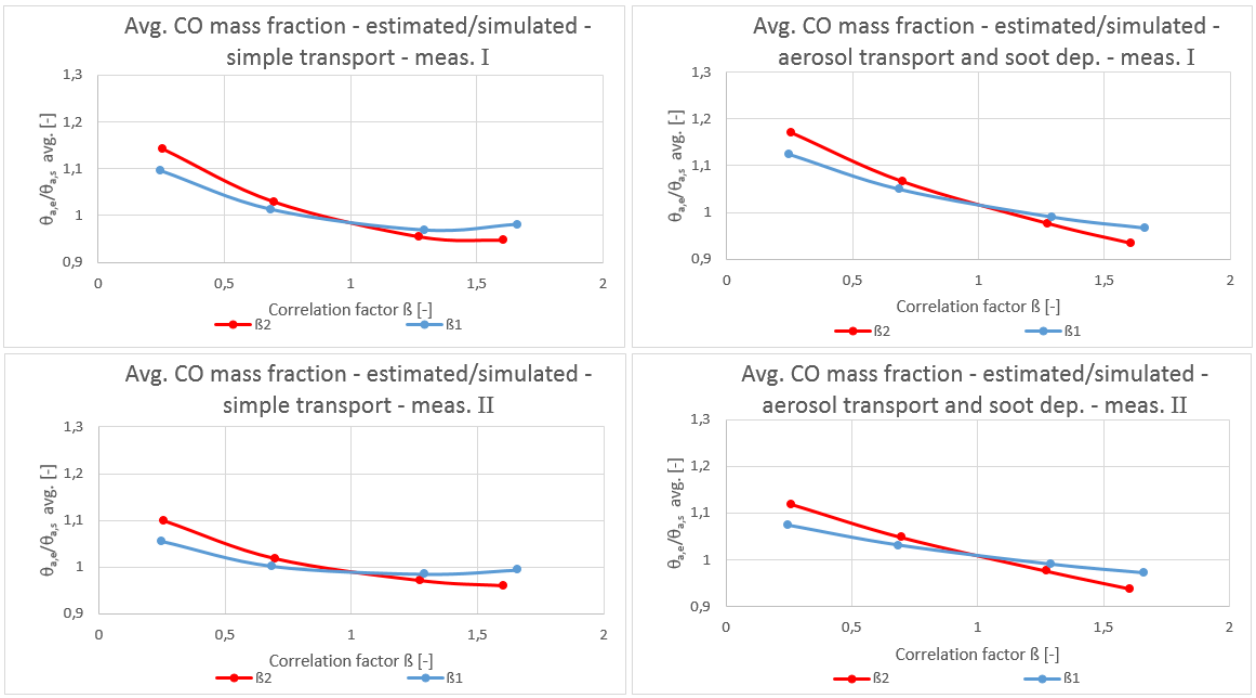

Figure B.28 Model B. Simulation series and position of measurements from upper left: 17-I, 19-I, 17-II, 19-II.

Differentiating miscellaneous fuel-type variations

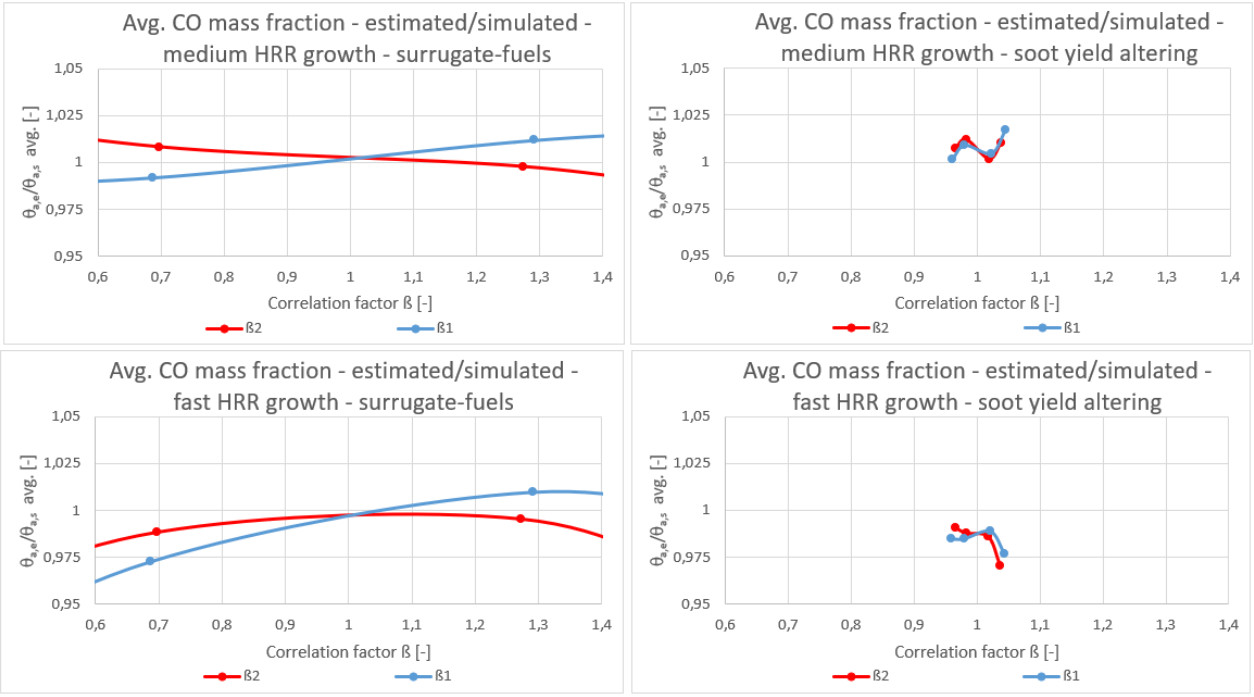

Figure B.29 Model A, surrogate-fuels compared to fuels where only soot yield is altered. Series from upper left: 1, 13, 2, 14.

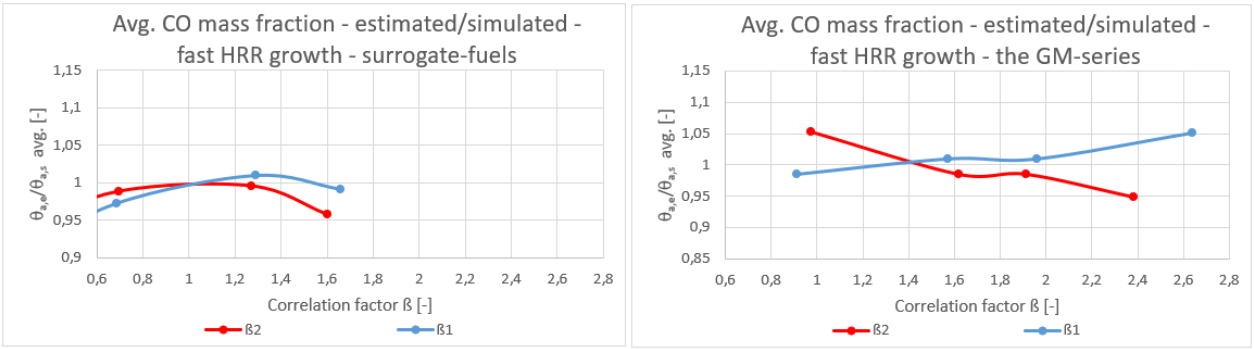

Figure B.30 Model A, surrogate-fuel series 2 (left) and the GM-series 15 (right).

B.4 Recorded time histories

Results in this study are mostly based on time averaged ratios of estimation to simulation. As such, a selection of time histories representative for the estimation discrepancies are shown in this Appendix. All figures show plots of estimated time histories (dotted lines) and simulated time histories (solid lines). The time histories are of the statistical volumetric mean soot densities. Plotted simulation time histories are referred to by simulation fuel parameter indexes (see Table 3.6 through Table 3.9). Estimated simulation results are additionally referred to by "E". All plotted estimations are generated through use of correlation factor 1 and the results from the base simulation (indexed 5 in each series).

The time history plots in Figure B.31 show results from simulation series 1 and 2, using medium and fast HRR-growth respectively, and Model A. Ratios of time averaged estimations to simulations plotted against correlation factor-values are provided in Figure 4.8. The ratios are time averaged from t=120 s to 200 s for the medium HRR-growth and from t=90 s to 200 s for the fast HRR-growth.

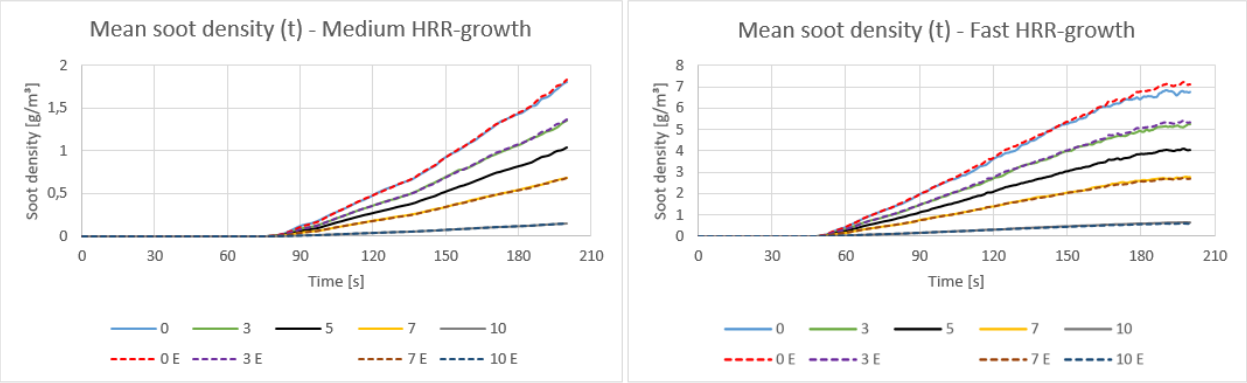

Figure B.31 Time histories of estimated and simulated values of statistical mean soot density. Series applied from left: 1, 2.

The time history plots in Figure B.32 show results from simulation series 3, 4, 5, using HRRs of 1000, 1500 and 2000 kW respectevely, and Model A. Ratios of time averaged estimations to simulations plotted against correlation factor-values are provided in Figure 4.9. The ratios are time averaged from t=400 s to 600 s.

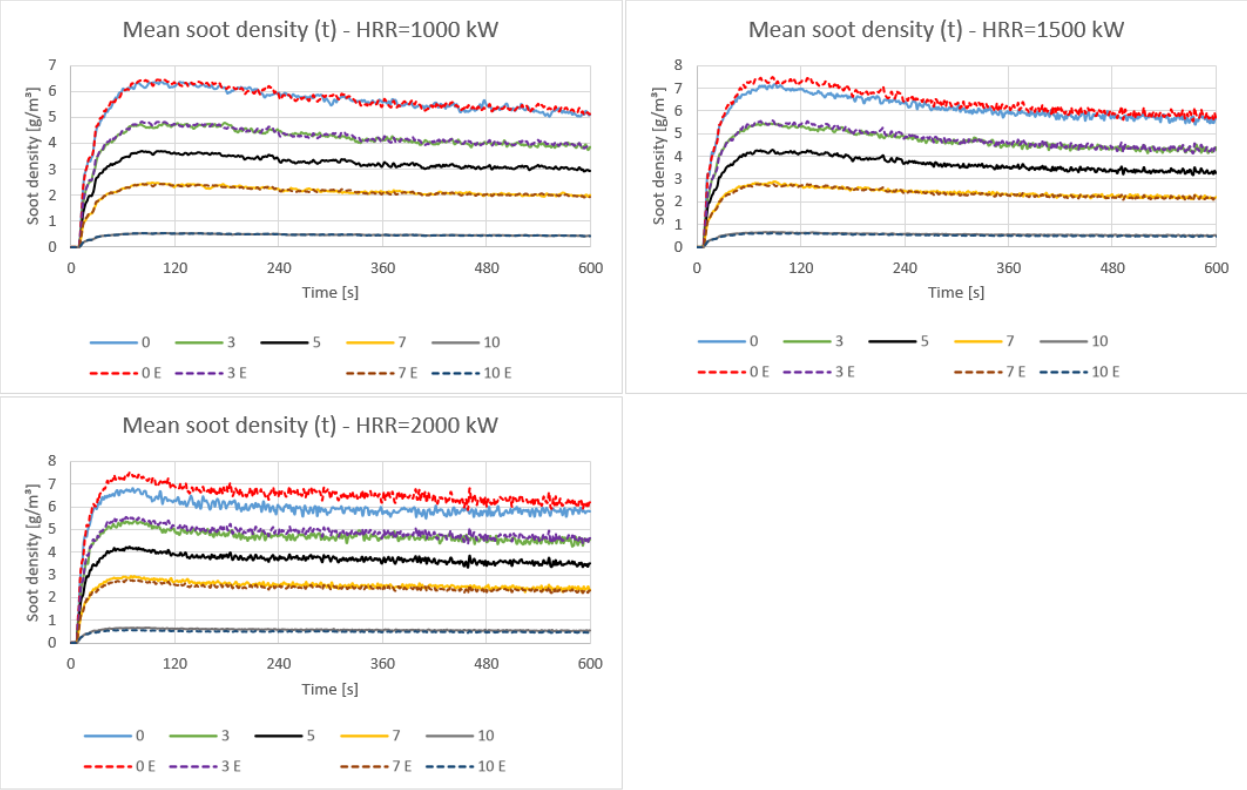

Figure B.32 Time histories of estimated and simulated values of statistical mean soot density. Series applied from upper left: 3, 4, 5.

The time history plots in Figure B.33 show results from simulation series 6, 7, 8 and 9. The two former and the two latter using medium and fast HRR-growths respectively, and Model A. The left and right columns show results when soot deposition is disabled and enabled respectively. Ratios of time averaged estimations to simulations plotted against correlation factor-values are provided in Figure 4.12 and Figure 4.13. The ratios are time averaged from t=120 s to 200 s for medium HRR-growth, and from t=90 s to 200 s for fast HRR-growth.

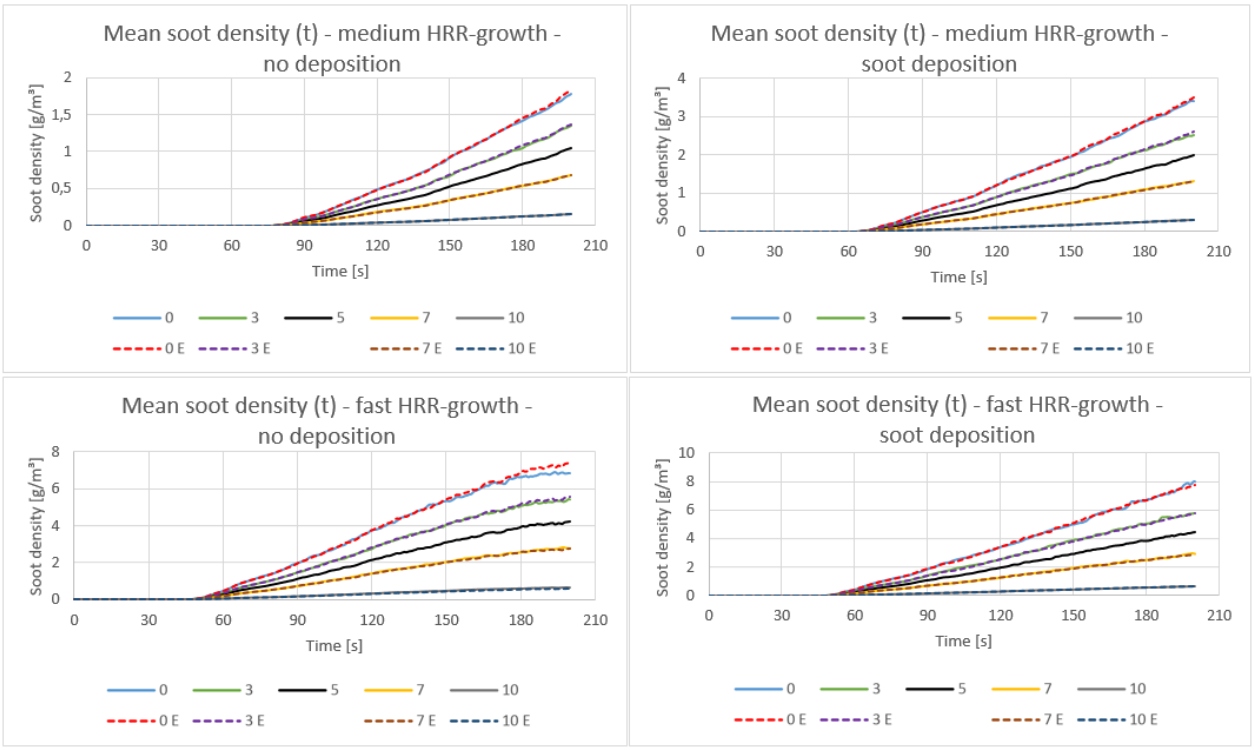

Figure B.33 Time histories of estimated and simulated values of statistical mean soot density. Series applied from upper left: 6, 7, 8, 9.

The time history plots in Figure B.34 show results from simulation series 10, 11, 12, using HRRs of 1000, 1500 and 2000 kW respectevely, Model A and soot deposition enabled. Ratios of time averaged estimations to simulations plotted against correlation factor-values are provided in Figure 4.14. The ratios are time averaged from t=400 s to 600 s.

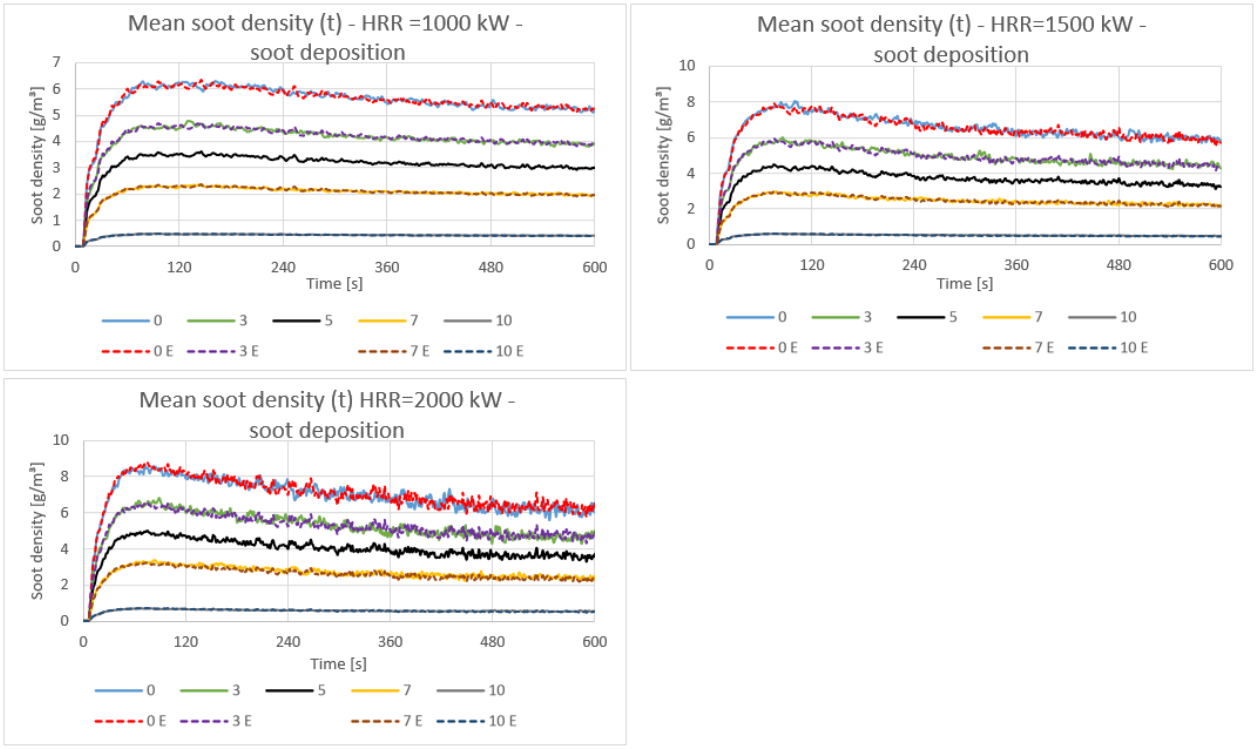

Figure B.34 Time histories of estimated and simulated values of statistical mean soot density. Series applied from upper left: 10, 11, 12

The time history plots in Figure B.35 show results from simulation series 13, 14, 15. The former and the two latter using medium and fast HRR-growths respectively, and Model A. In these series, the surrogate-fuel method is not applied. Series 13 and 14 use fuel alterations only for soot yield. Series 15 applies the GM-series. Series 13 uses simulation A.M.5.L as base. Series 14 and 15 uses simulation A.F.5.L as base. Ratios of time averaged estimations to simulations plotted against correlation factor-values are provided in Figure 4.12 and Figure 4.13. The ratios are time averaged from t=120 s to 200 s for medium HRR-growth and from t=90 s to 200 s for fast HRR-growth.

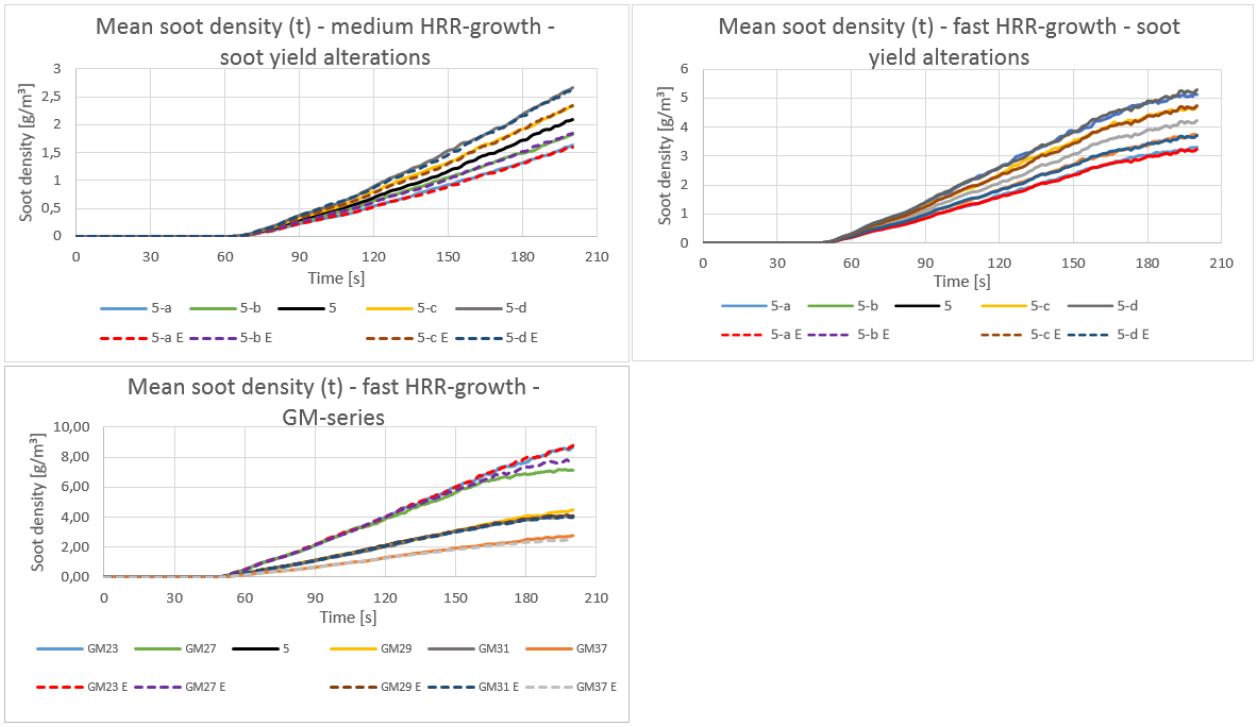

Figure B.35 Time histories of estimated and simulated values of statistical mean soot density. Series applied from upper left: 13, 14, 15.

The time history plots in Figure B.36 show results from simulation series 16, 17, 18 and 19 using HRRs of 3000, 5000, 7000 and 5000 kW respectevely, and Model B. Series 16 through 18 applies no deposition, while deposition mechanisms are active in series 19. Recorded values are made from measurement position I. Ratios of time averaged estimations to simulations plotted against correlation factor-values are provided in Figure 4.10. The ratios are time averaged from t=400 s to 600 s.

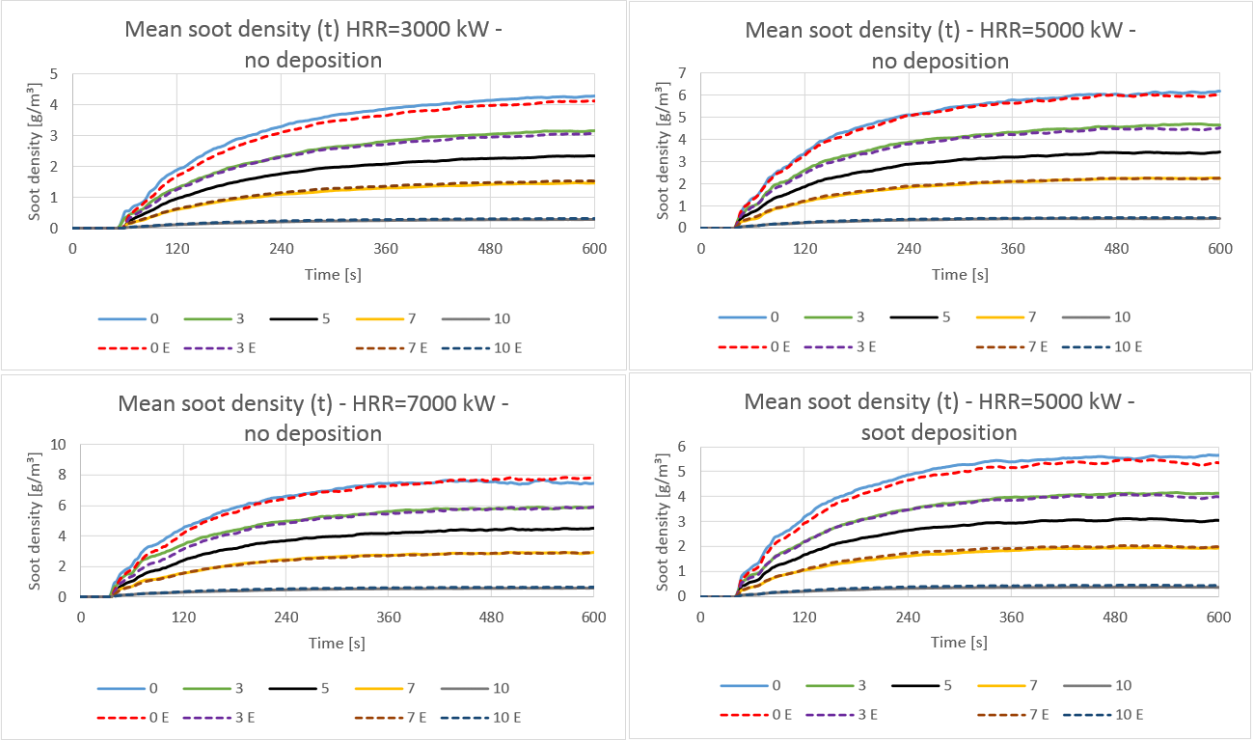

Figure B.36 Time histories of estimated and simulated values of statistical mean soot density. Recorded values are from Model B, measurement I. Series applied from upper left: 16, 17, 18, 19.

C FDS input

Representations of the FDS input files applied in the study is presented in this Appendix. The input file representing Model A is the simulation indexed A.C1,5.5.S.Y. The file representing Model B is the simulation indexed B.C3.5.L. Both are base simulations, indicated by the fuel parameter index 5. The former employs active soot deposition mechanisms. The latter uses the simple transport method, default in FDS. As such, both methods of soot transport are represented. By combining these input files with the information presented in the methods chapter, reproduction of all simulations is possible.

C.1 Model A

A_C1-5_5_S_Y.fds

Generated by PyroSim - Version 2018.2.0730

19.jan.2019 14:03:14

```
&HEAD CHID='A_C1-5_5_S_Y'/
&TIME T_END=600.0/
&DUMP RENDER_FILE='A_C1-5_5_S_Y.ge1', DT_RESTART=50.0, DT_SL3D=0.25/
&MISC VISIBILITY_FACTOR=8.0,
SUPPRESSION=.FALSE.
      GRAVITATIONAL_DEPOSITION  = .TRUE.
      THERMOPHORETIC_DEPOSITION = .TRUE.
      TURBULENT_DEPOSITION      = .TRUE./

&MESH ID='Room-corridor-a', IJK=52,76,52, XB=0.0,2.6,0.0,3.8,0.0,2.6/
&MESH ID='Room-corridor-b', IJK=26,26,26, XB=0.0,2.6,3.8,6.4,0.0,2.6/
&MESH ID='Corridor-outside', IJK=100,28,26, XB=2.6,12.6,3.6,6.4,0.0,2.6/

&SPEC ID='MY FUEL', FORMULA = 'C1H1.7O0.52N0.04' /
&SPEC ID='NITROGEN',                LUMPED_COMPONENT_ONLY=.TRUE./
&SPEC ID='OXYGEN',                  LUMPED_COMPONENT_ONLY=.TRUE./
```

```
&SPEC ID='WATER VAPOR',           LUMPED_COMPONENT_ONLY=.TRUE./
&SPEC ID='CARBON DIOXIDE',        LUMPED_COMPONENT_ONLY=.TRUE./
&SPEC ID='CARBON MONOXIDE',   LUMPED_COMPONENT_ONLY=.TRUE./
&SPEC ID='SOOT',                  AEROSOL=.TRUE./


&SPEC ID='AIR', BACKGROUND =.TRUE.,
      SPEC_ID(1)='OXYGEN',                VOLUME_FRACTION(1)=0.208057,
      SPEC_ID(2)='NITROGEN',              VOLUME_FRACTION(2)=0.783214,
      SPEC_ID(3)='WATER VAPOR',           VOLUME_FRACTION(3)=0.008342,
      SPEC_ID(4)='CARBON DIOXIDE',        VOLUME_FRACTION(4)=0.000387 /

&SPEC ID='PRODUCTS'
      SPEC_ID(1)='CARBON DIOXIDE',        VOLUME_FRACTION(1)=0.143550,
      SPEC_ID(2)='WATER VAPOR',           VOLUME_FRACTION(2)=0.158831,
      SPEC_ID(3)='NITROGEN',              VOLUME_FRACTION(3)=0.655908,
      SPEC_ID(4)='CARBON MONOXIDE', VOLUME_FRACTION(4)=0.002337 /

&REAC FUEL='MY FUEL', SPEC_ID_NU='MY FUEL', 'AIR', 'PRODUCTS','SOOT',
      NU=-1,-4.601248,5.524804,0.2175391575, HEAT_OF_COMBUSTION=17075.15 /



&MATL ID='GYPSUM',
   SPECIFIC_HEAT=1.09,
   CONDUCTIVITY=0.17,
   DENSITY=930.0/
&MATL ID='MINERAL_WOOL',
   SPECIFIC_HEAT=0.8,
   CONDUCTIVITY=0.041,
```

```
    DENSITY=100.0/
&MATL ID='CONCRETE',
    SPECIFIC_HEAT=1.04,
    CONDUCTIVITY=1.8,
    DENSITY=2280.0/

&SURF ID='EI 60wall',
    RGB=190,220,220,
    BACKING='VOID',
    MATL_ID(1,1)='GYPSUM',
    MATL_ID(2,1)='GYPSUM',
    MATL_ID(3,1)='MINERAL_WOOL',
    MATL_ID(4,1)='GYPSUM',
    MATL_ID(5,1)='GYPSUM',
    MATL_MASS_FRACTION(1,1)=1.0,
    MATL_MASS_FRACTION(2,1)=1.0,
    MATL_MASS_FRACTION(3,1)=1.0,
    MATL_MASS_FRACTION(4,1)=1.0,
    MATL_MASS_FRACTION(5,1)=1.0,
    THICKNESS(1:5)=0.0125,0.0125,0.12,0.0125,0.0125/
&SURF ID='EI 60, roof',
    RGB=255,0,3,
    BACKING='VOID',
    MATL_ID(1,1)='GYPSUM',
    MATL_ID(2,1)='GYPSUM',
    MATL_ID(3,1)='MINERAL_WOOL',
    MATL_ID(4,1)='GYPSUM',
    MATL_MASS_FRACTION(1,1)=1.0,
    MATL_MASS_FRACTION(2,1)=1.0,
    MATL_MASS_FRACTION(3,1)=1.0,
```

MATL_MASS_FRACTION(4,1)=1.0,

THICKNESS(1:4)=0.0125,0.0125,0.17,0.0125/

&SURF ID='Concrete floor',

RGB=225,245,253,

BACKING='VOID',

MATL_ID(1,1)='CONCRETE',

MATL_MASS_FRACTION(1,1)=1.0,

THICKNESS(1)=0.2/

&SURF ID='Flame',

COLOR='RED',

HRRPUA=1041.7/

&OBST ID='Obstruction', XB=10.1,10.2,3.8,4.4,0.0,2.4, SURF_ID='EI 60wall'/

&OBST ID='Obstruction', XB=1.9,12.6,3.7,3.8,0.0,2.4, SURF_ID='EI 60wall'/

&OBST ID='Obstruction', XB=0.0,12.6,6.2,6.3,0.0,2.4, SURF_ID='EI 60wall'/

&OBST ID='Obstruction', XB=0.7,1.9,3.7,3.8,2.0,2.4, SURF_ID='EI 60wall'/

&OBST ID='Obstruction', XB=0.0,0.1,3.8,6.3,0.0,2.4, SURF_ID='EI 60wall'/

&OBST ID='Obstruction', XB=10.1,10.2,5.6,6.2,0.0,2.4, SURF_ID='EI 60wall'/

&OBST ID='Obstruction', XB=-6.344132E-17,0.7,3.7,3.8,0.0,2.4, SURF_ID='EI 60wall'/

&OBST ID='Obstruction', XB=10.1,10.2,4.4,5.6,2.0,2.4, SURF_ID='EI 60wall'/

&OBST ID='Obstruction', XB=0.7,1.9,1.3,2.5,0.0,0.5, SURF_ID='INERT'/

&OBST ID='Obstruction', XB=0.0,0.1,0.1,3.8,0.0,2.4, SURF_ID='EI 60wall'/

&OBST ID='Obstruction', XB=0.0,2.6,0.0,0.1,0.0,2.4, SURF_ID='EI 60wall'/

&OBST ID='Obstruction', XB=2.5,2.6,0.1,3.8,0.0,2.4, SURF_ID='EI 60wall'/

&OBST ID='Obstruction, roof', XB=0.0,12.6,3.7,6.3,2.4,2.5, COLOR='INVISIBLE', SURF_ID='EI 60, roof'/

&OBST ID='Obstruction, roof', XB=0.0,2.6,0.0,3.7,2.4,2.5, COLOR='INVISIBLE', SURF_ID='EI 60, roof'/

&OBST ID='Obstruction, concrete floor', XB=0.0,2.6,0.0,3.7,-0.1,-8.326673E-17, SURF_ID='Concrete floor'/

&OBST ID='Obstruction, CONCRETE floor', XB=0.0,12.6,3.7,6.3,-0.1,-8.326673E-17,
SURF_ID='Concrete floor'/

&VENT ID='Firevent', SURF_ID='Flame', XB=0.7,1.9,1.3,2.5,0.5,0.5/

&VENT ID='Vent02', SURF_ID='OPEN', XB=12.6,12.6,3.7,6.3,0.0,2.4/

&DEVC ID='[Species: CARBON MONOXIDE] Mass Fraction_MEAN', QUANTITY='MASS
FRACTION', SPEC_ID='CARBON MONOXIDE', STATISTICS='MEAN', XB=7.5,10.1,3.8,6.2,1.5,2.4/

&DEVC ID='[Species: CARBON MONOXIDE] Mass Fraction_MAX', QUANTITY='MASS
FRACTION', SPEC_ID='CARBON MONOXIDE', STATISTICS='MAX', XB=7.5,10.1,3.8,6.2,1.5,2.4/

&DEVC ID='INV [Species: SOOT] Density_MEAN', QUANTITY='DENSITY', SPEC_ID='SOOT',
STATISTICS='MEAN', XB=7.5,10.1,3.8,6.1,1.5,2.4/

&DEVC ID='INV [Species: SOOT] Density_MIN', QUANTITY='DENSITY', SPEC_ID='SOOT',
STATISTICS='MIN', XB=7.5,10.1,3.8,6.1,1.5,2.4/

&DEVC ID='INV [Species: SOOT] Density_MAX', QUANTITY='DENSITY', SPEC_ID='SOOT',
STATISTICS='MAX', XB=7.5,10.1,3.8,6.1,1.5,2.4/

&DEVC ID='[Species: SOOT] Density_MEAN', QUANTITY='DENSITY', SPEC_ID='SOOT',
STATISTICS='MEAN', XB=7.5,10.1,3.8,6.2,1.5,2.4/

&DEVC ID='[Species: SOOT] Density_MIN', QUANTITY='DENSITY', SPEC_ID='SOOT',
STATISTICS='MIN', XB=7.5,10.1,3.8,6.2,1.5,2.4/

&DEVC ID='[Species: SOOT] Density_MAX', QUANTITY='DENSITY', SPEC_ID='SOOT',
STATISTICS='MAX', XB=7.5,10.1,3.8,6.2,1.5,2.4/

&DEVC ID='[Species: CARBON MONOXIDE] Density_MEAN', QUANTITY='DENSITY',
SPEC_ID='CARBON MONOXIDE', STATISTICS='MEAN', XB=7.5,10.1,3.8,6.1,1.5,2.4/

&DEVC ID='[Species: CARBON MONOXIDE] Density_MIN', QUANTITY='DENSITY',
SPEC_ID='CARBON MONOXIDE', STATISTICS='MIN', XB=7.5,10.1,3.8,6.1,1.5,2.4/

&DEVC ID='[Species: CARBON MONOXIDE] Density_MAX', QUANTITY='DENSITY',
SPEC_ID='CARBON MONOXIDE', STATISTICS='MAX', XB=7.5,10.1,3.8,6.1,1.5,2.4/

&TAIL /

C.2 Model B

B_C3_5_L.fds

Generated by PyroSim - Version 2018.2.0730

05.feb.2019 13:35:21

```
&HEAD CHID='B_C3_5_S'/
&TIME T_END=600.0/
&DUMP RENDER_FILE='B_C3_5_S.ge1', DT_RESTART=50.0, DT_SL3D=0.25/
&MISC VISIBILITY_FACTOR=8.0/

&MESH ID='Room-corridor-a', IJK=66,78,50, XB=0.0,6.6,-2.0,5.8,0.0,5.0/
&MESH ID='Room-corridor-b', IJK=66,75,26, XB=0.0,6.6,5.8,13.3,0.0,2.6/
&MESH ID='Corridor-outside-a', IJK=80,78,26, XB=6.6,14.6,5.6,13.4,0.0,2.6/
&MESH ID='Corridor-outside-b', IJK=125,28,26, XB=14.6,27.1,10.6,13.4,0.0,2.6/



&REAC ID='Reaction1',
     FYI='SFPE, Red pine & GM25, 50/50%',
     FUEL='REAC_FUEL',
     C=1.0,
     H=1.7,
     O=0.52,
     N=0.04,
     AUTO_IGNITION_TEMPERATURE=0.0,
     CO_YIELD=0.016,
     SOOT_YIELD=0.105,
     EPUMO2=1.26E4/



&MATL ID='GYPSUM',
```

```
    SPECIFIC_HEAT=1.09,
    CONDUCTIVITY=0.17,
    DENSITY=930.0/
&MATL ID='MINERAL_WOOL',
    SPECIFIC_HEAT=0.8,
    CONDUCTIVITY=0.041,
    DENSITY=100.0/
&MATL ID='CONCRETE',
    SPECIFIC_HEAT=1.04,
    CONDUCTIVITY=1.8,
    DENSITY=2280.0/

&SURF ID='EI 60wall',
    RGB=190,220,220,
    BACKING='VOID',
    MATL_ID(1,1)='GYPSUM',
    MATL_ID(2,1)='GYPSUM',
    MATL_ID(3,1)='MINERAL_WOOL',
    MATL_ID(4,1)='GYPSUM',
    MATL_ID(5,1)='GYPSUM',
    MATL_MASS_FRACTION(1,1)=1.0,
    MATL_MASS_FRACTION(2,1)=1.0,
    MATL_MASS_FRACTION(3,1)=1.0,
    MATL_MASS_FRACTION(4,1)=1.0,
    MATL_MASS_FRACTION(5,1)=1.0,
    THICKNESS(1:5)=0.0125,0.0125,0.12,0.0125,0.0125/
&SURF ID='EI 60, roof',
    RGB=255,0,3,
    BACKING='VOID',
    MATL_ID(1,1)='GYPSUM',
```

```
    MATL_ID(2,1)='GYPSUM',
    MATL_ID(3,1)='MINERAL_WOOL',
    MATL_ID(4,1)='GYPSUM',
    MATL_MASS_FRACTION(1,1)=1.0,
    MATL_MASS_FRACTION(2,1)=1.0,
    MATL_MASS_FRACTION(3,1)=1.0,
    MATL_MASS_FRACTION(4,1)=1.0,
    THICKNESS(1:4)=0.0125,0.0125,0.17,0.0125/
&SURF ID='Concrete floor',
    RGB=225,245,253,
    BACKING='VOID',
    MATL_ID(1,1)='CONCRETE',
    MATL_MASS_FRACTION(1,1)=1.0,
    THICKNESS(1)=0.2/
&SURF ID='Flame',
    COLOR='RED',
    HRRPUA=1038.0/

&OBST ID='Obstruction', XB=14.5,14.6,5.7,11.4,0.0,2.4, SURF_ID='EI 60wall'/
&OBST ID='Obstruction', XB=3.9,6.5,5.7,5.8,0.0,5.0, SURF_ID='EI 60wall'/
&OBST ID='Obstruction', XB=0.0,14.6,13.2,13.3,0.0,2.4, COLOR='INVISIBLE', SURF_ID='EI 60wall'/
&OBST ID='Obstruction', XB=2.7,3.9,5.7,5.8,2.0,5.0, SURF_ID='EI 60wall'/
&OBST ID='Obstruction', XB=0.0,0.1,5.8,13.3,0.0,2.4, SURF_ID='EI 60wall'/
&OBST ID='Obstruction', XB=14.5,14.6,12.6,13.2,0.0,2.4, SURF_ID='EI 60wall'/
&OBST ID='Obstruction', XB=0.0,2.7,5.7,5.8,0.0,5.0, SURF_ID='EI 60wall'/
&OBST ID='Obstruction', XB=14.5,14.6,11.4,12.6,2.0,2.4, SURF_ID='EI 60wall'/
&OBST ID='Obstruction', XB=2.5,4.2,1.9,3.6,0.0,0.5, SURF_ID='INERT'/
&OBST ID='Obstruction', XB=0.0,0.1,0.1,5.8,0.0,5.0, SURF_ID='EI 60wall'/
&OBST ID='Obstruction', XB=6.5,6.6,0.1,5.8,0.0,5.0, COLOR='INVISIBLE', SURF_ID='EI 60wall'/
&OBST ID='Obstruction', XB=0.0,2.1,0.0,0.1,0.0,5.0, SURF_ID='EI 60wall'/
```

&OBST ID='Obstruction', XB=2.1,4.5,0.0,0.1,3.0,5.0, SURF_ID='EI 60wall'/

&OBST ID='Obstruction', XB=14.6,27.1,10.7,10.8,0.0,2.4, SURF_ID='EI 60wall'/

&OBST ID='Obstruction', XB=4.5,6.6,0.0,0.1,0.0,5.0, SURF_ID='EI 60wall'/

&OBST ID='Obstruction', XB=24.6,24.7,10.8,11.4,0.0,2.4, SURF_ID='EI 60wall'/

&OBST ID='Obstruction', XB=24.6,24.7,11.4,12.6,2.0,2.4, SURF_ID='EI 60wall'/

&OBST ID='Obstruction', XB=24.6,24.7,12.6,13.2,0.0,2.4, SURF_ID='EI 60wall'/

&OBST ID='Obstruction', XB=6.5,14.6,5.7,5.8,0.0,2.4, SURF_ID='EI 60wall'/

&OBST ID='Obstruction', XB=14.6,27.1,13.2,13.3,0.0,2.4, COLOR='INVISIBLE', SURF_ID='EI 60wall'/

&OBST ID='Obstruction, roof', XB=0.0,14.6,5.7,13.4,2.4,2.5, COLOR='INVISIBLE', SURF_ID='EI 60, roof'/

&OBST ID='Obstruction, roof', XB=0.0,6.6,0.1,5.7,5.0,5.1, COLOR='INVISIBLE', SURF_ID='EI 60, roof'/

&OBST ID='Obstruction, roof', XB=14.6,27.1,10.8,13.4,2.4,2.5, COLOR='INVISIBLE', SURF_ID='EI 60, roof'/

&OBST ID='Obstruction, concrete floor', XB=0.0,6.6,-1.0,5.7,-0.1,0.0, SURF_ID='Concrete floor'/

&OBST ID='Obstruction, CONCRETE floor', XB=0.0,14.6,5.7,13.3,-0.1,0.0, SURF_ID='Concrete floor'/

&OBST ID='Obstruction, CONCRETE floor', XB=14.6,27.1,10.7,13.3,-0.1,0.0, SURF_ID='Concrete floor'/

&VENT ID='Vent05', SURF_ID='OPEN', XB=0.0,6.6,-2.0,0.0,5.0,5.0/

&VENT ID='Firevent', SURF_ID='Flame', XB=2.5,4.2,1.9,3.6,0.5,0.5/

&VENT ID='Vent02', SURF_ID='OPEN', XB=27.1,27.1,10.7,13.3,0.0,2.4/

&VENT ID='Vent01', SURF_ID='OPEN', XB=0.0,6.6,-2.0,-2.0,0.0,5.0/

&VENT ID='Vent03', SURF_ID='OPEN', XB=0.0,0.0,-2.0,0.0,0.0,5.0/

&VENT ID='Vent04', SURF_ID='OPEN', XB=6.6,6.6,-2.0,0.0,0.0,5.0/

&DEVC ID='[Species: SOOT] Density01_MEAN', QUANTITY='DENSITY', SPEC_ID='SOOT', STATISTICS='MEAN', XB=22.0,24.6,10.8,13.2,1.5,2.4/

&DEVC ID='[Species: SOOT] Density01_MIN', QUANTITY='DENSITY', SPEC_ID='SOOT', STATISTICS='MIN', XB=22.0,24.6,10.8,13.2,1.5,2.4/

&DEVC ID='[Species: SOOT] Density01_MAX', QUANTITY='DENSITY', SPEC_ID='SOOT', STATISTICS='MAX', XB=22.0,24.6,10.8,13.2,1.5,2.4/

&DEVC ID='[Species: CARBON MONOXIDE] Mass Fraction01_MEAN', QUANTITY='MASS FRACTION', SPEC_ID='CARBON MONOXIDE', STATISTICS='MEAN', XB=22.0,24.6,10.8,13.2,1.5,2.4/

&DEVC ID='[Species: CARBON MONOXIDE] Mass Fraction01_MAX', QUANTITY='MASS FRACTION', SPEC_ID='CARBON MONOXIDE', STATISTICS='MAX', XB=22.0,24.6,10.8,13.2,1.5,2.4/

&DEVC ID='[Species: SOOT] Density02_MEAN', QUANTITY='DENSITY', SPEC_ID='SOOT', STATISTICS='MEAN', XB=0.1,2.7,10.8,13.2,1.5,2.4/

&DEVC ID='[Species: SOOT] Density02_MIN', QUANTITY='DENSITY', SPEC_ID='SOOT', STATISTICS='MIN', XB=0.1,2.7,10.8,13.2,1.5,2.4/

&DEVC ID='[Species: SOOT] Density02_MAX', QUANTITY='DENSITY', SPEC_ID='SOOT', STATISTICS='MAX', XB=0.1,2.7,10.8,13.2,1.5,2.4/

&DEVC ID='[Species: CARBON MONOXIDE] Mass Fraction02_MEAN', QUANTITY='MASS FRACTION', SPEC_ID='CARBON MONOXIDE', STATISTICS='MEAN', XB=0.1,2.7,10.8,13.2,1.5,2.4/

&DEVC ID='[Species: CARBON MONOXIDE] Mass Fraction02_MAX', QUANTITY='MASS FRACTION', SPEC_ID='CARBON MONOXIDE', STATISTICS='MAX', XB=0.1,2.7,10.8,13.2,1.5,2.4/

&TAIL /

Bibliography

[1] BBC, "BBC News," 18 June 2018. [Online]. Available: https://www.bbc.com/news/uk-40301289. [Accessed 23 May 2019].

[2] BBC, "BBC News," 16 April 2019. [Online]. Available: https://www.bbc.com/news/world-europe-47941794. [Accessed 23 May 2019].

[3] USA TODAY, "USA TODAY," 20 04 2019. [Online]. Available: https://eu.usatoday.com/story/news/world/2019/04/20/notre-dame-cathedral-fire-1-billion-rebuild-paris-france-church/3528844002/. [Accessed 23 05 2019].

[4] NIST, "FDS-SMV, Fire Dynamics Simulator (FDS) and Smokeview (SMV)," 20 03 2016. [Online]. Available: https://pages.nist.gov/fds-smv/. [Accessed 27 05 2019].

[5] D. A. Purser, "Combustion Toxicity," in *SFPE Handbook of Fire Protection, Fifth edition*, New York, Springer, 2016, pp. 2207-2307.

[6] D. Drysdale, "Thermochemistry," in *SFPE Handbook of Fire Protection Engineering, Fifth Edition*, New York, Springer, 2016, pp. 138-150.

[7] D. Drysdale, An Introduction to Fire Dynamics, Chichester: John Wiley & Sons, Ltd, 2011.

[8] e. a. M.M. Khan, "Combustion Characteristics of Materials and Generation of Fire Products," in *SFPE Handbook of Fire Protection Engineering, Fifth Edition*, New York, Springer, 2016, pp. 1143-1232.

[9] J. G. Q. Björn Karlsson, Enclosure Fire Dynamics, CRC Press, 2000.

[10] NFPA, *NFPA 204, Standard for Smoke and Heat Venting*, NFPA, 2018.

[11] Standard Norge, *SN-INSTA/TS 950:2014, Fire Safety Engineering - Comparative method to verify fire safety design in buildings*, Standard Norge, 2014.

[12] V. Babrauskas, "Heat Release Rates," in *SFPE Handbook of Fire Protection Engineering, Fifth Edition*, New York, Springer, 2016, pp. 799-904.

[13] Fluid Mechanics (Fith Edition), "ScienceDirect," ScienceDirect, 2012. [Online]. Available: https://www.sciencedirect.com/topics/materials-science/computational-fluid-dynamics. [Accessed 20 01 2019].

[14] S. M. Kevin McGrattan, "Modelling Fires Using Computational Fluid Dynamics (CFD)," in *SFPE Handbook of Fire Protection Engineering*, New York, Springer, 2016, pp. 1034-1065.

[15] B. Merci, "Introduction to Fluid Mechanics," in *SFPE Handbook of Fire Protection Engineering, Fifth Edition*, New York, Springer, 2016, pp. 1-24.

[16] NIST, *NIST Special Publication 1018-1 Sixth Edition, Fire Dynamics Simulator Technical Reference Guide, Volume 1: Mathematical model,* NIST, 2018.

[17] NIST, *NIST Special Publication 1019, Sixth Edition, Fire Dynamics Simulator User's Guide,* NIST, 2018.

[18] UT Fire Research Group, "FDS Mesh Size Calculator," 2017. [Online]. Available: https://www.utfireresearch.com/fds-mesh. [Accessed 03 01 2019].

[19] NIST, *NIST Special Publication 1018-3 Sixth Edition, Fire Dynamics Simulator Technical Reference Guide, Volume 3: Validation,* NIST, 2018.

[20] Best Practice gruppen, *CFD Best Practice,* 2009.

[21] United States Nuclear Regulatoru Commission, NUREG, *Verification and Validation of Selected Fire Models for Nuclear Power Plant Applications,* NUREG, EPRI, 2016.

[22] R. McDermott, "GitHub," 05 02 2019. [Online]. Available: https://github.com/firemodels/fds/wiki/FDS-Road-Map. [Accessed 02 03 2019].

[23] Thunderhead Engineering, "PyroSim, Fire Dynamics and Smoke Control," Thunderhead Engineering, [Online]. Available: https://www.thunderheadeng.com/pyrosim/. [Accessed 02 03 2019].

[24] Boverkets författningssamling, *Boverkets ändring av verkets allmänna råd (2011:27) om analytisk dimensionering av byggnaders brandskydd; BFS 2013:12 BBRAD 3,* Boverkets författningssamling, 2013.

[25] Föreningen för brandteknisk ingenjörsvetenskap, BIV Officiell svensk avdelning i Society of Fire Protection Engineers , *BIV:s tillämpningsdokument 2/2013 – Utgåva 1 - CFD-beräkningar med FDS,* Malmö: Föreningen för brandteknisk ingenjörsvetenskap, BIV , 2013.

[26] RISE, "Information about Room Corner Test," RISE, [Online]. Available: https://www.sp.se/en/index/services/firetest_building/firetest_bu%C3%ADlding/iso_9705_room_corner_test/Sidor/default.aspx. [Accessed 02 03 2019].

[27] NIST, *NIST Special Publication 1018-2 Sixth Edition, Fire Dynamics Simulator Technical Reference Guide, Volume 2: Verification,* NIST, 2018.

[28] SINTEF Byggforsk, *520.322 Brannmotstand for vegger,* SINTEF, 2008.

[29] NORGIPS, "Etasjeskiller, Brannegenskaper," [Online]. Available: https://norgips.no/prosjektering/himlinger-og-etasjeskiller/brannklassifisering. [Accessed 13 02 2019].

[30] SFPE, "Appendix 3, Fuel Properties and Combustion Data," in *SFPE Handbook of Fire Protection Engineering, Fifth Edition*, New York, Springer, 2016, pp. 3437-3475.

[31] United States Department of Agriculture, Natural Resources Conservation Service, "USDA," 29 05 2003. [Online]. Available: https://plants.usda.gov/plantguide/pdf/cs_quru.pdf. [Accessed 28 02 2019].

[32] ExcelFunctions.net, "ExcelFunctions.net," 2019. [Online]. Available: https://www.excelfunctions.net/excel-intercept-function.html. [Accessed 06 04 2019].

[33] The Engineering Toolbox, "Air - Density, Specific Weight and Thermal Expansion Coefficient at Varying Temperature and Constant Pressures," 2003. [Online]. Available: https://www.engineeringtoolbox.com/air-density-specific-weight-d_600.html. [Accessed 25 05 2019].

[34] The Engineering Toolbox, "Air - Specific Heat at Constant Temperature and Varying Pressure," 2009. [Online]. Available: https://www.engineeringtoolbox.com/air-specific-heat-various-pressures-d_1535.html. [Accessed 25 05 2019].